

A Thesis Submitted for the Degree of PhD at the University of Warwick

Permanent WRAP URL:

<http://wrap.warwick.ac.uk/164145>

Copyright and reuse:

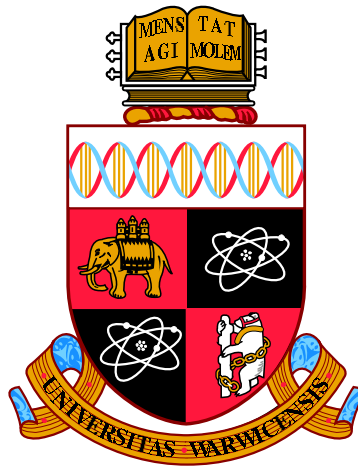
This thesis is made available online and is protected by original copyright.

Please scroll down to view the document itself.

Please refer to the repository record for this item for information to help you to cite it.

Our policy information is available from the repository home page.

For more information, please contact the WRAP Team at: wrap@warwick.ac.uk



**Turbulent Cascades and Condensation in Nonlinear
Wave Systems**

by

Jonathan Matthew Skipp

Thesis

Submitted to the University of Warwick

for the degree of

Doctor of Philosophy

Centre for Complexity Science

September 2021

THE UNIVERSITY OF
WARWICK

Contents

List of Tables	vi
List of Figures	vii
Acknowledgments	xi
Declarations	xiii
Abstract	xiv
Abbreviations	xv
Chapter 1 Introduction	1
1.1 Wave turbulence vs. hydrodynamic turbulence	1
1.2 Large-scale coherent structures in wave turbulence	3
1.3 Outline of this thesis	4
Chapter 2 Theoretical Background	6
2.1 Equations studied in this thesis	6
2.2 Invariants of the GPE, SHE, and CHM	7
2.2.1 Conserved quantities of Schrödinger-type equations	7
2.2.2 Conserved quantities in the CHM equation	9
2.3 Derivation of the (four-wave) kinetic equation	10
2.3.1 Fourier space representation	11
2.3.2 Waveaction variable and the Hamiltonian formulation	12
2.3.3 Interaction variable and asymptotic expansion	14
2.3.4 Statistical closure	16
2.3.5 Large box and weak nonlinearity limit	18
2.3.6 Three-wave kinetic equation	20
2.4 Invariants of the kinetic equation	20
2.4.1 Invariants of the Schrödinger-type equations	21
2.4.2 Invariants of the CHM equations	22

2.4.2.1	Zonostrophy: the third invariant of the CHM kinetic equation	22
2.5	Stationary solutions of the kinetic equation	23
2.5.1	The Rayleigh-Jeans equilibrium spectrum	23
2.5.2	Kolmogorov-Zakharov flux spectra	23
2.5.2.1	KZ spectra for isotropic systems	24
2.5.2.2	Anisotropic systems, and lack of KZ spectra in the CHM equation	24
2.6	The dual cascade in the GPE: the Fjørtoft argument	25
Chapter 3 Equilibria and condensates in Rossby and drift wave turbulence		28
3.1	Chapter summary	28
3.2	Introduction	28
3.2.1	Condensation outside and within the equilibrium spectrum	31
3.2.2	Organisation of this chapter	32
3.3	Charney-Hasegawa-Mima equation	32
3.3.1	Wave turbulence and the CHM kinetic equation	33
3.3.2	Invariants of the kinetic equation, and the Rayleigh-Jeans spectrum	34
3.3.2.1	Invariants of the kinetic equation	34
3.3.2.2	Rayleigh-Jeans equilibrium spectrum	35
3.4	Regularity and divergence of the RJ spectrum	37
3.4.1	The λ — μ plane; $\mu_{\pm}^+(\lambda)$ are the boundaries of the RJ-accessible region	38
3.4.2	The k_x — k_y plane: \mathbf{k}_{\pm}^+ are the modes at which $n_{\mathbf{k}}^{\text{RJ}}$ becomes singular	39
3.4.2.1	Bottom row of figure 3.3.	39
3.4.2.2	Top row of figure 3.3.	41
3.4.3	Regularity of the RJ spectrum, negative thermodynamic potentials	41
3.5	Condensation in the RJ spectrum	42
3.5.1	Finite-size condensation at the edge of the RJ region	45
3.5.2	Lack of condensation in the infinite box limit	46
3.6	CHM phase diagram	47
3.6.1	Interior of the RJ sail	48
3.6.2	Boundary of the RJ sail	49
3.6.3	Outside the RJ sail	50
3.7	Discussion and conclusion	52
3.A	Appendix: Application to the Gross-Pitaevskii equation	55

3.A.1	Review of the GPE in an infinite-sized domain	55
3.A.2	RJ spectra and Bose-Einstein condensation in 3D.	56
3.A.3	RJ spectra in 2D with no true Bose-Einstein condensation . .	58
3.A.4	The 2D GPE in a finite domain	58
Chapter 4	Wave turbulence in self-gravitating Bose gases and non-	
	local nonlinear optics	61
4.1	Chapter summary	61
4.2	Introduction	62
4.2.1	Wave turbulence cascades	62
4.2.2	Schrödinger-Helmholtz equations	62
4.2.2.1	Large-scale limit: The nonlinear Schrödinger equation	63
4.2.2.2	Small-scale limit: The Schrödinger-Newton equations	64
4.2.2.3	Physical applications of the Schrödinger-Helmholtz equations	66
4.2.3	Turbulence in the nonlinear Schrödinger and Schrödinger-Newton equations	67
4.2.4	Organisation of this chapter	69
4.3	Building blocks of Schrödinger-Helmholtz wave turbulence	69
4.3.1	Hamiltonian formulation of the Schrödinger-Helmholtz equa- tions	69
4.3.2	Kinetic equation and conserved quantities	71
4.3.3	Fjørtoft argument for two conserved invariants	73
4.3.4	Kolmogorov-Zakharov flux spectra as formal solutions of the kinetic equation	74
4.3.5	Equilibrium spectra	75
4.3.6	Directions of the energy and particle fluxes and realisability of the scale-invariant spectra	75
4.3.7	Differential approximation model for wave turbulence	77
4.3.8	Fluxes in the differential approximation	79
4.4	Turbulent spectra in the Schrödinger-Helmholtz model	80
4.4.1	Reconciling with the Fjørtoft argument	80
4.4.2	Spectra in the 3D Schrödinger-Newton model	80
4.4.2.1	Warm inverse particle cascade in the 3D Schrödinger- Newton model	81
4.4.2.2	Warm direct energy cascade in the 3D Schrödinger- Newton model	83
4.4.2.3	Warm dual cascade in the 3D Schrödinger-Newton model	83
4.4.3	Spectra in the 2D Schrödinger-Newton model	84

4.4.3.1	Log-corrected inverse particle cascade in the 2D Schrödinger-Newton model	84
4.4.3.2	Warm direct energy cascade in the 2D Schrödinger-Newton model	85
4.4.4	Spectra in the 2D nonlinear Schrödinger model	85
4.4.4.1	Warm inverse particle cascade in the 2D nonlinear Schrödinger model	86
4.4.4.2	Log-corrected direct energy cascade in the 2D nonlinear Schrödinger model	86
4.4.5	Crossover from warm to Kolmogorov-Zakharov cascade in the 3D Schrödinger-Helmholtz model	87
4.5	Conclusion and outlook	88
4.5.1	Summary and discussion of results	88
4.5.2	Outlook for wave turbulence in Schrödinger-Helmholtz systems	91
4.A	Appendix: Relation between the cosmological constant and the Jeans swindle	93
4.B	Appendix: Wave turbulence in inhomogeneous systems	93
4.B.1	Incoherent modulational instability	96
4.B.2	Kinetic regime	97
4.B.2.1	Kinetic regime in the local limit	98
4.B.2.2	Kinetic regime in the nonlocal limit	98
4.C	Appendix: Bimodal cascade spectra in the differential approximation model	99

Chapter 5 The Schrödinger-Helmholtz equation in 2D: direct numerical simulations 102

5.1	Chapter summary and organisation	102
5.2	Numerical methods	102
5.2.1	Pseudospectral methods for nonlinear partial differential equations	103
5.2.1.1	Nonlinear term and de-aliasing	104
5.2.2	Forcing and dissipation	105
5.2.3	Time-stepping	106
5.3	Results on the freely-evolving and forced-dissipated 2D SHE	106
5.3.1	Benchmarking: conservation of energy and waveaction	107
5.3.2	Evolution of a freely-evolving simulation	108
5.3.3	Forced-dissipated simulation: structure formation via the inverse cascade	110
5.4	Discussion and future direction of research	113
5.4.1	Discussion of numerical results	113

5.4.2 Future directions 115

List of Tables

3.1	Equivalence between equilibrium spectra and invariants of the CHM equation, GPE, and 2D Euler equation.	36
-----	---	----

List of Figures

2.1	Schematic sketch of (a) 4-wave interactions of the $2 \leftrightarrow 2$ type, and (b) 3-wave interactions of $2 \leftrightarrow 1$ type.	11
3.1	Waves, zonal flows, and vortices in quasi-2D flows with a β effect. (a) Geophysical case: observations of the atmosphere of Jupiter (b) Plasma case: simulation of a tokamak plasma.	30
3.2	The λ - μ plane, with regions where the RJ spectrum is accessible (white) separated from the RJ-forbidden (grey) region by the RJ boundary comprised of the coloured curves $\mu^+(\lambda)$ and $\mu_-(\lambda)$. (a) Accurate plot of λ - μ plane with $\epsilon = 1/8$. (b) Schematic sketch of the λ - μ plane. Labels on lines of constant λ (vertical, blue) and μ (horizontal, red) correspond to panels of figure 3.4.	38
3.3	k_x - k_y plane showing the curve $D = 0$ intersecting $L_{1/4}$ (dark grey lattice) at the mode \mathbf{k}^+ (top row, for the boundary of the $T > 0$ region) or \mathbf{k}_- (bottom row, for the boundary of the $T < 0$ region). Typical configurations are shown for each regime of $\mathbf{k}_\pm(\lambda)$ detailed in (3.18) and (3.17), distinguished by colour. Panels labelled with black triangles correspond to the transitions between the different $\mathbf{k}_\pm(\lambda)$ regimes. The light grey square is $S_{1/4}$	40
3.4	Fraction of the total invariants that are contained within mode \mathbf{k}_\pm^+ as a function of (a) $\delta\mu$, or (b) $\delta\lambda$, for the representative points on the RJ boundary within each regime of \mathbf{k}_\pm^+ shown schematically in figure 3.2(b). $T > 0$ for the top row in parts (a) and (b) and $T < 0$ in the bottom row in both parts. Within each triptych, each panel represents a different system size ϵ	44
3.5	Sectors of \mathbf{k} -space labelled by the invariant spectrum that is dominant deep inside each sector. The grey square is $S_{1/8}$, whose left-hand edge intersects the isolines $E_{\mathbf{k}} = \Omega_{\mathbf{k}}$ and $E_{\mathbf{k}} = Z_{\mathbf{k}}$ at the points marked by \times and $+$ respectively.	45

3.6	CHM phase diagram for $\epsilon = 1/64$. (a) Sectors of the phase diagram are marked according to $(\text{sgn } T, \text{sgn } \mu, \text{sgn } \lambda)$, partitioned by the lines $\lambda = 0$ (thick blue), $\mu = 0$ (thick red), and $T, \mu, \lambda \rightarrow \infty$ (thick grey). Shaded areas suggest the boundary layer where one or two dominant invariants condense first. (b) The phase diagram with the RJ sail traversed by lines of constant λ (blue) and constant μ (red). (c) Upper right portion of the phase diagram, showing the lines $\lambda = \lambda_{\triangleleft}$ (solid blue), $\lambda_{\triangleleft} \pm 4 \times 10^{-5}$ (dashed blue), $\lambda_{\triangleleft} \pm 12 \times 10^{-5}$ (dotted blue), and $\mu = \mu_{\triangleleft}$ (solid red).	47
3.7	$\text{sgn } P(\alpha, \mathbf{k}_1, \mathbf{k}_2, \mathbf{k}')$ over \mathbf{k}' space for $L_\epsilon = 1/4$, $\alpha = 1/2$. We choose \mathbf{k}_1 and \mathbf{k}_2 so that P represents perturbations of the spectrum away from boundaries of the RJ sail in figure 3.6: (a) ∇ black boundary, (b) \triangleleft black boundary, (c) first segment of the lower brown boundary, (d) second segment of the lower brown boundary. The thick black or brown lines are contours of $P = 0$, white areas denote $P > 0$, and grey areas $P < 0$	50
3.8	Chemical potential μ as a function of the energy per particle $\mathcal{F} = \mathcal{E}/\mathcal{N}$ for an infinite-sized GPE system with high-wavenumber cutoff at $ \mathbf{k} = k_c$, in (a) 3D, and (b) 2D. For both dimensionalities the RJ spectrum has a positive and a negative (T, μ) branch. Condensation into a singular spectrum happens in 3D but not in 2D.	56
3.9	(a) Chemical potential μ vs. energy per particle $\mathcal{F} = \mathcal{E}/\mathcal{N}$ for a 2D GPE system of finite size, with high and low wavenumber cutoffs in k_x and k_y . The introduction of a finite box size induces a portion of $\mu < 0$ on the $T > 0$ branch of the RJ spectrum. (b) The curve of $D = 0$ moving through the k_x - k_y plane as μ swings from the $\mu < 0, T > 0$ branch of $n_{\mathbf{k}}^{\text{RJ}}$ (top panel), into the RJ-forbidden region (middle), and onto the $T < 0, \mu < -2$ branch of $n_{\mathbf{k}}^{\text{RJ}}$ (bottom). . . .	59
4.1	Schematic sketch of a spiral galaxy, embedded in a dark matter halo. In the fuzzy dark matter model, such a halo consists of a solitonic condensate of a self-gravitating scalar boson field that can be described by the Newtonian limit of the Schrödinger-Helmholtz equations. . .	65
4.2	An optical wave turbulence experiment using liquid crystal as the nonlocal nonlinear medium. The experimental setup is shown in (a). Results of numerical modelling of the system using the Schrödinger-Helmholtz equations is shown in (b). Note that the dynamics in this system occurred in one spatial direction, the x direction, and the z direction is analogous to time. In this chapter we carry out theoretical analysis of the wave turbulence of analogous optical systems in 2D. . . .	66

4.3	Particle flux $\eta(x)$ (in red) and energy flux $\epsilon(x)$ (in blue) as a function of spectral index x for the limits of the Schrödinger-Helmholtz model. Upper panels for the Schrödinger-Newton model in (a) $d = 3$, and (b) in $d = 2$. Lower panels for the nonlinear Schrödinger model in (c) $d = 3$, and (d) $d = 2$. Dashed lines indicate the signs of the fluxes when the spectral index takes the values x_{FN} and x_{FE}	76
4.4	Dual warm cascade in the 3D Schrödinger-Newton equations. The inverse particle cascade, with negative particle flux η , is shown in red. In blue is the direct energy cascade with positive flux ϵ . The black dashed line is the thermodynamic equipartition spectrum (4.11). (See main text for parameters.)	84
4.5	Sketch of the crossover from a warm cascade [which follows closely the thermodynamic spectrum (4.11) shown in black dashes] to a scale-free cascade, the latter with the Kolmogorov-Zakharov spectral indices shown, in the 3D Schrödinger-Helmholtz equations. The crossover happens around $\omega \approx \Lambda$, with the warm cascade in $\omega \gg \Lambda$ and the Kolmogorov-Zakharov cascade in $\omega \ll \Lambda$. Depending on placement of the forcing scale the crossover happens (a) in the inverse cascade (shown in red) or (b) in the direct cascade (shown in blue).	87
4.6	Double-peaked spectra representing a solution of the differential approximation model where particles are swept upscale (red curve) and energy downscale (blue curve) from forcing at ω_f at a zero value for the spectrum. Black dashed lines represent the two different thermodynamic spectra that match the middle of the two peaks of the spectrum. For parameters see main text.	99
5.1	Time series of the total waveaction (left), and the total energy (right), for two freely-evolving runs with the same initial condition and two different timesteps.	107
5.2	Dependence of the relative global waveaction (left) and energy (right) errors with timestep. The errors converge to zero as the timestep is reduced, at the empirical fitted rate stated, and indicated by the dashed line. For comparison, the expected convergence rate of $(\Delta t)^4$ is shown in by the black dotted line.	108
5.3	Freely-evolving run with the initial condition (5.9). First column: snapshots of $ \psi(\mathbf{x}, t) $. Second column: 1D waveaction spectra. Third column: spatio-temporal spectra.	109

5.4	Forced-dissipated run with forcing around $k_f = 32$ and hyperviscosity. Columns are as in figure 5.3. Note the appearance of a coherent structure in the $ \psi(\mathbf{x}) $ field, and its signature in the spatio-temporal spectra, from $t = 750$ onwards.	111
5.5	Time series of (a) the total waveaction, and scaled waveaction in the fundamental mode, and (b) the total, linear, and nonlinear energy for the forced-dissipated run. Vertical grey dots indicate $t = 710$, the approximate time of appearance of the condensate.	113

Acknowledgments

To my supervisor and friend Sergey Nazarenko. Thank you for the immeasurable support, encouragement, guidance, and patience you have given me over the years. I have learned so much from you, about wave turbulence, about science, about intellectual life, and about the meaning of generosity. I count myself very lucky indeed to have been your student.

Thanks also to Bogdan Hnat, with whom I started out on my PhD journey. I am very grateful indeed for the constant support and encouragement you have given me during my time at Warwick.

I thank Jason Laurie for providing the code with which I produced the numerical results in this thesis. I also thank Adam Griffin, Giorgio Krstulovic and Ying Zhu for many helpful discussions about the numerics.

I offer my profuse thanks to the staff of the Centre for Complexity Science for everything they have done for me during my time with them. In particular to Colm Connaughton for being such a font of knowledge, advice, and help about the science in this thesis, and the process of getting it done. And to all the CDT management team but particularly the administrators present and past: Jade Perkins, Debbie Walker, Heather Robson, and Jen Bowskill, who have done so much to make the Centre the friendly, welcoming, supportive place that it is. I will miss this place.

Thanks to all the friends who have shared the postgraduate journey with me; I won't ever think about my time at Warwick without fond thoughts of Adam, Aditi, Ayman, Bhavan, Diana, Ellen, Fede, Gian-Lorenzo, Katherine, K.B., Liz, Merve, Neil, Nick, Tom, and of course Jack.

Finally, thanks to my mum and dad Hung Yee and Malcolm, without whom none of this would be possible, and to Abi, without whom life would be nowhere near as sweet.

This work is dedicated to the memory of John Malcolm Robert Skipp.

Declarations

This thesis was written by me and does not contain any material that has been submitted for a degree at another university.

Chapters 1 and 2 contain no original work but provide the necessary conceptual and theoretical background to contextualise the work in chapters 3, 4, and 5. Chapter 3 is original work carried out by Sergey Nazarenko and me. It has been submitted for peer review, and at the time of submission of this thesis, it appears as pre-print [1]. Chapter 4 is original work carried out by Victor L'vov, and Sergey Nazarenko, and me. It has been published in [2]. Chapter 5 contains original work carried out by Sergey Nazarenko and me (the summary of numerical methods was composed by me but is not original). The numerical results were obtained using a numerical code originally written by Jason Laurie, and that I subsequently developed.

Abstract

This thesis explores different aspects of large-scale structure formation by turbulent processes. We work in the context of wave turbulence (WT): the statistical description of large ensembles of weakly nonlinear waves. There are two relevant aspects of WT theory that we focus on, and each different aspect is exemplified by a different equation of motion that we treat in the WT description.

The first aspect we explore is the WT description of absolute thermodynamic equilibria, including the phenomenon of condensation. Condensates of dynamical invariants into the fundamental mode of the system constitute the large-scale structures we seek to characterise. We study the equilibria and condensates of the Charney-Hasegawa-Mima (CHM) equation. The CHM equation is unique in WT theory as it possesses three adiabatic invariants, in contrast the two invariants in related models such as the 2D Euler equation, and the Gross-Pitaevskii equation. We explore how the third, anisotropic, invariant of the CHM system enriches the description of condensation, and show how both zonal flows and isotropic large-scale (and indeed small-scale) vortex condensates arise out of the equilibrium WT description of the CHM equation. We also discuss the role of negative thermodynamic potentials (viz. negative temperatures) in describing these states.

The second aspect of large-scale structure formation by WT processes is the dual cascade (in systems with two invariants) of particles, or waveaction, to large scale, and energy to small scale. We study the dual cascade in the Schrödinger-Helmholtz Equation (SHE) which is a new object of inquiry in WT theory. We examine the nature of the SHE dual cascade in two and three dimensions, and interpret the inverse cascade of particles as the nonequilibrium process of structure formation at large scales. We show that in both the fully local and fully nonlocal limits of the SHE, the inverse particle and direct energy fluxes are carried by small deviations from thermodynamic distributions, rather than the Kolmogorov-Zakharov cascades that are familiar in WT. We develop a differential approximation model to characterise such “warm cascade” states.

Finally we report initial results on direct numerical simulations of the SHE in two dimensions. These results are a numerical proof-of-concept demonstration that the general phenomenology of the dual cascade that we have characterised theoretically is qualitatively correct. We indicate the directions that a future research programme might take in fully characterising the SHE dual cascade numerically.

Abbreviations

1D One dimension(al)

2D Two dimension(al)

3D Three dimension(al)

CHM Charney-Hasegawa-Mima

ETDRK4 Exponential time-differencing fourth-order Runge-Kutta

FFT Fast Fourier Transform

GPE Gross-Pitaevskii equation

KZ Kolmogorov-Zakharov

NLS Nonlinear Schrödinger

PDF Probability density function

RHS Right-hand side

RJ Rayleigh-Jeans

RPA Random phases and amplitudes

SHE Schrödinger-Helmholtz equation

WT Wave turbulence

Chapter 1

Introduction

1.1 Wave turbulence vs. hydrodynamic turbulence

Wave behaviour is ubiquitous throughout the physical universe. Nature abounds in systems where oscillations spread across an extended system by wave motion, from density waves in the tenuous material that stretches between galaxies, to undulations in planet-sized atmospheric flows such as the jet stream, to the quantum mechanical de Broglie waves that describe matter at the smallest scale. Frequently a collection of waves will propagate through a system almost independently, slowly exchanging energy and other quantities, until finally the spectrum of the system has changed substantially through very many weak interactions. Wave turbulence [3, 4] is the mathematical study of such ensembles of interacting waves, and is the subject of this thesis.

The “turbulence” in wave turbulence (WT) makes reference to the deep similarity between WT and hydrodynamic turbulence. Although it is true that hydrodynamic turbulence is primarily concerned with the behaviour of vortices and eddies, with waves playing only a minor role, a checklist of its key features includes systems that are out of equilibrium, with many dynamical degrees of freedom (eddies at different spatial scales), interacting in a chaotic way (so that statistical quantities, rather than those garnered from individual realisations of the system, are important), such that the invariants of motion are transferred through the scales of the system. This is encapsulated in the most famous result of turbulence theory, that three-dimensional (3D) homogeneous, isotropic, Navier-Stokes turbulence has an energy spectrum that varies as

$$E_k^{(1D)} = C\varepsilon^{2/3}k^{-5/3} \quad (1.1)$$

where k is the modulus of the wavenumber \mathbf{k} . This is the Kolmogorov-Obukhov spectrum of turbulence [5, 6], and relates the statistically-defined energy spectrum

$E_k^{(1D)}$ (average kinetic energy of the flow in a shell of radius k in Fourier space, hence the (1D) in the superscript), to the spatial scale of the system $1/k$, on a distribution that realises the transfer of energy from forcing at large scale $1/k_f$, to dissipation at small scale $1/k_{\max}$. The forcing and dissipation scales are assumed to be widely separated, so that deep in the inertial range, i.e. at intermediate scales far removed from the forcing and dissipation ($k_f \ll k \ll k_{\max}$), the energy transfer happens via a local scale-by-scale cascade that is independent of the details of the forcing and dissipation. This is reflected in (1.1) remaining valid, with the same power law and prefactor $C \sim 1.6$, for every scale in the inertial range and no matter what fluid is realising the turbulence. The situation that (1.1) describes is clearly far from equilibrium as the spectrum is characterised by the energy injection rate ε (equal to the rate of energy flux through scales), rather than a thermodynamic temperature.

This checklist of features for hydrodynamic turbulence is also realised in ensembles of interacting waves, with many dynamical degrees of freedom (Fourier modes) interacting randomly, inducing a transfer of energy and other dynamically-conserved quantities through scales of the system, either from a setup of widely-separated, continuous forcing and dissipation, or evolving from an initial condition towards a final equilibrium. It is for this reason that the word “turbulence” can apply to a system of waves. Indeed, WT can be defined as the *out-of-equilibrium statistical mechanics of random nonlinear waves* [3].

The theory of WT is most fully developed when the waves are dispersive, and the nonlinear interactions between waves are weak. The latter crucially allows the hierarchy of moment equations derived from the original equation of motion of the system to be closed, giving a kinetic equation for the evolution of the wave spectrum, see chapter 2. Much of WT theory is concerned with finding solutions to such kinetic equations and examining their properties. Indeed, the analogy between WT and hydrodynamic turbulence was made clear in 1965 when Zakharov showed that there is a class of stationary solutions to certain kinetic equations that corresponds to the cascade of energy through scales [7]. These spectra are the WT equivalents as the Kolmogorov-Obukhov spectra (1.1), and are now known as the Kolmogorov-Zakharov (KZ) spectra. However, despite the importance of KZ spectra in the theory of WT, there are cases where the cascade of energy and other invariants through scales is *not* associated with KZ spectra. In this thesis we will consider two such examples.

The scope of systems that manifest WT behaviour is very broad. As a non-exhaustive list, WT has been applied to waves in Bose-Einstein condensates and superfluids [8–14], Kelvin waves on quantum vortex filaments [15–18], turbulence in nonlinear optics [19–22], waves on vibrating plates [23, 24], capillary and gravity waves on fluid surfaces [25–30], Rossby waves in planetary atmospheres and oceans,

and equally drift waves in magnetically confined fusion plasmas [31–40], Alfvén waves in magnetohydrodynamics [41–44], and gravitational waves in the early universe [45, 46]. In chapter 3 we will examine a model that describes Rossby and drift waves, and in chapter 4 we will turn to an equation that describes both a model of cosmological dark matter, and nonlinear optics in a nonlocal medium, depending on the spatial dimension.

1.2 Large-scale coherent structures in wave turbulence

In a situation where WT processes are transferring dynamical invariants across scales, invariants will accumulate over time at the scales they are being transferred to, if they are not removed from the system by some dissipation process. In the case where the system has two invariants, the situation generically involves a cascade of one invariant to small isotropic scales while the other moves to the largest isotropic scale in the system. Respectively these are known as the direct and inverse cascades, the combination of the two being known as the dual cascade. If there are three invariants, a triple cascade occurs, which can lead to the accumulation of an invariant at a large scale which is anisotropic.

To be specific, let us take the two-invariant case, typified by the Gross-Pitaevskii equation (GPE), also known as the nonlinear Schrödinger (NLS) equation, which is a canonical model that we will examine in detail in chapter 2. The GPE conserves both the energy and the number of particles or waveaction, and exhibits a dual cascade, with the energy cascading directly to small scales and the particles moving in an inverse cascade to large scales. This inverse cascade of particles leads to the accumulation of a large scale, strongly nonlinear, coherent structure: the condensate [8, 10–12, 19]. Once a condensate develops, it strongly influences the dynamics of the system, changing the nature of the dominant wave interactions in terms of the dispersion relation and the order of the wave interactions [8, 19].

The condensate could itself be either stable or unstable. In the latter case the instability of the condensate will lead to its fragmentation, the formation of solitary nonlinear structures, and their subsequent interaction with each other, and with the weakly nonlinear waves remaining in the system [19], possibly with the solitary structures merging until a single solitary wave remains within a sea of weak waves [3, 22]. The observation and characterisation of such a “WT life cycle” remains a tantalising goal of WT theory. Chapter 4 contains a fuller discussion of this prospect, in the context of a model closely related to the GPE: the Schrödinger-Helmholtz Equation (SHE).

The three-invariant case is typified by the Charney-Hasegawa-Mima (CHM) equation, which will be the subject of chapter 3. The CHM equation is a model

that is used to analyse both Rossby waves in planetary atmospheres and oceans, and drift waves in magnetically confined fusion plasmas. The large-scale structures of most interest that manifest in CHM systems are zonal flows: bands of highly anisotropic, alternating sheared flows that arise out of the WT [39, 47, 48]. Once the large-scale zonal flows form, they strongly suppress the transport of small-scale turbulence across them [37], which is important in the blocking of weather systems in mid latitudes in the geophysical application [49], and the trapping of heat and particles in the plasma core in the fusion case [47]. The zonal flows are coupled to the Rossby/drift waves in a co-evolving feedback loop wherein Rossby/drift turbulence generate the zonal flow, which suppresses the turbulence, leading to a saturation of the zonal flow [37].

In both cases described above, large-scale structure formation is the first step in a chain of processes that lead to rich, complex, multiscale behaviour. It is an ultimate goal of WT theory to describe and characterise all links in the chain, with the eventual aim of being an all-encompassing theory of not only weakly, but also strongly nonlinear turbulence, and to describe stages where weak and strong turbulence interact. Before this grand objective is realised, one must understand from as many points of view as possible, the initial phase of structure formation in the system being examined. Here, the most developed aspect of WT theory, weak WT, is invaluable in describing the mechanisms by which structure is accumulated at large scales.

1.3 Outline of this thesis

In this work we examine WT characteristics and processes that underlie the formation of large-scale structure in two different systems.

In chapter 3 we examine the formation of zonal flows and isotropic structures in the CHM equation from a rather classical point of view that has not previously been applied to CHM systems: that of examining the varieties of thermodynamic equilibria that the WT evolves towards. Here the fact that the WT of the CHM equation has three conserved quantities will play a vital role. We show that the presence of three invariants causes the varieties of equilibria of the CHM to be extremely rich, containing in particular limits zonal, large-scale isotropic, and small-scale isotropic condensates.

In chapter 4 we turn our attention to the SHE. This is the first time that this model has been examined within the framework of WT. We examine the cascade spectra by which SHE systems realise the dual cascade (upscale cascade of particles which creates large-scale structure, and direct cascade of energy to small scales). In particular we show that the KZ spectra are not able to realise the cascade. Instead,

we demonstrate that the energy and particles are carried by spectra that are very close to the thermal equilibrium spectra.

Finally, chapter 5 reports preliminary results on direct numerical simulations of the SHE. We describe a pseudospectral code and use it to explore scenarios similar to those described analytically in chapter 4. These results show qualitative agreement with the general scenario outlined in chapter 4 although quantitative agreement remains to be shown, in particular by employing a smaller timestep and moving to higher resolution. We detail a programme of work that we hope to embark upon in the future using this code, to improve on these initial results.

The work in each of these chapters is more or less self-contained, so rather than an overall conclusion to the thesis, each of chapters 3-5 ends with a comprehensive discussion of the results reported therein.

We proceed in chapter 2 to review the aspects of WT that are needed to contextualise the subsequent chapters.

Chapter 2

Theoretical Background

2.1 Equations studied in this thesis

In this thesis we will focus on two particular equations of motion for a field $\psi(\mathbf{x}, t)$. These equations are the Charney-Hasegawa-Mima (CHM) equation,

$$\frac{\partial}{\partial t} (\nabla^2 \psi - \rho^{-2} \psi) + \beta \frac{\partial \psi}{\partial x} + \left[\frac{\partial \psi}{\partial x} \frac{\partial \nabla^2 \psi}{\partial y} - \frac{\partial \psi}{\partial y} \frac{\partial \nabla^2 \psi}{\partial x} \right] = 0, \quad (2.1)$$

for which $\psi(\mathbf{x}, t)$ is real-valued, and the Schrödinger-Helmholtz equation,

$$i \frac{\partial \psi}{\partial t} + \nabla^2 \psi - V[|\psi|^2] \psi = 0, \quad (2.2a)$$

$$\nabla^2 V - \Lambda V = \gamma |\psi|^2, \quad (2.2b)$$

for which $\psi(\mathbf{x}, t)$ is complex. These equations are supplemented by some initial condition $\psi(\mathbf{x}, 0)$. In WT we usually consider the equations evolving in a periodic box of side length L in d spatial dimensions, \mathbb{T}_L^d . In this thesis we will be interested in the case $d = 2$ for the CHM equation, and $d = 2, 3$ for the SHE. We will describe in detail the physical contexts in which equations (2.1) and (2.2) appear, and the interpretations of their parameters and the dynamical variable $\psi(\mathbf{x}, t)$, in chapters 3 and 4 respectively. In those chapters, we will also make frequent reference to the Gross-Pitaevskii equation (GPE), also known as the nonlinear Schrödinger equation (NLS),

$$i \frac{\partial \psi}{\partial t} + \nabla^2 \psi + s |\psi|^2 \psi = 0, \quad (2.3)$$

which will be a constant touchstone for comparison as it is a canonical equation of study in WT. In (2.3), $\psi(\mathbf{x}, t)$ is complex, and the quantity $s = \pm 1$. Borrowing terminology from nonlinear optics, the case of (2.3) with $s = +1$ will be referred to as the focusing case, and $s = -1$ will be termed the defocusing case.

Before we embark on the study of (2.1) and (2.2), in this chapter we will

recapitulate certain established results which will be the starting points for our original investigations, using (2.3) as a reference point. Firstly in section 2.2 we state the quantities that are invariant under the action of (2.1)-(2.3). Next we derive the kinetic equation for the GPE in section 2.3, and indicate how the derivation changes when examining the CHM equation and the SHE. In section 2.4 we mention how the conserved quantities of the original equations (2.1)-(2.3) relate to invariants of the kinetic equation, and how an extra invariant of the CHM equation appears in the WT limit. Next we state the families of stationary solutions of the kinetic equation. Finally, we review the Fjørtoft argument which demonstrates robustly the dual cascade of energy and particles in the GPE and SHE, and indicate how it can be extended to three invariants.

The content that appears in this chapter is explored in far greater detail, in a pedagogical style, in book [3] and review [39].

2.2 Invariants of the GPE, SHE, and CHM

All the results of this thesis concern the cascade of the quadratic invariants of equations (2.1)-(2.3). Therefore we now state what these invariants are.

2.2.1 Conserved quantities of Schrödinger-type equations

The GPE (2.3) and SHE (2.2) are both examples of the generalised nonlinear Schrödinger equation

$$i\frac{\partial\psi}{\partial t} = -\nabla^2\psi + V[|\psi|^2]\psi, \quad (2.4)$$

c.f. (2.2a), with the generalised potential $V[|\psi|^2]$, which we assume to be real-valued. In the case of the GPE we have $V[|\psi|^2] = -s|\psi|^2$. For the SHE the potential is obtained by solving (2.2b); we write formally $V[|\psi|^2] = \gamma(\nabla^2 - \Lambda)^{-1}|\psi|^2$, where the inverse operator is understood to be explicitly defined in Fourier space, see section 4.3.1.

Equation (2.4) has two invariants that are the real-space integrals of positive quadratic quantities. These are the total waveaction, or number of particles,

$$\mathcal{N} = \int |\psi|^2 \, \mathrm{d}\mathbf{x}, \quad (2.5)$$

and the total energy, whose value is given by the Hamiltonian functional

$$\mathcal{H} = \int \left(|\nabla\psi|^2 + U[|\psi|^2] \right) \, \mathrm{d}\mathbf{x}, \quad (2.6)$$

where the integrals are taken over our domain \mathbb{T}_L^d . In (2.6) the potential energy

density $U[|\psi|^2]$ satisfies

$$U' \equiv \frac{d}{d|\psi|^2} U[|\psi|^2] = V[|\psi|^2].$$

For the GPE the potential energy density is $U[|\psi|^2] = -(s/2)|\psi|^4$, and for the SHE it is $U[|\psi|^2] = (\gamma/2)(\nabla^2 - \Lambda)^{-1}|\psi|^4$.

To demonstrate that \mathcal{N} is constant, we differentiate (2.5) with respect to time and substitute (2.4):

$$\dot{\mathcal{N}} = \int \left(\psi^* \frac{\partial \psi}{\partial t} + c.c. \right) d\mathbf{x} = \int \left[i (\psi^* \nabla^2 \psi - \psi^* V) + c.c. \right] d\mathbf{x},$$

where $c.c.$ denotes the complex conjugate. We integrate the first term on the RHS by parts, and use Gauss' theorem to give

$$\dot{\mathcal{N}} = \int \left[i (-|\nabla \psi|^2 - \psi^* V) + c.c. \right] d\mathbf{x} + \int \psi^* \nabla \psi \cdot d\mathbf{S} = 0$$

where the integrand in the first term is zero because it is a purely imaginary term plus its complex conjugate, and surface term vanishes because of the periodic boundary conditions (for the rest of this section we neglect writing out the surface terms generated by integration by parts). Thus we have that $\dot{\mathcal{N}} = 0$, i.e. the waveaction is conserved.

The conservation of \mathcal{H} follows in a similar way. Differentiating (2.6) with respect to time, we obtain

$$\begin{aligned} \dot{\mathcal{H}} &= \int \left[\frac{\partial}{\partial t} (\nabla \psi^* \cdot \nabla \psi) + U' \frac{\partial}{\partial t} (\psi^* \psi) \right] d\mathbf{x} \\ &= \int \left[(\nabla \dot{\psi}^* \cdot \nabla \psi + U' \dot{\psi}^* \psi) + c.c. \right] d\mathbf{x} \end{aligned}$$

Noting $U' = V$, and substituting for ψV using (2.4) we obtain

$$\begin{aligned} \dot{\mathcal{H}} &= \int \left[(\nabla \dot{\psi}^* \cdot \nabla \psi + c.c.) + (\dot{\psi}^* (i\dot{\psi} + \nabla^2 \psi) + c.c.) \right] d\mathbf{x} \\ &= \int \left[(\nabla \dot{\psi}^* \cdot \nabla \psi + \dot{\psi}^* \nabla^2 \psi) + c.c. \right] d\mathbf{x} \\ &= 0, \end{aligned}$$

where the final equality follows by integrating the $\dot{\psi}^* \nabla^2 \psi$ term by parts. Thus, we have explicitly demonstrated that \mathcal{H} is conserved.

Alternatively, we can simply note the Hamiltonian structure of the gener-

alised NLS equation: we recover (2.4) via Hamilton's equation

$$i \frac{\partial \psi}{\partial t} = \frac{\delta \mathcal{H}}{\delta \psi^*}. \quad (2.7)$$

Conservation of \mathcal{H} immediately follows by noting that it has no explicit time dependence. To see that (2.7) is equivalent to (2.4), we once again integrate by parts to rewrite the first term under the integral in (2.6) as $-\psi^* \nabla^2 \psi$. Varying \mathcal{H} with respect to ψ^* , we get

$$\begin{aligned} \frac{\delta \mathcal{H}}{\delta \psi^*} &= \frac{\delta}{\delta \psi^*} \int \left(-\psi^* \nabla^2 \psi + U[|\psi|^2] \right) \mathrm{d}\mathbf{x} \\ &= -\nabla^2 \psi + U'[|\psi|^2] \psi. \end{aligned}$$

Noting that $U' = V$, we obtain the right-hand side of (2.4).

The generalised NLS also conserves the total momentum

$$\mathbf{P} = -2i \int (\psi^* \nabla \psi - \psi \nabla \psi^*) \mathrm{d}\mathbf{x}. \quad (2.8)$$

However this is not a positive-definite quantity, and as we will see in section 2.6, the key to understanding cascades is the observation that every positive-definite invariant imposes restrictions on where the other such invariants may move in \mathbf{k} -space.

To summarise, we have demonstrated explicitly that the generalised NLS equation (2.4) conserves the quadratic invariants \mathcal{N} and \mathcal{H} . We have also shown that the equation can be written in Hamiltonian form (2.7). In particular, these properties apply to two of our equations of interest, the GPE and the SHE. We now turn to our other equation of interest, the CHM equation.

2.2.2 Conserved quantities in the CHM equation

The CHM equation (2.1) also conserves two invariants. These are the energy

$$E = \frac{1}{2} \int [(\nabla \psi)^2 + \rho^{-2} \psi^2] \mathrm{d}\mathbf{x} \quad (2.9)$$

and the enstrophy

$$\Omega = \frac{1}{2} \int (\nabla^2 \psi - \rho^{-2} \psi)^2 \mathrm{d}\mathbf{x}. \quad (2.10)$$

As in the previous section, the conservation of E and Ω can be proved by differentiating them with respect to time, substituting (2.1), judicious integration by parts, and using the periodic boundary conditions. We neglect reproducing the proofs here.

Unlike the GPE and the SHE, the CHM equation is not equivalent to Hamil-

ton's equation (2.7) with the Hamiltonian given by the energy. Nevertheless it does have Hamiltonian structure when expressed in the correct variables, as we will see in section 2.3.2.

2.3 Derivation of the (four-wave) kinetic equation

Having established our equations of study, and the quantities that they conserve, we now turn to the subject of turbulence. As mentioned in chapter 1, turbulence is characterised by the excitation of a large number of degrees of freedom, interacting with a high degree of spatio-temporal complexity. In such a situation it is natural to consider a statistical description of the system. In particular, one wishes to study correlation functions: products of the field values at different points in the system, averaged in a suitable way. The assumption of homogeneity of the turbulence relates correlation of the fields at different spatial points to correlations in Fourier space. Thus the first step in setting up a description of turbulence is to take moments of the equation of motion, obtaining evolution equations for the moments.

In general, statistical descriptions of turbulence are at this point hampered by the closure problem. Namely, the nonlinear term in the equation of motion couples low-order moments to higher-order moments. This is the point where the uniqueness and utility of WT expresses itself: when one makes a certain assumption about the statistical distribution of the Fourier modes (see section 2.3.4), then when one takes the limit of a large domain and weak nonlinearity, it is possible to close the hierarchy of moment equations in an asymptotically correct, self-consistent way [3, 4].

The majority of WT studies usually consider the evolution of the lowest, second-order, moment of the probability density function (PDF), known as the waveaction spectrum. This is the moment that is most easily measured in experiments, and is the variable of interest when studying cascades of quadratic invariants, which is the subject of this thesis. However higher moments, or even the full PDF, are mathematically accessible thanks to the self-consistent closure properties of WT [3, 50–52].

In this section we derive the wave kinetic equation that governs the evolution of the waveaction spectrum (2.20), using the procedure detailed in [3]. As a concrete example we will derive the kinetic equation for the GPE. We will point out at which points the derivation must be modified to obtain the kinetic equation for the SHE and CHM.

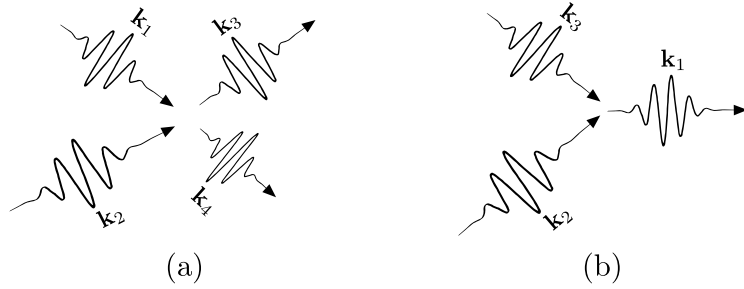


Figure 2.1: Schematic sketch of (a) 4-wave interactions of the $2 \leftrightarrow 2$ type, and (b) 3-wave interactions of $2 \leftrightarrow 1$ type.

2.3.1 Fourier space representation

Firstly we express the dynamical variable in terms of Fourier variables via

$$\psi(\mathbf{x}, t) = \sum_{\mathbf{k}} \psi_{\mathbf{k}} e^{i\mathbf{k} \cdot \mathbf{x}} \quad \Leftrightarrow \quad \psi_{\mathbf{k}}(t) = \frac{1}{L^d} \int \psi(\mathbf{x}, t) e^{-i\mathbf{k} \cdot \mathbf{x}} d\mathbf{x} \quad (2.11)$$

where the \mathbf{k} -space sum is over all wavenumbers $\mathbf{k} = 2\pi\mathbf{l}/L$ and \mathbf{l} ranges over the discrete lattice of integers in d -dimensional space \mathbb{Z}^d . The \mathbf{x} -space integral is again over \mathbb{T}_L^d .

Thus in terms of $\psi_{\mathbf{k}}(t)$, the GPE (2.3) reads

$$i \frac{\partial \psi_{\mathbf{k}}}{\partial t} = k^2 \psi_{\mathbf{k}} - \sum_{123} W_{3\mathbf{k}}^{12} \psi_1 \psi_2 \psi_3^* \delta_{12}^{3\mathbf{k}} \quad (2.12)$$

where we have introduced the shorthand notation $\psi_j = \psi_{\mathbf{k}_j}$, $\sum_{i\dots j} = \sum_{\mathbf{k}_i, \dots, \mathbf{k}_j}$, and $\delta_{12}^{3\mathbf{k}} = \delta(\mathbf{k}_1 + \mathbf{k}_2 - \mathbf{k}_3 - \mathbf{k})$ is the Kronecker delta, equal to unity if its argument is zero, and zero otherwise. For the GPE the 4-wave interaction coefficient $W_{3\mathbf{k}}^{12} = -s$.

If the second term on the RHS of (2.12) is zero then the equation is linear, and expresses waves with dispersion relation $\omega_{\mathbf{k}} = k^2$ propagating through the domain without interacting.

The nonlinearity on the RHS expresses 4-wave interactions of the $2 \leftrightarrow 2$ type, sketched schematically in figure 2.1(a). This interaction happens between all modes $\mathbf{k}_1, \mathbf{k}_2, \mathbf{k}_3, \mathbf{k}$ that are in wavenumber resonance, as expressed by the Kronecker delta $\delta_{12}^{3\mathbf{k}}$. The strength of this interaction is given by the 4-wave interaction coefficient $W_{3\mathbf{k}}^{12}$ which is generally a function of the wavenumbers involved, see its expression for the SHE in equation (4.5d).

For the CHM equation, the nonlinear term in (2.1) is quadratic in $\psi(\mathbf{x}, t)$. Thus the wave interaction is between three waves, shown schematically in figure 2.1(b), which are necessarily of $2 \leftrightarrow 1$ type. The CHM dispersion relation is given in equation (3.2).

2.3.2 Waveaction variable and the Hamiltonian formulation

As alluded to above, most equations considered in WT have Hamiltonian structure. Generally in WT we write Hamiltonians in terms of the waveaction variable $a_{\mathbf{k}}$. For the Schrödinger-type equations (2.3) and (2.2) we have simply $a_{\mathbf{k}} = \psi_{\mathbf{k}}$. For the CHM equation (2.1),

$$a_{\mathbf{k}} = \frac{1 + \rho^2 k^2}{\sqrt{\beta \rho^4 |k_x|}} \psi_{\mathbf{k}}.$$

In terms of the waveaction variable, Hamilton's equation reads

$$i \frac{\partial a_{\mathbf{k}}}{\partial t} = \frac{\partial H}{\partial a_{\mathbf{k}}^*}, \quad (2.13)$$

where the Hamiltonian can be decomposed as

$$H = H_2 + H_3 + H_4 + \dots \quad (2.14)$$

The quadratic Hamiltonian is

$$H_2 = \sum_{\mathbf{k}} \omega_{\mathbf{k}} a_{\mathbf{k}} a_{\mathbf{k}}^*,$$

where $\omega_{\mathbf{k}}$ is the dispersion relation of the system. Thus if the series (2.14) is ordered $H_2 \gg H_3, H_4, \dots$, as is the case in weak WT, the quadratic Hamiltonian leads to linear waves and the interaction Hamiltonians H_3, H_4, \dots represent perturbations of the linear waves by the wave-wave interactions.

The cubic Hamiltonian is generically

$$H_3 = \sum_{123} (V_{12}^3 a_1 a_2 a_3^* \delta_{12}^3 + c.c.). \quad (2.15)$$

For the GPE and SHE the interaction Hamiltonian is quartic so $H_3 = 0$. For the CHM equation, which is of 3-wave type, H_3 is the interaction Hamiltonian. The 3-wave interaction coefficient $V_{12}^{\mathbf{k}}$ for the CHM equation is given in (3.5). (Note that in order to derive (3.5) one must also impose the frequency resonance condition $\omega_{\mathbf{k}} = \omega_1 + \omega_2$, see [53]. However for our purpose, the derivation of the WT kinetic equation, this requirement is not at all restrictive as the kinetic equation enforces interactions between waves that lie on the resonant manifold for which the frequency resonance condition is true.)

In addition, for the CHM $\psi(\mathbf{x}, t)$, and hence $a(\mathbf{x}, t)$ is real. This imposes the condition $a_{\mathbf{k}}^* = a_{-\mathbf{k}}$. In this case, in order for H_3 to be real (as it must be to relate

to the energy), the 3-wave interaction coefficient has the following symmetries:

$$V_{12}^3 = V_{21}^3 = (V_{3,-1}^2)^* = (V_{-1,-2}^{-3})^*.$$

Only the first of these symmetries is true in the general case where $a(\mathbf{x})$ is complex.

The quartic Hamiltonian for 4-wave interactions of $2 \leftrightarrow 2$ type,

$$H_4 = \frac{1}{2} \sum_{1234} W_{34}^{12} a_1 a_2 a_3^* a_4^* \delta_{12}^{34}, \quad (2.16)$$

is the interaction Hamiltonian for the GPE and SHE in two and three dimensions (2D and 3D respectively), and is zero for the CHM equation.

As H_4 is real, we require the following symmetries of the interaction coefficient:

$$W_{34}^{12} = W_{34}^{21} = W_{43}^{12} = (W_{12}^{34})^*. \quad (2.17)$$

It is important to note that in (2.16), the diagonal terms in the sum result in a term that is quadratic in $a_{\mathbf{k}}$. This contributes a term to H_2 and leads to a nonlinear frequency shift

$$\omega_{\mathbf{k}}^{\text{NL}} = 2 \sum_{\mathbf{k}_1} W_{1\mathbf{k}}^{1\mathbf{k}} |a_1|^2 \quad (2.18)$$

to the dispersion relation, so that the wave equation for $2 \leftrightarrow 2$ interactions becomes

$$i\partial_t a_{\mathbf{k}} = \tilde{\omega}_{\mathbf{k}} a_{\mathbf{k}} + \sum'_{123} W_{34}^{12} a_1 a_2 a_3^* \delta_{12}^{\mathbf{k}3} \quad (2.19)$$

where the renormalised frequency is $\tilde{\omega}_{\mathbf{k}} = \omega_{\mathbf{k}} + \omega_{\mathbf{k}}^{\text{NL}}$, and the accented sum \sum'_{123} excludes the diagonal terms where $\mathbf{k}_1 = \mathbf{k}_3$ or $\mathbf{k}_2 = \mathbf{k}_3$. This frequency renormalisation is the leading nonlinear effect on the wave dynamics. For the GPE the nonlinear frequency shift is independent of \mathbf{k} and is simply $\omega_{\mathbf{k}}^{\text{NL}} = -2s \sum_{\mathbf{k}_1} |a_1|^2$. In 3-wave systems there is no frequency renormalisation because there are no diagonal terms in H_3 that would contribute to H_2 .

The waveaction spectrum is defined in terms of the waveaction variables that appear in the Hamiltonian. The spectrum is

$$n_{\mathbf{k}}(t) = \left(\frac{L}{2\pi} \right)^d \langle |a_{\mathbf{k}}(t)|^2 \rangle, \quad (2.20)$$

where $\langle \dots \rangle$ denotes ensemble averaging with respect to independent realisations of the system, see section 2.3.4 (in practice it is usual to assume ergodicity of the dynamics and replace the ensemble average by the time average of one realisation, particularly when examining steady-state WT). The end goal of this derivation is to find the wave kinetic equation for the evolution of this spectrum.

2.3.3 Interaction variable and asymptotic expansion

For weakly nonlinear waves, we expect the Fourier mode $a_{\mathbf{k}}(t)$ to oscillate rapidly with frequency $\tilde{\omega}_{\mathbf{k}}$, while its amplitude envelope slowly changes due to the nonlinear interactions. In order to capture these dynamics in the kinetic equation, we write $a_{\mathbf{k}}(t)$ as a perturbation series in a smallness parameter ϵ (at least in principle; in practice we will actually work with a new variable $b_{\mathbf{k}}(t)$, see (2.21) below). Solving for each required term in the series leads to the appearance of secular terms, i.e. terms that grow proportionally with time. As we will see, the growth of these terms comes about because of the nonlinear resonance between different orders of the solution. Indeed, the secular terms represent the dynamics we are trying to capture: the slow growth of the spectrum due to nonlinear wave interactions.

To account mathematically for the secular terms, some authors choose to derive the kinetic equation using the method of multiple timescales, see e.g. review [54] and references therein. This involves replacing the dynamical variables $a_{\mathbf{k}}(t)$ (and hence $b_{\mathbf{k}}(t)$ and finally the spectrum $n_{\mathbf{k}}(t)$) with new variables $a_{\mathbf{k}}(T_0, T_1, \dots)$ etc., that are functions of multiple independent time variables T_0, T_1, \dots . The assumption that these timescales are well-separated, $T_n = \epsilon^n T_0$, requires a consistency condition that relates the secular terms to the derivative of the spectrum with respect to the appropriate slow time variable. This consistency condition *is*, in fact, the kinetic equation. For a pedagogical overview of the multiple timescale method as it applies to the derivation of a WT kinetic equation, see [39].

Here, rather than proceeding with the derivation via the method of multiple timescales, we will instead follow the method detailed in [3]. Again, we make the assumption that the linear wave oscillations are fast and well-separated in timescale from the slow growth of the spectrum. In order for this assumption to be consistent, we will again need to define the time derivative of the spectrum in terms of a slow timescale. In contrast to the method of multiple timescales though, we make use of only one time variable. We will also employ an auxiliary intermediate timescale to probe the dynamics in between the linear and nonlinear times. Thus, while there are some technical differences between this method and the method of multiple timescales, they are very similar spirit, and indeed they both obtain exactly the same kinetic equation in the end. However to our knowledge there is no explicit demonstration of precisely how the two methods correspond to each other, and we do not attempt to give one here.

We proceed by first writing (2.19) in terms of the so-called interaction variable,

$$b_{\mathbf{k}} = \frac{1}{\sqrt{\epsilon}} a_{\mathbf{k}} e^{i\tilde{\omega}_{\mathbf{k}} t}. \quad (2.21)$$

Here ϵ is a book-keeping parameter that measures the weakness of the nonlinearity.

When we assume the nonlinearity is weak ($\epsilon \ll 1$), $b_{\mathbf{k}}$ becomes stationary to leading order and evolves only over the nonlinear timescale, which we will shortly define in (2.23). The scaling $1/\sqrt{\epsilon}$ is determined by the fact that the nonlinearity in the GPE is cubic, and because we choose to have the timescales (2.23) and (2.24) scale with ϵ as they do. In the case of the CHM equation, which has a quadratic nonlinearity, there would instead be a factor of $1/\epsilon$ in (2.21).

In terms of $b_{\mathbf{k}}$, equation (2.19) becomes for the GPE

$$i\partial_t b_{\mathbf{k}} = -\epsilon s \sum_{123} b_1 b_2 b_3^* e^{i\omega_{12}^{3\mathbf{k}} t} \delta_{12}^{3\mathbf{k}} \quad (2.22)$$

where $\omega_{12}^{3\mathbf{k}} = \tilde{\omega}_3 + \tilde{\omega}_{\mathbf{k}} - \tilde{\omega}_1 - \tilde{\omega}_3$. For the GPE the nonlinear frequency shift is independent of \mathbf{k} and so cancels out, meaning we can drop the tildes in $\omega_{12}^{3\mathbf{k}}$. For the SHE and more general 4-wave systems the tildes will be retained, also the sum in (2.22) will contain a factor of $W_{3\mathbf{k}}^{12}$. Likewise the equivalent of (2.22) for the 3-wave systems like the CHM will contain $V_{12}^{\mathbf{k}}$.

We now define the timescales involved. The linear timescale is the linear wave period $\tau_L \sim 2\pi/\omega_{\mathbf{k}}$. The nonlinear timescale is

$$\tau_{\text{NL}} \sim \tau_L/\epsilon^2, \quad (2.23)$$

whose ϵ -scaling will be justified *a posteriori*. The linear and nonlinear timescales become well-separated in the weakly nonlinear limit $\epsilon \ll 1$. We now consider an auxiliary intermediate timescale T such that $\tau_L \ll T \ll \tau_{\text{NL}}$, in particular we simply take

$$T \sim \tau_L/\epsilon. \quad (2.24)$$

Next we seek a solution for $b_{\mathbf{k}}(T)$ by using the perturbation expansion

$$b_{\mathbf{k}}(t) = b_{\mathbf{k}}^{(0)}(t) + \epsilon b_{\mathbf{k}}^{(1)}(t) + \epsilon^2 b_{\mathbf{k}}^{(2)}(t) \quad (2.25)$$

recursively in (2.22) and integrating up to time T . At zeroth order in ϵ we get $b_{\mathbf{k}}^{(0)}(T) = b_{\mathbf{k}}(0)$ which we write as simply $b_{\mathbf{k}}$ for compactness (dropping the order label and time argument when considering quantities at $t = 0$).

At order ϵ we have at $t = T$

$$b_{\mathbf{k}}^{(1)}(T) = i \sum_{123} s b_1 b_2 b_3^* \delta_{12}^{3\mathbf{k}} \Delta_T(\omega_{12}^{3\mathbf{k}}) \quad (2.26)$$

where $\Delta_T(\omega_{12}^{3\mathbf{k}}) = \int_0^T e^{i\omega_{12}^{3\mathbf{k}} t} dt = (e^{i\omega_{12}^{3\mathbf{k}} T} - 1)/i\omega_{12}^{3\mathbf{k}}$ (note that the restriction on the sum in (2.26) excludes combination of modes that make $\omega_{12}^{3\mathbf{k}} = 0$).

At order ϵ^2 we obtain

$$b_{\mathbf{k}}^{(2)}(T) = \sum_{123456} \left[b_1 b_2 b_6 b_4^* b_5^* \delta_{45}^{36} \delta_{12}^{3\mathbf{k}} E_T(\omega_{126}^{\mathbf{k}45}, \omega_{12}^{3\mathbf{k}}) - 2b_1 b_4 b_5 b_3^* b_6^* \delta_{45}^{26} \delta_{12}^{3\mathbf{k}} E_T(\omega_{145}^{\mathbf{k}36}, \omega_{12}^{3\mathbf{k}}) \right] \quad (2.27)$$

where $E_T(x, y) = \int_0^T \Delta_t(x - y) e^{iyt} dt$, and $\omega_{126}^{\mathbf{k}45} = \omega_{12}^{3\mathbf{k}} + \omega_{36}^{45}$, and we have used $s^2 = 1$.

With these expressions for the terms in the expansion (2.25) we can now find the waveaction spectrum (2.20), which in terms of the interaction variables is

$$n_{\mathbf{k}}(T) = \epsilon \left(\frac{L}{2\pi} \right)^d \langle |b_{\mathbf{k}}(T)|^2 \rangle \quad (2.28)$$

(the ϵ scaling is determined by (2.21)). Expanding the square in the RHS we have

$$\langle |b_{\mathbf{k}}(T)|^2 \rangle = \langle |b_{\mathbf{k}}|^2 \rangle + \epsilon \underbrace{\langle b_{\mathbf{k}}^{(1)}(T) b_{\mathbf{k}}^* + c.c. \rangle}_{\langle X \rangle} + \epsilon^2 \underbrace{\langle |b_{\mathbf{k}}^{(1)}(T)|^2 \rangle}_{\langle Y \rangle} + \epsilon^2 \underbrace{\langle b_{\mathbf{k}}^{(2)}(T) b_{\mathbf{k}}^* + c.c. \rangle}_{\langle Z \rangle}. \quad (2.29)$$

For future reference we write out the moments of $b_{\mathbf{k}}$ in the highlighted terms above, collecting the Kronecker δ , and factors of Δ_T and E_T , into the (...), and state explicitly which wavenumbers are omitted in the sums (these excluded wavenumbers were the diagonal terms that gave rise to the nonlinear frequency correction in (2.18)).

$$\langle X \rangle = \sum_{\substack{\mathbf{k}_1 \neq \mathbf{k}_3 \\ \mathbf{k}_2 \neq \mathbf{k}_3}} [\langle b_1 b_2 b_3^* b_{\mathbf{k}}^* \rangle(\dots) + c.c.], \quad (2.30a)$$

$$\langle Y \rangle = \sum_{\substack{\mathbf{k}_1, \mathbf{k}_2 \neq \mathbf{k}_3 \\ \mathbf{k}_4, \mathbf{k}_5 \neq \mathbf{k}_6}} \langle b_1 b_2 b_6 b_3^* b_4^* b_5^* \rangle(\dots), \quad (2.30b)$$

$$\langle Z \rangle = \sum_{\substack{\mathbf{k}_1, \mathbf{k}_2 \neq \mathbf{k}_3 \\ \mathbf{k}_4, \mathbf{k}_5 \neq \mathbf{k}_6}} [\langle b_1 b_2 b_6 b_4^* b_5^* b_{\mathbf{k}}^* \rangle(\dots) - 2\langle b_1 b_4 b_5 b_3^* b_6^* b_{\mathbf{k}}^* \rangle(\dots) + c.c.]. \quad (2.30c)$$

We see that in order to know the spectrum we need to know the moments of the PDF up to sixth order. This demonstrates the closure problem of turbulence. Next we will develop a statistical closure that will express these higher moments in terms of second-order moments.

2.3.4 Statistical closure

Our statistical closure involves making an assumption about the statistics of the initial wave field: that all Fourier modes have random phases and amplitudes (RPA). Writing the Fourier modes as $b_{\mathbf{k}} = B_{\mathbf{k}} \varphi_{\mathbf{k}}$, the RPA assumption is that the am-

plitudes $B_{\mathbf{k}} \in \mathbb{R}^+$ of each mode are statistically independent, and that the phase factors $\varphi_{\mathbf{k}} = e^{i\phi_{\mathbf{k}}} \in \mathbb{S}^1$ are also independent, and uniformly distributed on \mathbb{S}^1 , the unit circle in the complex plane, i.e. the phase itself $\phi_{\mathbf{k}}$ is uniformly distributed on $[0, 2\pi)$.

Thus the averaging over Fourier modes in (2.28) onwards means averaging over amplitudes and phases, $\langle \dots \rangle = \langle \langle \dots \rangle_B \rangle_{\varphi}$. With the RPA assumption, these can be done independently, as the amplitudes and phases are statistically independent, for example,

$$\langle b_1 b_2 b_3^* b_4^* \rangle = \langle B_1 B_2 B_3^* B_4^* \rangle_B \langle \varphi_1 \varphi_2 \varphi_3^* \varphi_4^* \rangle_{\varphi}. \quad (2.31)$$

We now show that the random phase assumption allows us to reduce the order of the moments appearing in (2.28). Consider the average of the n -th power of the phase factor $\varphi_{\mathbf{k}}$. As $\varphi_{\mathbf{k}}$ is uniformly distributed in \mathbb{S}^1 , so too will $\varphi_{\mathbf{k}}^n$ be, meaning we have $\langle \varphi_{\mathbf{k}}^n \rangle_{\varphi} = 0$ unless $n = 0$, in which case we have $\langle 1 \rangle_{\varphi} = 1$. Now, because the phases are independent, we can factorise the average of a product of phase factors into the product of averages, $\langle \varphi_1 \varphi_2 \rangle_{\varphi} = \langle \varphi_1 \rangle_{\varphi} \langle \varphi_2 \rangle_{\varphi}$. This will vanish unless $\mathbf{k}_1 = \mathbf{k}_2$, and the phase factors are complex conjugates of each other, i.e. we have $\langle \varphi_1 \varphi_2^* \rangle = \delta_2^1$. Extending this to the product in (2.31), the only terms that survive phase averaging are those where the phase factors appear in complex conjugate pairs (this result is known as Wick's rule):

$$\langle b_1 b_2 b_3^* b_4^* \rangle_{\varphi} = B_1 B_2 B_3^* B_4^* \langle \varphi_1 \varphi_2 \varphi_3^* \varphi_4^* \rangle_{\varphi} = B_1^2 B_2^2 (\delta_3^1 \delta_4^2 + \delta_4^1 \delta_3^2) - B_1^4 \delta_3^1 \delta_4^1 \delta_2^1 \quad (2.32a)$$

where in the last step we have used the Kronecker delta replacement rule in the amplitude subscripts (and the superscripts on the B variables denote powers). The last term in (2.32a) prevents double-counting in the case that all wavenumbers are equal. When the amplitude average is taken, this term will lead to the fourth-order cumulant, which measures the departure of the amplitude distribution away from Gaussianity. We will neglect this term as the extra Kronecker delta means that when we take the partial sum over N wave modes, the contribution of this term will be smaller by that of the other terms by a factor of $\mathcal{O}(1/N)$. This is what allows us to close the moment hierarchy at second order.

Similarly we can write the phase-averaged sixth-order moment as

$$\langle b_1 b_2 b_3 b_4^* b_5^* b_6^* \rangle_{\varphi} = B_1^2 B_2^2 B_3^2 [(\delta_4^1 \delta_5^2 \delta_6^3 + \dots) + \delta_5^1 \delta_6^2 \delta_4^3 + \delta_6^1 \delta_5^2 \delta_4^3] - \text{cumulant} \quad (2.32b)$$

where the \dots stands for the three remaining terms where the indices of three Kronecker δ 's are permuted, and again we neglect the cumulant in (2.32b)

Substituting (2.32a) into (2.30a), we see that in fact no term in the fourth-order moment in fact realised, due to the restrictions on the sum. Therefore there is no contribution from $\langle X \rangle$, the $\mathcal{O}(\epsilon)$ term in (2.29), to the spectrum at time T .

This term has vanished because of the averaging over random phases: the wave field at wavenumber \mathbf{k} is being pushed and pulled by other modes via nonlinear interactions at random phases in its oscillation, so that after time T has elapsed the net contribution to the spectrum at this order is zero. This result is crucial as it means we must go to the next order, ϵ^2 , to find terms that contribute to the evolution of the spectrum. This justifies the scaling (2.23) of the nonlinear timescale.

Turning to (2.32b) and permuting indices appropriately, we see that the term in round parentheses does not contribute due to the restrictions on the sum in (2.30b). The remaining terms contract the sum to three wavenumbers, giving the contribution to the $\mathcal{O}(\epsilon^2)$ term in (2.29)

$$\langle Y \rangle_\varphi = 2 \sum_{123} B_1^2 B_2^2 B_3^2 \delta_{12}^{3\mathbf{k}} |\Delta_T(\omega_{12}^{3\mathbf{k}})|^2. \quad (2.33a)$$

Similarly, substituting (2.32b) into (2.30c), we find that the surviving contribution at $\mathcal{O}(\epsilon^2)$ is

$$\langle Z \rangle_\varphi = 4 \sum_{123} B_{\mathbf{k}}^2 (B_1^2 B_2^2 - B_1^2 B_3^2 - B_2^2 B_3^2) \delta_{12}^{3\mathbf{k}} \Re [E_T(0, \omega_{12}^{3\mathbf{k}})]. \quad (2.33b)$$

Next we carry out the amplitude averaging, and use the fact that amplitudes are independent to factorise the second-order moments, i.e. $\langle B_1^2 B_2^2 B_3^2 \rangle_B = \langle B_1^2 \rangle_B \langle B_2^2 \rangle_B \langle B_3^2 \rangle_B$. and convert the second-order moments to spectra via (2.28).

2.3.5 Large box and weak nonlinearity limit

To complete the derivation of the kinetic equation, we take the large box limit $L \rightarrow \infty$, which converts sums over discrete wavenumbers to integrals over \mathbf{k} -space, and Kronecker δ 's to Dirac δ functions, via the replacements

$$\sum_{123} \rightarrow \left(\frac{L}{2\pi}\right)^{3d} \int d\mathbf{k}_1 d\mathbf{k}_2 d\mathbf{k}_3, \quad \text{Kronecker-}\delta \rightarrow \left(\frac{2\pi}{L}\right)^d \times \text{Dirac-}\delta.$$

Finally we take the small nonlinearity limit $\epsilon \rightarrow 0$. By the definition of the auxiliary time T , equation (2.24), the small nonlinearity limit corresponds to sending $T \rightarrow \infty$. The T dependence is only found in the functions $|\Delta_T(x)|^2$ and $\Re[E_T(0, x)]$. It can be shown that

$$\lim_{T \rightarrow \infty} |\Delta_T(x)|^2 = 2\pi T \delta(x) \quad \text{and} \quad \lim_{T \rightarrow \infty} \Re[E_T(0, x)] = \pi T \delta(x) \quad (2.34)$$

i.e. both surviving $\mathcal{O}(\epsilon^2)$ terms (2.33a) and (2.33b) are proportional to T .

Putting all these results together, we find that the spectrum at time T is

$$\begin{aligned} n_{\mathbf{k}}(T) &= \epsilon \left(\frac{L}{2\pi} \right)^d \langle |b_{\mathbf{k}}(T)|^2 \rangle \\ &= n_{\mathbf{k}}(0) + 4\pi T \int \delta_{12}^{3\mathbf{k}} \delta(\omega_{12}^{3\mathbf{k}}) n_1 n_2 n_3 n_{\mathbf{k}} \left[\frac{1}{n_{\mathbf{k}}} + \frac{1}{n_3} - \frac{1}{n_1} - \frac{1}{n_2} \right] d\mathbf{k}_1 d\mathbf{k}_2 d\mathbf{k}_3. \end{aligned}$$

As discussed at the start of section 2.3.3, we see that the spectrum grows due to the secular terms that arise at order ϵ^2 in the perturbation series (2.29). These secular terms are a result of resonances: the delta functions $\delta_{12}^{3\mathbf{k}}$ and $\delta(\omega_{12}^{3\mathbf{k}})$ restrict the support of the integrand to the resonant manifold

$$\mathbf{k} + \mathbf{k}_3 - \mathbf{k}_1 - \mathbf{k}_2 = 0, \quad \omega_{\mathbf{k}} + \omega_3 - \omega_1 - \omega_2 = 0. \quad (2.35)$$

Note though that the resonant manifold is broadened by nonlinearity, and quasi resonances with frequency mismatch $\omega_{12}^{3\mathbf{k}} = \Gamma$ will also contribute to the evolution of the spectrum (Γ is the nonlinear frequency broadening, and is approximately the inverse of the nonlinear timescale). The fact that we take the $L \rightarrow \infty$ limit first ensures that the modes become dense in \mathbf{k} -space before we send $\epsilon \rightarrow 0$, so many quasi-resonant modes fit within the nonlinear frequency broadening, before the weakly nonlinear limit is taken.

The final step is to form the time derivative of the spectrum. We have $T \ll \tau_{\text{NL}}$, i.e. the auxiliary time is small compared to the characteristic evolution time of the spectrum. This allows us to approximate the derivative by the finite difference in terms of T :

$$\frac{\partial n_{\mathbf{k}}}{\partial t} \approx \frac{n_{\mathbf{k}}(T) - n_{\mathbf{k}}(0)}{T}. \quad (2.36)$$

This step seems innocuous, but it is more than just the approximation of a derivative by the lowest order in a Taylor expansion. On the other side of the timescale separation we have $\tau_{\text{L}} \ll T$. This means that in the time increment T we have $\sim \epsilon$ linear oscillation periods, which are all smoothed over by taking the finite difference in (2.36). This derivative thereby captures the slow growth of the spectrum over a long time due to the cumulative effect of the nonlinear interactions, while filtering out the rapid oscillations that occur on the fastest timescale. From a different perspective, this filtering effect of (2.36) represents a loss of information about the fast dynamics. It is this step that makes the kinetic equation an irreversible description of the wave spectrum, much in the same way that in the kinetic theory of a self-interacting gas, we move from Hamilton's equations, which are reversible, to the coarse-grained and irreversible description provided by Boltzmann's equation.

Carrying out the finite difference in (2.36) we arrive, at last, at the kinetic equation, which we write for the general 4-wave case by restoring the interaction

coefficient $W_{3\mathbf{k}}^{12}$:

$$\dot{n}_{\mathbf{k}} = 4\pi \int |W_{3\mathbf{k}}^{12}|^2 \delta_{12}^{3\mathbf{k}} \delta(\omega_{12}^{3\mathbf{k}}) n_1 n_2 n_3 n_{\mathbf{k}} \left[\frac{1}{n_{\mathbf{k}}} + \frac{1}{n_3} - \frac{1}{n_1} - \frac{1}{n_2} \right] d\mathbf{k}_1 d\mathbf{k}_2 d\mathbf{k}_3. \quad (2.37)$$

By analogy with Boltzmann's equation, the RHS of the kinetic equation is often referred to as a collision integral.

2.3.6 Three-wave kinetic equation

The same procedure can be carried out for the 3-wave case, giving the kinetic equation

$$\dot{n}_{\mathbf{k}} = \int (\mathcal{R}_{12\mathbf{k}} - \mathcal{R}_{\mathbf{k}12} - \mathcal{R}_{2\mathbf{k}1}) d\mathbf{k}_1 d\mathbf{k}_2, \quad (2.38)$$

where

$$\mathcal{R}_{12\mathbf{k}} = 2\pi |V_{12}^{\mathbf{k}}|^2 \delta_{12}^{\mathbf{k}} \delta(\omega_{12}^{\mathbf{k}}) (n_1 n_2 - n_{\mathbf{k}} n_1 - n_2 n_{\mathbf{k}}).$$

The resonant manifold for 3-wave systems is

$$\mathbf{k} - \mathbf{k}_1 - \mathbf{k}_2 = 0, \quad \omega_{\mathbf{k}} - \omega_1 - \omega_2 = 0, \quad (2.39)$$

justifying the use of the frequency resonance when we derive $V_{12}^{\mathbf{k}}$ for the CHM equation (3.5). Also note that for the CHM equation, for which $a_{\mathbf{k}}^* = a_{-\mathbf{k}}$, we restrict the integration in (2.38) to the right half-plane.

2.4 Invariants of the kinetic equation

Having established the wave kinetic equation as our main tool of study in WT, we can now ask whether it conserves the invariants from section 2.2.

To answer this question, we consider a general integral quantity Φ with a \mathbf{k} -space density $\rho_{\mathbf{k}}$, such that

$$\Phi = \int \rho_{\mathbf{k}} n_{\mathbf{k}} d\mathbf{k}.$$

We can calculate the rate of change of Φ using the appropriate kinetic equation.

For 4-wave systems such as the GPE and SHE, we have

$$\begin{aligned} \dot{\Phi} &= \int \rho_{\mathbf{k}} \dot{n}_{\mathbf{k}} d\mathbf{k} \\ &= 4\pi \int \rho_{\mathbf{k}} |W_{3\mathbf{k}}^{12}|^2 \delta_{12}^{3\mathbf{k}} \delta(\omega_{12}^{3\mathbf{k}}) n_1 n_2 n_3 n_{\mathbf{k}} \left[\frac{1}{n_{\mathbf{k}}} + \frac{1}{n_3} - \frac{1}{n_1} - \frac{1}{n_2} \right] d\mathbf{k}_1 d\mathbf{k}_2 d\mathbf{k}_3 d\mathbf{k} \end{aligned}$$

We then break the integral into four pieces and make the following change of dummy integration variables: (identity); $(\mathbf{k} \leftrightarrow \mathbf{k}_3)$; $(\mathbf{k}, \mathbf{k}_3 \leftrightarrow \mathbf{k}_1, \mathbf{k}_2)$; $(\mathbf{k}, \mathbf{k}_3 \leftrightarrow \mathbf{k}_2, \mathbf{k}_1)$. Using

the symmetries of the interaction coefficient (2.17) we obtain

$$\begin{aligned} \dot{\Phi} = & \pi \int (\rho_{\mathbf{k}} + \rho_3 - \rho_1 - \rho_2) |W_{3\mathbf{k}}^{12}|^2 \delta_{12}^{3\mathbf{k}} \delta(\omega_{12}^{3\mathbf{k}}) \\ & \times n_1 n_2 n_3 n_{\mathbf{k}} \left[\frac{1}{n_{\mathbf{k}}} + \frac{1}{n_3} - \frac{1}{n_1} - \frac{1}{n_2} \right] d\mathbf{k}_1 d\mathbf{k}_2 d\mathbf{k}_3 d\mathbf{k}. \end{aligned}$$

Thus Φ will be conserved if its density satisfies

$$\rho_{\mathbf{k}} + \rho_3 - \rho_1 - \rho_2 = 0 \quad (2.40)$$

on the resonant manifold for 4-wave systems (2.35) on which the integrand of the kinetic equation is supported.

In a similar way, for 3-wave systems like the CHM equation, we find

$$\dot{\Phi} = \frac{1}{3} \int (\rho_{\mathbf{k}} - \rho_1 - \rho_2) \mathcal{R}_{12\mathbf{k}} d\mathbf{k}_1 d\mathbf{k}_2 d\mathbf{k}, \quad (2.41)$$

so quantities whose densities satisfy

$$\rho_{\mathbf{k}} - \rho_1 - \rho_2 = 0 \quad (2.42)$$

on the resonant manifold (2.39), are conserved in 3-wave systems.

2.4.1 Invariants of the Schrödinger-type equations

The GPE and SHE both conserve the total waveaction \mathcal{N} and the total energy \mathcal{H} . In terms of the spectrum $n_{\mathbf{k}}$ the waveaction can be written

$$\mathcal{N} = \int n_{\mathbf{k}} d\mathbf{k},$$

up to a normalising constant. The \mathbf{k} -space density of \mathcal{N} is simply 1, which trivially satisfies (2.40), and hence the waveaction is conserved by the kinetic equation (2.37).

As for the energy, we see from (2.6) that the leading-order part of the Hamiltonian (the kinetic energy) can be written in \mathbf{k} -space as

$$\mathcal{E} = \int \omega_{\mathbf{k}} n_{\mathbf{k}} d\mathbf{k}. \quad (2.43)$$

The leading-order energy \mathcal{E} has the Fourier-space density $\omega_{\mathbf{k}}$, which manifestly satisfies (2.40) on the resonant manifold (2.35). Therefore \mathcal{E} is conserved over the timescale for which the kinetic equation is valid. The conservation of \mathcal{E} , rather than the total energy \mathcal{H} , by the kinetic equation is due to the fact that the kinetic equation is derived in the weak nonlinear limit. Indeed \mathcal{E} is adiabatically conserved by the original equations of motion, whereas \mathcal{H} is exactly conserved. In subsequent

chapters we will simply call \mathcal{E} the energy of Schrödinger-type systems.

The total momentum (2.8) has density \mathbf{k} in Fourier space, which also satisfies (2.40) on the resonant manifold, showing that momentum is also conserved by (2.37).

2.4.2 Invariants of the CHM equations

Writing the energy (2.9) and enstrophy (2.10) of the CHM equation in Fourier space we obtain, up to normalising constants,

$$E = \int |\omega_{\mathbf{k}}| n_{\mathbf{k}} \, d\mathbf{k}$$

and

$$\Omega = \int k_x n_{\mathbf{k}} \, d\mathbf{k}. \quad (2.44)$$

Again, the energy density is $\omega_{\mathbf{k}}$, which satisfies (2.42) on the 3-wave resonant manifold (2.39). Therefore the energy E is an exact invariant of both the kinetic equation and the original CHM equation.

The enstrophy density is k_x , which is also the density of the x -component of momentum. It too satisfies (2.42) on the resonant manifold due to the $\delta_{12}^{\mathbf{k}}$, and so Ω is also an exact invariant of both the CHM and its kinetic equation. Note that for the CHM equation, the \mathbf{k} -space integral in (2.44) is over $k_x > 0$, and so Ω is positive-definite. The y -momentum, with density k_y , is also conserved, however it is sign-indefinite and so does not play a role in determining the direction of cascades, as we will discuss in section 3.3.2.1.

2.4.2.1 Zonostrophy: the third invariant of the CHM kinetic equation

For the generic 3-wave system, no invariants besides the energy, enstrophy, and y -momentum have been found. However, it was discovered in the 1990s [32, 34, 35, 55] that for the CHM equation and its derivatives, another quantity exists whose density

$$\varphi_{\mathbf{k}} = \arctan \frac{k_y + k_x \sqrt{3}}{\rho k^2} - \arctan \frac{k_y - k_x \sqrt{3}}{\rho k^2}$$

satisfies (2.42) on the resonant manifold. Thus the quantity

$$Z = \int \varphi_{\mathbf{k}} n_{\mathbf{k}} \, d\mathbf{k},$$

termed the zonostrophy in [36], is an invariant of the CHM kinetic equation, and an adiabatic invariant of the CHM equation itself. We will have much to say about the zonostrophy, and the role it plays in the cascades and equilibrium of CHM systems,

in chapter 3.

2.5 Stationary solutions of the kinetic equation

Having derived the kinetic equations that concern us, and enumerated their dynamical invariants, the next relevant objects of interest are their stationary solutions. There are two types of stationary solution known in WT, the equilibrium spectrum and the nonequilibrium cascade spectra.

2.5.1 The Rayleigh-Jeans equilibrium spectrum

The first type of stationary solution is the equilibrium spectrum, known as the Rayleigh-Jeans (RJ) spectrum, which has the form

$$n_{\mathbf{k}}^{\text{RJ}} = \frac{1}{\sum_j \alpha_j \rho_{\mathbf{k}}^{(j)}} \quad (2.45)$$

where the $\rho_{\mathbf{k}}^{(j)}$ are the densities of the invariants described in section 2.4, and the coefficients α_j are thermodynamic potentials conjugate to the invariants.

As the system evolves from an initial condition, the kinetic equation governs the redistribution of invariants throughout \mathbf{k} -space. Eventually the system comes to an equilibrium, at which there is equipartition across \mathbf{k} -space of the invariant whose density is the denominator of (2.45): a linear combination of the original invariants with coefficients α_j . The fact that the RJ spectrum is stationary follows by substituting (2.45) into the kinetic equation and observing that for each invariant density the combinations (2.40) or (2.42) appear as a factor in the numerator. The collision integral of the kinetic equation thus vanishes pointwise.

The RJ spectrum, the conditions for its relevance, and what it implies about the kinds of large-scale structures that are constructed by the turbulence, will be examined at length in chapters 3 and 4 so we withhold further discussion until then.

2.5.2 Kolmogorov-Zakharov flux spectra

The other family of stationary solutions of the kinetic equation are the spectra that represent the pure flux of invariants through \mathbf{k} -space in a local, scale-by-scale cascade. These are the Kolmogorov-Zakharov (KZ) spectra. Since their discovery in 1965 by Zakharov [7] the KZ spectra have played a central role in the theory of WT.

Despite this, the KZ spectra do not turn out to be relevant in most of what we will discuss in this thesis. As such, we will not give a detailed derivation of the KZ spectra here, but make only some brief comments.

2.5.2.1 KZ spectra for isotropic systems

The theory of KZ spectra was developed in the context of isotropic systems, for which both the dispersion relation $\omega_{\mathbf{k}}$ and the wave interaction coefficient, e.g. $W_{12}^{3\mathbf{k}}$, depend only on the magnitude $k = |\mathbf{k}|$ of the wavenumber. Further it is assumed that the dispersion relation and the interaction coefficient are both scale invariant, i.e. homogeneous functions of their arguments, so that rescaling the wavenumber $k \rightarrow \mu k$ gives $\omega_{\mu\mathbf{k}} = \mu^\alpha \omega_{\mathbf{k}}$ and $W_{\mu\mathbf{k}_1\mu\mathbf{k}_2}^{\mu\mathbf{k}_3\mu\mathbf{k}_4} = \mu^\beta W_{\mathbf{k}_1\mathbf{k}_2}^{\mathbf{k}_3\mathbf{k}_4}$. One then seeks stationary KZ spectra that are scale invariant,

$$n_{\mathbf{k}}^{\text{KZ}} \propto k^\nu.$$

Under these conditions the angles in the collision integral can be integrated out to obtain an integral over the modulus k 's only. A set of coordinate transformations, discovered independently by Zakharov [56] and Kraichnan [57], transform the collision integral into a form where the spectral indices ν for stationary KZ spectra can be read off by considering a factor that vanishes on the resonant manifold, much like in section 2.4 above. The various possible values for ν correspond, formally at least, to the spectra that might possibly realise the cascade of invariants through scales.

The full derivation of the KZ spectra for isotropic systems can be found in e.g. [3, 4, 19]. The GPE and SHE are equations for which the formal KZ spectra can be found in this way. However, as we will discover in chapter 4, only in the 3D GPE does the KZ spectra turn out to be physically relevant. In the 2D GPE, and for the SHE in both 3D and 2D, the KZ spectra are not the spectra that realise the flux of invariants, because they predict cascades of invariants in the wrong direction with respect to the more robust Fjørtoft argument, see section 2.6 below.

2.5.2.2 Anisotropic systems, and lack of KZ spectra in the CHM equation

The procedure sketched above can be modified to incorporate anisotropic systems, as was first done by Kuznetsov [58]. The system is assumed to be scale-invariant with separate degrees of homogeneity in the x and y directions, so under $\mathbf{k} = (k_x, k_y) \rightarrow (\mu_x k_x, \mu_y k_y)$ the dispersion relation scales as

$$\omega_{(\mu_x k_x, \mu_y k_y)} = \mu_x^{\alpha_x} \mu_y^{\alpha_y} \omega_{(k_x, k_y)},$$

and the interaction coefficient as

$$V_{(\mu_x k_{1x}, \mu_y k_{1y}), (\mu_x k_{2x}, \mu_y k_{2y})}^{(\mu_x k_x, \mu_y k_y)} = \mu_x^{\beta_x} \mu_y^{\beta_y} V_{(k_{1x}, k_{1y}), (k_{2x}, k_{2y})}^{(k_x, k_y)}.$$

Anisotropic scale-invariant KZ spectra

$$n_{\mathbf{k}}^{\text{KZ}} \propto |k_x|^{\nu_x} |k_y|^{\nu_y}$$

can then be sought via a generalised Zakharov-Kraichnan transform.

The KZ spectra for certain limits of the CHM equation have been found, which formally predict the cascade of E and Ω [59–61], and Z [32, 34]. However these KZ spectra suffer from several problems.

Firstly, for a candidate KZ spectrum to be physically relevant, it must have the property of stationary locality: on the candidate spectrum, at a scale deep in the inertial range, the flux of invariants must be dominated by interactions at comparable scales. If instead the interactions are primarily with scales at the ends of the inertial range (i.e. the forcing or dissipation scales), then the spectrum is said to be nonlocal. Nonlocal spectra are not universal as they depend on the details of the forcing and dissipation.

Secondly, the candidate KZ spectrum must have evolutionary locality: perturbations to the spectrum around a certain scale deep in the inertial range must evolve in time via interactions with comparable scales. Again, if the perturbations evolve via interactions with the forcing or dissipation scales then the spectrum is evolutionary nonlocal, and not universal.

Thirdly, even if the candidate KZ spectrum has stationary and evolutionary locality, it must be stable to perturbations to be physically realisable.

The locality and stability of the formal KZ spectra found for the CHM cascade spectra were investigated in [55, 62]. None of the candidate spectra possesses the necessary locality and stability properties, therefore the KZ spectra are not relevant to the CHM equation. Instead CHM turbulence has the property of being strongly nonlocal: turbulence at some intermediate scale interacts directly with large-scale structures at the so-called zonal scales $|k_x| \ll |k_y|$, see [39] for a review. We will discuss these zonal structures more in chapter 3, and present an argument for their formation in terms of the equilibrium RJ spectrum (2.45).

2.6 The dual cascade in the GPE: the Fjørtoft argument

The final theoretical aspect we wish to review is a crucial result on which the investigations in chapters 3 and 4 are based. This is the Fjørtoft argument for the directions in which invariants will flow in \mathbf{k} -space, by whatever cascade process, be it local or nonlocal, isotropic or anisotropic, stationary or time-dependent. The flow of invariants to large scales is what is responsible for the creation of large-scale structure in WT, and the direction of this flow is determined by the Fjørtoft argument.

The argument applies when there are two or more invariants of some evolution equation that have \mathbf{k} -space densities that are positive-definite, and differ by monotonic functions of k_x and k_y . The three-invariant case of the CHM kinetic equation was studied in [36]. Here we present the two-invariant case of the GPE kinetic equation, whose invariants are the energy \mathcal{E} and waveaction \mathcal{N} , for which the ratio of invariant densities is $\omega_{\mathbf{k}} = k^2$. The argument is identical to the case of the 2D Euler equation whose invariants are enstrophy Ω and energy E , see table 3.1.

The Fjørtoft argument has several different formulations [3, 63, 64]. Here we will present the version of the argument found in [3], which is most applicable to the situation where the turbulence evolves from an initial condition. In section 4.3.3 we give the argument for a forced-dissipated system where the invariants are carried from where they are injected by forcing to where they are removed by dissipation, on stationary spectra.

First we recall the definition of the waveaction and energy. Respectively,

$$\mathcal{N} = \int n_{\mathbf{k}} \, d\mathbf{k}, \quad \mathcal{E} = \int \omega_{\mathbf{k}} n_{\mathbf{k}} \, d\mathbf{k}. \quad (2.46a)$$

Dimensionally we can form the (absolute value of the) wavenumber $k_0 = \sqrt{\mathcal{E}/\mathcal{N}}$ that characterises the inverse lengthscale of the initial spectrum. Now we define the \mathcal{N} -centroid and the \mathcal{E} -centroid, respectively

$$k_{\mathcal{N}} = \int k n_{\mathbf{k}} \, d\mathbf{k}, \quad k_{\mathcal{E}} = \int k \omega_{\mathbf{k}} n_{\mathbf{k}} \, d\mathbf{k} \quad (2.46b)$$

(we assume convergence of the above integrals). These centroids are (absolute) wavenumbers that characterise the distributions of \mathcal{N} and \mathcal{E} in k -space (i.e. integrating over angles in \mathbf{k} -space and considering the invariant densities projected onto the $k \in [0, \infty)$ half-line).

We now make use of the Cauchy-Schwartz inequality which states that for any functions $f(k)$ and $g(k)$,

$$\left| \int f(k)g(k) \, dk \right| \leq \left| \int f(k)^2 \, dk \right|^{1/2} \left| \int g(k)^2 \, dk \right|^{1/2}. \quad (2.46c)$$

Applying the inequality to \mathcal{E} we have

$$\begin{aligned} \mathcal{E} &= \int k^2 n_{\mathbf{k}} \, d\mathbf{k} = \int \left(k^{1/2} n_{\mathbf{k}}^{1/2} \right) \left(k^{3/2} n_{\mathbf{k}}^{1/2} \right) \, d\mathbf{k} \\ &\leq \left(\int k n_{\mathbf{k}} \, d\mathbf{k} \right)^{1/2} \left(\int k^3 n_{\mathbf{k}} \, d\mathbf{k} \right)^{1/2} = \sqrt{\mathcal{N} k_{\mathcal{N}}} \sqrt{\mathcal{E} k_{\mathcal{E}}} \\ &\Rightarrow k_{\mathcal{N}} k_{\mathcal{E}} \geq \frac{\mathcal{E}}{\mathcal{N}} = k_0^2. \end{aligned} \quad (2.46d)$$

This implies that if the spectrum changes during the evolution such that the \mathcal{N} and \mathcal{E} -centroids move apart in k -space, it must do so in such a way that the centroids move in opposite directions. In particular if the \mathcal{N} -centroid moves to low wavenumber then the \mathcal{E} -centroid must move to high wavenumber.

To show that the centroids do indeed move in these directions, consider

$$\begin{aligned} \mathcal{N}k_{\mathcal{N}} &= \int kn_{\mathbf{k}} \, d\mathbf{k} = \int \left(kn_{\mathbf{k}}^{1/2}\right) \left(n_{\mathbf{k}}^{1/2}\right) \, d\mathbf{k} \\ &\leq \left(\int k^2 n_{\mathbf{k}} \, d\mathbf{k}\right)^{1/2} \left(\int n_{\mathbf{k}} \, d\mathbf{k}\right)^{1/2} = \sqrt{\mathcal{E}\mathcal{N}} \\ &\Rightarrow k_{\mathcal{N}} \leq \sqrt{\frac{\mathcal{E}}{\mathcal{N}}} = k_0, \end{aligned} \tag{2.46e}$$

so if the \mathcal{N} -centroid moves, it must move to low wavenumber.

Combining (2.46d) and (2.46e) together, we also find $k_{\mathcal{E}} \geq k_0$, so the \mathcal{E} -centroid moves to high wavenumber if it moves at all.

Thus we conclude that if the spectrum changes from its initial state, it must do so in such a way that the characteristic lengthscale of \mathcal{N} moves to large scale and that of \mathcal{E} moves to small scale. This is nothing less than a prediction of the dual cascade of waveaction and energy, with an inverse cascade of waveaction. This inverse cascade is then responsible for the construction of large-scale structure.

The outcome of the Fjørtoft argument that the dual cascade sends each positive-definite invariant to the region of k -space where its density dominates over the other invariant. This is also the case when there are three invariants present: each centroid moves towards the part of \mathbf{k} -space where its density is dominant [36].

The argument is very robust, and in this presentation it is conditioned only on the invariants and centroids being integrable. The predictions of the Fjørtoft argument is therefore the primary consideration when considering the cascades of invariants, and any finding that appears to contradict these predictions has either very special conditions attached to it, or is false.

Chapter 3

Equilibria and condensates in Rossby and drift wave turbulence

3.1 Chapter summary

In this chapter we study the thermodynamic equilibrium spectra of the Charney-Hasegawa-Mima (CHM) equation in its weakly nonlinear limit. In this limit, the equation has three adiabatic invariants, in contrast to the two invariants of the 2D Euler or Gross-Pitaevskii equations, which are examples for comparison. We explore how the third invariant considerably enriches the variety of equilibrium spectra that the CHM system can access. In particular we characterise the singular limits of these spectra in which condensates occur, i.e. a single Fourier mode (or pair of modes) accumulate(s) a macroscopic fraction of the total invariants. We show that these equilibrium condensates provide a simple explanation for the characteristic structures observed in CHM systems of finite size: highly anisotropic zonal flows, large-scale isotropic vortices, and vortices at small scale. We show how these condensates are associated with combinations of negative thermodynamic potentials (e.g. temperature).

3.2 Introduction

It is well known that the turbulent flow of statistically isotropic ideal fluids in two dimensions (2D) conserves not only the total kinetic energy E but also the total mean square vorticity, or enstrophy Ω . The presence of these two invariants of motion places strong restrictions on how the flow may evolve, namely that any change must involve E moving into large-scale motion of the flow while Ω concentrates in

small-scale motions. Perhaps the most famous result in this direction is Kraichnan’s dual cascade of 2D turbulence [57]. However one of the earliest formulations is the simple and robust argument of Fjørtoft [63], whose conclusion can be expressed as a principle involving the sign-definite global invariants of the flow: each such invariant is pushed by all the others towards the sector of Fourier space where its spectral weight is greatest [36, 3].

This statement, regarding the dynamics of 2D flow, is also reflected in the equilibrium statistical mechanics of 2D turbulence. Onsager [65] studied point vortices in a spatially finite domain, and found that flow states with high energy involve like-signed vortices clustering together to form large-scale supervortices, and that these configurations are associated with a negative thermodynamic temperature. Later, Kraichnan [57, 66] considered continuous vorticity fields by examining the 2D Euler equation with Fourier truncations at the small and large scale. He established that their statistical equilibria also predicted the large-scale (respectively small-scale) accumulation of energy (enstrophy), with the equilibrium being parameterised by a negative temperature (enstrophy temperature), see also review [67]. Kraichnan also noted the analogy between the accumulation of energy into the largest scale in 2D turbulence, and the condensation of particles in a 2D Bose gas [57], directly terming the former as condensation of energy into the “gravest mode” [66].

In planetary atmospheres and oceans, and in magnetically confined fusion plasmas, the slow mesoscale dynamics comprises of a quasi-2D flow constrained by the gradient of the Coriolis force in the geophysical case, and the diamagnetic drift in the plasma case. This gradient constraint, called the β effect in the geophysical literature, breaks the isotropy of the system. Consequently in these systems it is observed that energy condenses not into the gravest isotropic mode, but rather into strongly anisotropic zonal flows: bands of alternating shear flows aligned latitudinally (geophysical), or in the poloidal direction of the confinement device (plasma), and block the transport of energy and fluid across them [68, 69, 33, 70, 71, 47, 72, 37, 48].

In figure 3.1 we show illustrative examples of quasi-2D fluid systems with a β effect that exhibit zonal flows. The geophysical case is represented in (a) by an observation the planet Jupiter with its characteristic zonal bands. In (b) we show a plasma case: numerical simulations of the core of a magnetically-confined fusion plasma in a tokamak. Note that these zonal flows have wave-like undulations, and co-exist with isotropic vortices (for example, the famous Great Red Spot of Jupiter). A description of the zonal flows and vortices present in such systems, in terms of the thermodynamics of the weakly nonlinear waves, is the goal of the present chapter.

An important feature of such quasi-2D flows with a β effect is that in addition to E and Ω , for systems with small nonlinearity there exists a third positive-definite

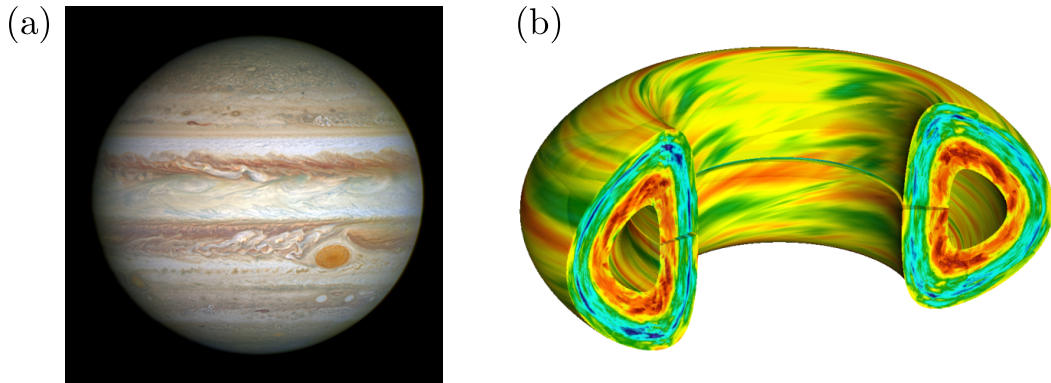


Figure 3.1: Waves, zonal flows, and vortices in quasi-2D flows with a β effect. (a) Geophysical case: observations of the atmosphere of Jupiter [73]. (b) Plasma case: simulation of a tokamak plasma [74].

adiabatic invariant of motion [32, 35, 34]. This invariant explains the tendency for energy to condense into zonal jets by the following adaptation of the Fjørtoft argument. The three invariants divide Fourier space into three sectors in an anisotropic way, shown in figure 3.5 below. Each sector is dominated by the cascade of its respective invariant, with the gravest isotropic mode being occupied by the cascade of the third invariant. This “throws” the energy cascade onto zonal modes, with wavenumber components $k_x \ll k_y$; hence the third invariant has been termed zonostrophy [36].

Such considerations are relevant in a non-equilibrium situation, either when the system is transiently evolving from an initial condition, or when there is persistent forcing and dissipation. In the present chapter we offer an alternative explanation of the tendency for zonal modes to condense energy, based on the statistical equilibria of quasi-2D flows with a β effect in the weakly nonlinear limit, and show that these too predict the condensation of energy into zonal flows. We study the Charney-Hasegawa-Mima (CHM) equation [75, 76], which is a simple model that describes free-energy-driven turbulence and zonal flow formation in both quasi-geostrophic geophysical flows, and drift dynamics in magnetically confined plasmas [69]. We examine the CHM equation in the weakly nonlinear limit, using the theory of wave turbulence (WT) [4, 3] to find the equilibrium spectra of flows where enstrophy, energy, and zonostrophy are all invariants of the motion.

Our approach is similar in spirit to Einstein’s original analysis of Bose-Einstein condensation [77], Kraichnan’s analysis of the 2D Euler equation [57, 66, 67], and to the description by Connaughton et. al. [20] of the condensation of classical waves obeying the Gross-Pitaevskii equation (GPE, also known as the nonlinear Schrödinger equation), using WT theory. In this spirit, we identify and characterise the types of equilibrium states that weakly nonlinear CHM systems can access. This

provides a qualitative but informative understanding: that WT processes, such as the triple cascade, are manifested as the system seeks out these equilibria that are the end point of the turbulence.

It is worthwhile at this point to summarise the findings of [20] on the GPE in order to preview the WT approach we take here, and to specify concretely what the term “condensation” will refer to in this chapter. In the appendix to this chapter we recapitulate results on infinite-sized GPE systems in 3D and 2D in slightly more detail, as well as apply the results of this chapter to the 2D GPE in finite-sized systems.

3.2.1 Condensation outside and within the equilibrium spectrum

The GPE (3.23) in the WT limit has two invariants: the total waveaction, or number of particles \mathcal{N} , and the leading order energy \mathcal{E} . Once initialised with this \mathcal{N} and \mathcal{E} , the system will come to equilibrium on the so-called Rayleigh-Jeans (RJ) spectrum $n_{\mathbf{k}}^{\text{RJ}}$ (3.25). Crucially, in three dimensions (3D) the integrals that define \mathcal{N} and \mathcal{E} on the RJ spectrum converge as the system size tends to infinity, meaning that $n_{\mathbf{k}}^{\text{RJ}}$ can only accommodate a finite amount of particles and energy. There exists some nonzero ratio of energy per particle, i.e. temperature, below which the excess particles must collapse into a singular distribution at wavenumber $\mathbf{k} = 0$; this distribution can absorb an arbitrarily large fraction of the total number of particles in the system. This is the WT counterpart of Einstein’s argument for condensation of a Bose gas [77]. Strictly speaking it is this singular distribution that is known as the true Bose-Einstein condensate [78].

By contrast in 2D, \mathcal{N} diverges logarithmically at low wavenumber and so the RJ spectrum can absorb an arbitrary number of particles in the infinite box limit. Consequently no nonzero critical condensation temperature exists for a spatially infinite system, a manifestation of the Mermin-Wagner-Hohenberg theorem [79, 80]. However for spatially finite 2D systems condensation is restored, in the sense of the largest-scale (“gravest”) mode containing a macroscopic fraction of the total \mathcal{N} [81–85]. Numerical demonstrations of finite-size condensation can also clearly be seen in [10, 11]. It is in this sense that we refer to “condensation” in this chapter: a macroscopic fraction of the invariants occupying a single fundamental mode *within the equilibrium RJ spectrum*. As we will see, the meaning of the fundamental mode changes in the 2D anisotropic system we examine here.

Finally, we note that in studying the GPE, we can take the ratio \mathcal{E}/\mathcal{N} as the control parameter, as this ratio is accessible by specifying the initial spectrum. One can then take the chemical potential μ as the sole thermodynamic potential that characterises the equilibrium. The phase diagram for the GPE is thus one dimensional. In the CHM system we examine, the presence of an additional in-

variant requires a third thermodynamic potential to describe the equilibrium, and two ratios of invariants are needed as control variables. Thus the phase diagram for weakly nonlinear CHM turbulence requires two dimensions to visualise, and is much more intricate than the generic one dimensional phase diagram. We will see that it contains seven of the eight possible sign combinations for the three thermodynamic potentials, and that condensates are associated with the margins of the phase diagram, where at least one potential is negative.

3.2.2 Organisation of this chapter

We start in section 3.3 by recapitulating the WT of the CHM equation, defining its absolute and adiabatic invariants, and stating its RJ spectrum. We also make clear the correspondence between the CHM, the 2D GPE, and 2D Euler flow. Then in section 3.4 we consider the range of values that the thermodynamic potentials can take for a physical RJ spectrum, and enumerate the possible Fourier modes over which the RJ spectrum is singular, i.e. the fundamental modes where we expect condensates to form. In section 3.5 we demonstrate that condensates, in the sense we have described above, do indeed form at the specified fundamental modes, and that these condensates do not survive in the infinite box limit, as expected from the Mermin-Wagner-Hohenberg theorem. In section 3.6 we plot the phase diagram for weak CHM turbulence. We conclude in section 3.7.

3.3 Charney-Hasegawa-Mima equation

The CHM equation,

$$\frac{\partial}{\partial t} (\nabla^2 \psi - \rho^{-2} \psi) + \beta \frac{\partial \psi}{\partial x} + \left[\frac{\partial \psi}{\partial x} \frac{\partial \nabla^2 \psi}{\partial y} - \frac{\partial \psi}{\partial y} \frac{\partial \nabla^2 \psi}{\partial x} \right] = 0, \quad (3.1)$$

describes the evolution of the stream function $\psi(\mathbf{x}, t)$ in 2 spatial dimensions (in the plasma context ψ also represents the electrostatic potential). Equation (3.1) appears with dimensions, and ρ is the Rossby deformation radius (geophysics) or the ion gyroradius at the electron temperature (plasma).

In (3.1) we have adopted geophysical notation, in which x is the zonal direction (west-east) and y is the latitudinal (south-north) direction. In this convention when (3.1) is interpreted in the plasma context y is the direction of decreasing density and x is the direction binormal to the magnetic field and the density gradient. β measures the gradient of Coriolis parameter or plasma density gradient, which provides a restoring force to perturbations, allowing linear wave solutions of (3.1) in the absence of nonlinearity (terms in square brackets in (3.1) vanish). These are known as Rossby waves in geophysics and drift waves in the plasma context, and

have dispersion relation

$$\omega_{\mathbf{k}} = -\beta\rho^2 \frac{k_x}{1 + \rho^2 k^2}, \quad (3.2)$$

where $\mathbf{k} = (k_x, k_y)$ is the wavenumber and $k = |\mathbf{k}|$. The WT we discuss in this chapter is the turbulence of Rossby/drift waves, which comes about when the system is weakly nonlinear.

3.3.1 Wave turbulence and the CHM kinetic equation

We now describe the CHM equation in its WT limit. We consider the system inside \mathbb{T}_L^2 , a 2D periodic box of side length L , and decompose into Fourier modes $\psi_{\mathbf{k}}(t) = \int_{\mathbb{T}_L^2} \psi(\mathbf{x}, t) \exp(-i\mathbf{k} \cdot \mathbf{x}) d\mathbf{x}$. We then assume the modes are statistically independent in phase and amplitude, that the phases are uniformly distributed in $[0, 2\pi)$, and we formally take the limits of an infinite box ($L \rightarrow \infty$), and weak nonlinearity. One can then derive a three-wave kinetic equation for the evolution of the waveaction spectrum [31]

$$n_{\mathbf{k}} = \left(\frac{L}{2\pi}\right)^2 \frac{(1 + \rho^2 k^2)^2}{\beta\rho^4 |k_x|} \langle |\psi_{\mathbf{k}}|^2 \rangle \quad (3.3)$$

where the angle brackets denote averaging over phases and amplitudes of the initial wave modes. The kinetic equation is

$$\frac{\partial n_{\mathbf{k}}}{\partial t} = \int_{k_{1x}, k_{2x} > 0} (\mathcal{R}_{12\mathbf{k}} - \mathcal{R}_{\mathbf{k}12} - \mathcal{R}_{2\mathbf{k}1}) d\mathbf{k}_1 d\mathbf{k}_2, \quad (3.4)$$

where

$$\mathcal{R}_{12\mathbf{k}} = 2\pi |V_{12}^{\mathbf{k}}|^2 \delta_{12}^{\mathbf{k}} \delta(\omega_{12}^{\mathbf{k}}) (n_1 n_2 - n_{\mathbf{k}} n_1 - n_2 n_{\mathbf{k}}),$$

with interacting triads of waves lying on a resonant manifold, enforced by the Dirac delta functions for wavenumbers and frequencies, $\delta_{12}^{\mathbf{k}} = \delta(\mathbf{k} - \mathbf{k}_1 - \mathbf{k}_2)$ and $\delta(\omega_{12}^{\mathbf{k}}) = \delta(\omega_{\mathbf{k}} - \omega_1 - \omega_2)$ respectively. The strength of near-resonant interactions is given by the three-wave interaction coefficient

$$V_{12}^{\mathbf{k}} = i \frac{\sqrt{\beta k_x k_{1x} k_{2x}}}{2} \left(\frac{k_y}{1 + \rho^2 k^2} - \frac{k_{1y}}{1 + \rho^2 k_1^2} - \frac{k_{2y}}{1 + \rho^2 k_2^2} \right). \quad (3.5)$$

In the above we have used the shorthand $n_j = n_{\mathbf{k}_j}$ etc, and likewise for ω_j .

In (3.4) the integral is taken over half of \mathbf{k} -space due to $\psi(\mathbf{x}, t)$ being a real field, and hence $\psi_{\mathbf{k}}^* = \psi_{-\mathbf{k}}$. The zonal axis $k_x = 0$ is excluded because by (3.5) these modes do not take part in wave interactions, so modes that are exactly on the zonal axis do not evolve with the rest of the wave spectrum and are not described by (3.4).

Details of the derivation of (3.4), as well as many of the results obtained by the WT theory for the CHM equation, can be found in review [39].

3.3.2 Invariants of the kinetic equation, and the Rayleigh-Jeans spectrum

The three-wave kinetic equation (3.4) describes the irreversible evolution of an initial spectrum of waves towards states that make the spectrum stationary ($\partial_t n_{\mathbf{k}} = 0$). This kinetic equation has an H-theorem for the growth of nonequilibrium entropy, ensuring ergodic exploration of the phase space [86]. As this evolution progresses the dynamical invariants of the equation remain constant, but are redistributed throughout \mathbf{k} -space. We turn our attention to these invariants next.

3.3.2.1 Invariants of the kinetic equation

As in the 2D Euler equation there are two macroscopic invariants—the total enstrophy and energy—that are conserved by the CHM equation (3.1). These two invariants are also exactly conserved by the kinetic equation (3.4), and are calculated by integrating the enstrophy and energy spectra $\Omega_{\mathbf{k}}$ and $E_{\mathbf{k}}$ respectively, over Fourier space:

$$\Omega = \int_{k_x > 0} \Omega_{\mathbf{k}} d\mathbf{k} \quad \text{with} \quad \Omega_{\mathbf{k}} = k_x n_{\mathbf{k}}, \quad (3.6)$$

and

$$E = \int_{k_x > 0} E_{\mathbf{k}} d\mathbf{k} \quad \text{with} \quad E_{\mathbf{k}} = |\omega_{\mathbf{k}}| n_{\mathbf{k}}, \quad (3.7)$$

i.e. k_x and $|\omega_{\mathbf{k}}|$ are respectively the enstrophy and energy densities.

In addition to these there is a third independent macroscopic quantity that is conserved by the kinetic equation: the zonostrophy [32, 55, 35, 34]

$$Z = \int_{k_x > 0} Z_{\mathbf{k}} d\mathbf{k} \quad \text{with} \quad Z_{\mathbf{k}} = \varphi_{\mathbf{k}} n_{\mathbf{k}}, \quad (3.8)$$

where the general expression for $\varphi_{\mathbf{k}}$ is given in [34]. Formally Z is only adiabatically conserved by the original CHM equation (3.1). However in simulations it is remarkably well conserved for long times even for strong nonlinearities, see [36].

To eliminate β we make the transformation $(\psi, t) \rightarrow (\beta\psi, t/\beta)$ in (3.1), making it dimensionless. Further, we work in the small-scale limit $\rho k \gg 1$, in which case

the energy and zonostrophy densities become [55]

$$|\omega_{\mathbf{k}}| = \frac{k_x}{k^2} \quad \text{and} \quad \varphi_{\mathbf{k}} = \frac{k_x^3(k_x^2 + 5k_y^2)}{k^{10}}. \quad (3.9)$$

Importantly, as $k_x > 0$, all three invariants of the kinetic equation (Ω, E, Z) are positive-definite. Consequently the Fjørtoft principle described in section 3.2 applies: each invariant places a constraint on where the other two invariants move in \mathbf{k} -space during the evolution of the kinetic equation, leading to the dynamical formation of zonal flows [36]. As well as the enstrophy, Ω also corresponds to the total momentum of the system in the x direction. The y -momentum $\int_{k_x > 0} k_y n_{\mathbf{k}} d\mathbf{k}$ is also conserved, but it can be positive or negative, and so places no constraint on the flow of the other invariants through \mathbf{k} -space. We consider the simplest case, of systems with zero y -momentum, i.e. spectra that are even in k_y , a property that is conserved by the kinetic equation. We also exclude the meridional axis $k_y = 0$ to retain symmetry with the zonal axis and to make the gravest mode in our system the largest-scale isotropic mode, c.f. [66]. Formally we could retain the meridional axis in what follows, but the gravest mode would then be anisotropic, which would be unrealistic.

With these assumptions, we can restrict \mathbf{k} -space to the first quadrant ($k_x, k_y > 0$), and (3.6)-(3.8) will yield (Ω, E, Z) up to a factor of two that can be absorbed into the definition $n_{\mathbf{k}}$.

3.3.2.2 Rayleigh-Jeans equilibrium spectrum

The amounts of the dynamical invariants that a system of waves possesses are set by the initial spectrum according to (3.6)-(3.8). The spectrum then evolves according to the kinetic equation (3.4), which redistributes the invariants across \mathbf{k} -space, until thermodynamic equilibrium is reached. Formally the equilibrium solution of (3.4) is the RJ spectrum

$$n_{\mathbf{k}}^{\text{RJ}} = \frac{T}{\mu|\omega_{\mathbf{k}}| + k_x + \lambda\varphi_{\mathbf{k}}}, \quad (3.10)$$

on which the quantity $\sigma = (\mu E + \Omega + \lambda Z)/T$, i.e. a linear combination of the three invariants of the kinetic equation, is partitioned equally across the available degrees of freedom (Fourier modes). This can be seen by noting that on the RJ spectrum the density of σ , i.e. $\sigma_{\mathbf{k}}$, is independent of \mathbf{k} . However, if this is the case in an unbounded \mathbf{k} -space then the integral of $\sigma_{\mathbf{k}}$ against spectrum (3.10) diverges, which is unphysical. This is the WT version of the ultraviolet catastrophe. To restore nontrivial equilibria we introduce a high wavenumber cutoff k_{max} , corresponding to a minimum allowed lengthscale in the system. In a real fluid or plasma this could represent the effects of small-scale physics; in simulations this is the spatial

Table 3.1: Equivalence between equilibrium spectra and invariants of the CHM equation, GPE, and 2D Euler equation.

CHM ($\lambda = 0$)	2D Euler	GPE	Functional form
$E_{\mathbf{k}}^{\text{RJ}}$	$E_{\mathbf{k}}^{\text{RJ}}$	$n_{\mathbf{k}}^{\text{RJ}}$	$\frac{T}{k^2 + \mu}$
E	E	\mathcal{N}	$\int \frac{T}{k^2 + \mu} d\mathbf{k}$
Ω	Ω	\mathcal{E}	$\int \frac{Tk^2}{k^2 + \mu} d\mathbf{k}$

discretisation [20].

In the RJ spectrum (3.10) we refer to T as the “temperature”, μ as the “chemical potential” and λ as the “zonostrophy potential”. This differs from the usual WT convention in which $1/T$ is conjugate to the energy density $|\omega_{\mathbf{k}}|$. In (3.10) we have instead selected $1/T$ to be conjugate to the enstrophy density k_x to make contact with both the large-scale condensation of energy in the 2D Euler equation, and particles in the 2D GPE. The equilibrium energy spectrum for the 2D Euler equation has the same functional form as the waveaction spectrum for the 2D GPE [66, 67]. These coincide with the CHM energy spectrum $E_{\mathbf{k}}^{\text{RJ}} = |\omega_{\mathbf{k}}|n_{\mathbf{k}}^{\text{RJ}}$ when we set $\lambda = 0$. Likewise the CHM energy and enstrophy invariants with $\lambda = 0$ have the same functional form as those of the 2D Euler equation, and the total waveaction and energy in the 2D GPE, see table 3.1. Thus when we set $\lambda = 0$, the potentials μ and T in (3.10) directly map on to the chemical potential and temperature of an analogous GPE system.

At this point we re-introduce the finite box size L , in order to study the behaviour of the RJ spectrum and invariants as $L \rightarrow \infty$. This involves rewriting the integrals in (3.4)-(3.8) as discrete sums over a lattice of modes in Fourier space, with mode spacing $\Delta k = 2\pi/L$, from $k_{\min} = \Delta k$ to k_{\max} in each direction. We refer to this as the “discrete sum” approach. (This is distinct from “discrete wave turbulence” where no kinetic equation can be derived; see [38] for a discussion of the latter in the CHM equation.) We note, however, that the derivation of the kinetic equation (3.4) relies on taking the $L \rightarrow \infty$ limit. Here we assume without proof that the conservation of (Ω, E, Z) remains approximately valid for a large but finite system containing many Fourier modes, although for illustration purposes our figures will be plotted with only a few modes for clarity.

Finally, we can eliminate one free parameter by rescaling variables in terms of k_{\max} :

$$\epsilon = \frac{k_{\min}}{k_{\max}}, \quad \tilde{\mathbf{k}} = \frac{\mathbf{k}}{k_{\max}}, \quad \tilde{\mu} = \frac{\mu}{k_{\max}^2}, \quad \tilde{\lambda} = \frac{\lambda}{k_{\max}^6}, \quad \tilde{\Omega} = \frac{\Omega}{k_{\max}^2}, \quad \tilde{Z} = k_{\max}^4 Z, \quad (3.11)$$

(E is unchanged by this rescaling). Dropping the tildes immediately, the quantity of the three invariants that can be fit by a Rayleigh-Jeans equilibrium spectrum are

given by

$$\Omega = T\epsilon^2 \sum_{L_\epsilon} \frac{k^{10}}{D(\mathbf{k}, \mu, \lambda)}, \quad E = T\epsilon^2 \sum_{L_\epsilon} \frac{k^8}{D(\mathbf{k}, \mu, \lambda)}, \quad Z = T\epsilon^2 \sum_{L_\epsilon} \frac{k_x^2(k_x^2 + 5k_y^2)}{D(\mathbf{k}, \mu, \lambda)}, \quad (3.12)$$

when we are using discrete sums. All three summands have denominator

$$D(\mathbf{k}, \mu, \lambda) = \mu k^8 + k^{10} + \lambda k_x^2(k_x^2 + 5k_y^2),$$

and the sums are over the \mathbf{k} -space lattice $L_\epsilon = \{(k_x, k_y) = (\epsilon i, \epsilon j) : i, j = 1, \dots, \epsilon^{-1}\}$.

We use discrete sums in order to consistently study the infinite box limit $\epsilon \rightarrow 0$ in which both the mode spacing and the lower limits of the integrals in (3.6)-(3.8) vanish together. If instead we send the mode spacing to zero while retaining a finite lower limit on the integrals then the integration would be over the square $S_\epsilon = [\epsilon, 1]^2$. We will refer to this in passing as the ‘‘continuous integral’’ approach, in contrast to the discrete sum approach.

3.4 Regularity and divergence of the RJ spectrum

Having established the form of the RJ spectrum, we can now explore the parameter range for which it is valid. The waveaction spectrum (3.3) is manifestly positive-definite in $k_x > 0$, and so we require $\text{sgn } T = \text{sgn } D(\mathbf{k}, \mu, \lambda)$. Therefore physically meaningful equilibria exist with positive and negative temperature, as long as the spectrum, and hence the invariants (3.12), are positive. On the other hand, the spectrum diverges, and the RJ solution is no longer physical, when

$$D(\mathbf{k}, \mu, \lambda) = 0. \quad (3.13)$$

In this section we establish the conditions for (3.13) to be true and hence map out the edge of parameter space corresponding to allowable RJ spectra. The set corresponding to (3.13) is some 3D hypersurface in the space of (k_x, k_y, μ, λ) . We can collapse this to a 2D plot by expressing one of these variables as a function of one other, treating the other two as parameters. In section 3.4.1 we (arbitrarily) choose λ as the independent variable and plot $\mu(\lambda)$, treating k_x and k_y as parameters. Then in section 3.4.2 we plot the k_x - k_y plane, with parameters λ and $\mu(\lambda)$ set to their values that first make the RJ spectrum singular.

the grey RJ-forbidden region are the piecewise linear functions¹

$$\mu^+(\lambda) = \max_{\mathbf{k} \in L_\epsilon} \mu(\mathbf{k}, \lambda) \quad \text{and} \quad \mu_-(\lambda) = \min_{\mathbf{k} \in L_\epsilon} \mu(\mathbf{k}, \lambda), \quad (3.15)$$

respectively (in the continuous integral approach the max and min are taken over $\mathbf{k} \in S_\epsilon$ and the brown portion of $\mu^+(\lambda)$ is a differentiable function, see section 3.4.2). Both the $\mu^+(\lambda)$ and $\mu_-(\lambda)$ RJ boundaries divide into three segments. In each segment a different mode $\mathbf{k}^+(\lambda)$ or $\mathbf{k}_-(\lambda)$ parameterises that part of the boundary, i.e.

$$\mathbf{k}^+(\lambda) = \arg \max_{\mathbf{k} \in L_\epsilon} \mu(\mathbf{k}, \lambda) \quad \text{or} \quad \mathbf{k}_-(\lambda) = \arg \min_{\mathbf{k} \in L_\epsilon} \mu(\mathbf{k}, \lambda) \quad (3.16)$$

(or arg max and arg min over $\mathbf{k} \in S_\epsilon$ for continuous integrals). In figure 3.2 the different segments of μ^\pm are coloured according to the \mathbf{k}^\pm that parameterises them; we retain the colour scheme throughout this chapter to refer to the various \mathbf{k}^\pm .

The points where the mode \mathbf{k}_\pm^\pm changes are marked by Δ , \triangleright , ∇ , \triangleleft . Their (λ, μ) coordinates are given in the key to leading order in ϵ . Next, we display the \mathbf{k}_\pm^\pm in the k_x - k_y plane and identify their values.

3.4.2 The k_x - k_y plane: \mathbf{k}_\pm^\pm are the modes at which $n_{\mathbf{k}}^{\text{RJ}}$ becomes singular

In figure 3.3, each panel shows the k_x - k_y plane, with the lattice L_ϵ marked in dark grey points and the square S_ϵ in light grey. We plot the parametric curves $D(\mathbf{k}, \mu^+(\lambda), \lambda) = 0$ (top row) and $D(\mathbf{k}, \mu_-(\lambda), \lambda) = 0$ (bottom row), with λ increasing from left to right.

In each panel $\mathbf{k}_\pm^\pm(\lambda)$ is shown by the coloured dot, and is the wavenumber where the $D = 0$ curve first intersects a point in L_ϵ (or first touches S_ϵ in the continuous integral approach). Colours for $\mathbf{k}_\pm^\pm(\lambda)$ and the $D = 0$ curve correspond to the coloured portions of $\mu^\pm(\lambda)$ in figure 3.2, and label the mode $\mathbf{k}_\pm^\pm(\lambda)$ for the ranges of λ we now detail.

3.4.2.1 Bottom row of figure 3.3.

The $T < 0$ case is simpler so we consider it first to fix concepts. Expressions for $\mathbf{k}_-(\lambda)$ can be found by minimising $\mu(\mathbf{k}, \lambda)$ on L_ϵ by elementary means (identical

¹We use superscripts on variables when referring to their values on the upper RJ boundary, i.e. with positive T , subscripts to refer to their values on the negative T boundary, and both scripts simultaneously, e.g. $\mu_\pm^\pm(\lambda)$, $\mathbf{k}_\pm^\pm(\lambda)$, when speaking of both boundaries at once. Had we chosen μ as the independent variable we could define $\lambda_\pm^\pm(\mu)$ and $\mathbf{k}_\pm^\pm(\mu)$ analogously. For compactness we sometimes suppress explicit dependence on the independent variable, when the context is clear.

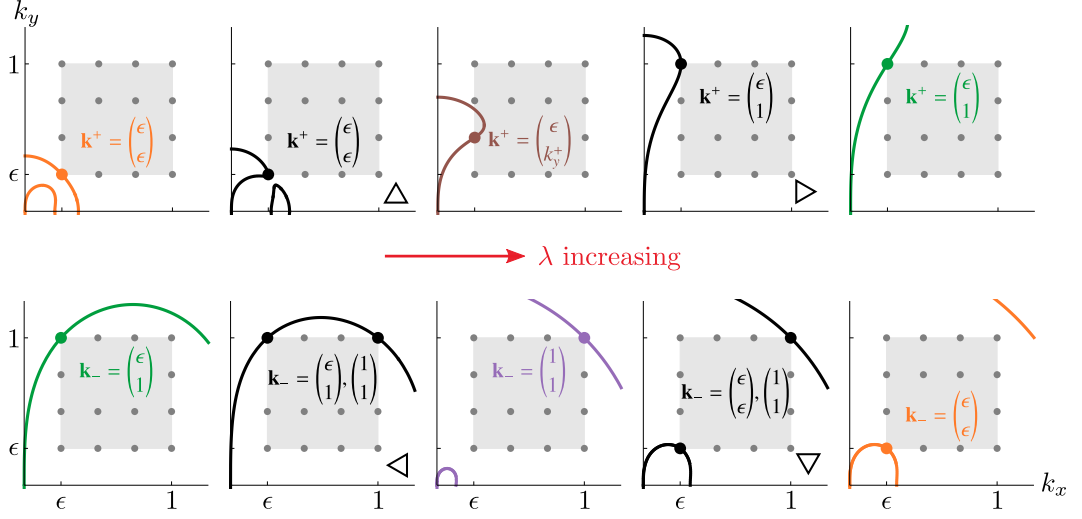


Figure 3.3: k_x - k_y plane showing the curve $D = 0$ intersecting $L_{1/4}$ (dark grey lattice) at the mode \mathbf{k}^+ (top row, for the boundary of the $T > 0$ region) or \mathbf{k}_- (bottom row, for the boundary of the $T < 0$ region). Typical configurations are shown for each regime of $\mathbf{k}_\pm(\lambda)$ detailed in (3.18) and (3.17), distinguished by colour. Panels labelled with black triangles correspond to the transitions between the different $\mathbf{k}_\pm(\lambda)$ regimes. The light grey square is $S_{1/4}$.

results are found when we use continuous integrals). We obtain

$$\mathbf{k}_-(\lambda) = \begin{cases} \begin{pmatrix} \epsilon \\ 1 \end{pmatrix} & \text{for } \lambda \leq \lambda_{\triangleleft} = -\frac{8(1+\epsilon^2)^4}{3-25\epsilon^2-15\epsilon^4-3\epsilon^6}, \\ \begin{pmatrix} 1 \\ 1 \end{pmatrix} & \text{for } \lambda_{\triangleleft} \leq \lambda \leq \lambda_{\nabla}, \\ \begin{pmatrix} \epsilon \\ \epsilon \end{pmatrix} & \text{for } \lambda \geq \lambda_{\nabla} = \frac{16}{3} \frac{\epsilon^4}{1+\epsilon^2}. \end{cases} \quad (3.17)$$

Each panel of figure 3.3 shows a representative configuration for the $D = 0$ curve, and the corresponding location for \mathbf{k}_- , as one moves from left to right along the bottom RJ boundary $\mu_-(\lambda)$ in figure 3.2. The mode \mathbf{k}_- over which $n_{\mathbf{k}}^{\text{RJ}}$ diverges is at first at the smallest zonal scale; then isotropic at the smallest scale of the system; then isotropic at the largest scale.

Transitioning between these three cases (we will refer to the three cases in (3.17) as “ \mathbf{k}_- regimes” in what follows), \mathbf{k}_- jumps discontinuously, due to the $D = 0$ curve touching L_ϵ at two different Fourier modes simultaneously. These transitions are shown in black in figure 3.3, in the panels labelled \triangleleft and ∇ . They are marked likewise in the λ - μ plane in figure 3.2, and occur at coordinates $(\lambda_{\triangleleft}, \mu_{\triangleleft})$ and $(\lambda_{\nabla}, \mu_{\nabla})$, whose leading-order behaviour with ϵ is given in the key.

3.4.2.2 Top row of figure 3.3.

For the $T > 0$ case we maximise $\mu(\mathbf{k}, \lambda)$ to find

$$\mathbf{k}^+(\lambda) = \begin{cases} \binom{\epsilon}{\epsilon} & \text{for } \lambda \leq \lambda^\Delta = \frac{16\epsilon^6}{7}, \\ \binom{\epsilon}{k_y^+(\lambda)} & \text{for } \lambda^\Delta \leq \lambda \leq \lambda^\triangleright, \\ \binom{\epsilon}{1} & \text{for } \lambda \geq \lambda^\triangleright = \frac{(1+\epsilon)^5}{\epsilon^2(15-\epsilon^2)}. \end{cases} \quad (3.18)$$

Between these three cases (henceforth “ \mathbf{k}^+ regimes”), $\mathbf{k}^+(\lambda)$ transitions with no jump, see the panels labelled Δ and \triangleright in figure 3.3. The transitions are marked likewise in figure 3.2, with (λ, μ) coordinates $(\lambda^\Delta, \mu^\Delta)$ and $(\lambda^\triangleright, \mu^\triangleright)$, given to leading order in ϵ in the key.

In (3.18), $k_y^+(\lambda)$ is different when discrete sums are used in (3.12) vs. using continuous integrals. In the latter, $n_{\mathbf{k}}^{\text{RJ}}$ becomes divergent when the $D = 0$ curve first meets the square S_ϵ , i.e. (ϵ, k_y^+) is the point where S_ϵ is tangent to $D = 0$. Correspondingly, k_y^+ is the real root in $[\epsilon, 1]$ of the 10th-degree polynomial found by solving $\partial_{k_y} \mu(k_x = \epsilon, k_y, \lambda) = 0$, and increases continuously with λ .

When discrete sums are used the $D = 0$ curve is only constrained by the lattice L_ϵ , and can penetrate between the lattice points slightly, as exemplified in the middle panel, top row of figure 3.3. Thus, $k_y^+ = j\epsilon$ for $j = 1, \dots, \epsilon^{-1}$, and increases piecewise with λ so that $\mathbf{k}^+ = (\epsilon, k_y^+)$ transitions discontinuously up the left-hand edge of L_ϵ . At the transitions the $D = 0$ curve touches two adjacent lattice points and \mathbf{k}^+ represents two neighbouring Fourier modes.

For $T > 0$, then, moving along the top RJ boundary $\mu^+(\lambda)$ in figure 3.2, the mode \mathbf{k}^+ over which $n_{\mathbf{k}}$ diverges is of the largest scale in both x and y (fully isotropic); remains largest in x and shrinks in y (becoming more zonally anisotropic as λ increases); and finally ends up at the largest possible scale in the x -direction and smallest scale in the y -direction (smallest-scale zonal mode).

For clarity we have set $\epsilon = 1/4$ in figure 3.3; the behaviour is qualitatively the same for smaller values of ϵ . In each panel of figure 3.3 we have displayed representatives of each $\mathbf{k}^\pm(\lambda)$ regime detailed in (3.17), (3.18). Within each regime the $\mathbf{k}^\pm(\lambda)$ remain the same despite the $D = 0$ curve changing shape, or even topology, as λ and $\mu^\pm(\lambda)$ change.

3.4.3 Regularity of the RJ spectrum, negative thermodynamic potentials

In summary, every (λ, μ) point lying in either of the white ($T > 0$ or $T < 0$) regions in figure 3.2 gives summands over L_ϵ in (3.12) that are all positive, corresponding to a physical RJ spectrum. In figure 3.2(b) we sketch the λ - μ plane schematically,

with the axes crossings labelled, to show that RJ states are possible for any sign combination of (T, μ, λ) , except for the case $T < 0, \mu > 0, \lambda > 0$. We also show (vertical blue) lines of constant λ and (horizontal red) lines of constant μ in the RJ-accessible regions. These schematically show the lines of approach to the RJ boundary corresponding to the panels of figure 3.4, and labelled accordingly.

As we will discuss in the next section, when the (λ, μ) point approaches the RJ boundary, the spectrum $n_{\mathbf{k}}^{\text{RJ}}$ becomes increasingly peaked at the \mathbf{k}_{\pm}^+ corresponding to that boundary point. Thus the various \mathbf{k}_{\pm}^+ are the fundamental modes into which the invariants will condense on the RJ spectrum. In the CHM the fundamental mode of condensation shows great diversity—isotropic, anisotropic, small-scale and large-scale—as compared to the isotropic 2D GPE or Euler equations, for which condensation only occurs into isotropic modes at the gravest or the smallest scale.

Inspection of figure 3.2(b) shows that proximity to the boundary, and hence condensation, is associated with at least one thermodynamic potential becoming negative. However this is not a sufficient condition for condensation as there are many regions of the λ - μ plane that have negative potentials but are remote from the RJ boundary, for example deep inside the quadrant $(T, \mu, \lambda) \ll 1$. Thus, while it is necessary for at least one of (T, μ, λ) to be negative in order to have a condensate, this condition is not sufficient. In the next section we will see that the necessary proximity of the (λ, μ) point to the RJ boundary in order to have condensation depends strongly on ϵ .

Finally, as the (λ, μ) point passes inside the RJ-forbidden grey region in λ - μ space, the $D = 0$ curve in k_x - k_y space envelops at least one lattice point $\mathbf{k} \in L_{\epsilon}$. This means that D , and hence $n_{\mathbf{k}}^{\text{RJ}}$, changes sign for that \mathbf{k} , so the RJ spectrum is no longer positive-definite and ceases to remain physically meaningful. If we are using continuous integrals, when the (λ, μ) point passes inside the RJ-forbidden region, the $D = 0$ curve in k_x - k_y space penetrates S_{ϵ} and envelops a portion of S_{ϵ} with finite area. At those “captured” modes $n_{\mathbf{k}}^{\text{RJ}}$ will become negative, which is unphysical. As discussed in section 3.4.2.2, the $D = 0$ curve can penetrate between lattice points of L_{ϵ} slightly, but this captures a finite-area portion of S_{ϵ} . Thus the grey RJ-forbidden region in λ - μ space is thus slightly bigger when using continuous integrals vs. using discrete sums.

3.5 Condensation in the RJ spectrum

Consider a sequence of equilibrium states lying on a vertical blue line of constant λ in figure 3.2(b). Starting from a point deep in the RJ-accessible region and approaching the boundary $\mu_{\pm}^+(\lambda)$, the curve $D = 0$ approaches the L_{ϵ} lattice, and the spectrum becomes increasingly peaked over the mode(s) $\mathbf{k}_{\pm}^+(\lambda)$. Finally when $\mu = \mu_{\pm}^+(\lambda)$,

the curve touches L_ϵ at \mathbf{k}_-^+ , as typified by one of the panels in figure 3.3, and the spectrum $n_{\mathbf{k}}^{\text{RJ}}$ becomes singular at \mathbf{k}_-^+ . Likewise we could approach the RJ boundary along a horizontal red line in figure 3.2(b), keeping μ fixed and approaching $\lambda_-^+(\mu)$, with the spectrum becoming increasingly peaked, and finally singular, at $\mathbf{k}_-^+(\mu)$.

As the spectrum at \mathbf{k}_-^+ becomes increasingly peaked, the term (or terms, in the cases where \mathbf{k}_-^+ represents two different Fourier modes) containing \mathbf{k}_-^+ in (3.12) starts to dominate the sum. Thus, as (λ, μ) moves to the edge of the RJ-accessible region, the spectrum becomes a Kronecker delta:

$$n_{\mathbf{k}}^{\text{RJ}} \rightarrow \delta_{\mathbf{k}, \mathbf{k}_-^+}, \quad (3.19)$$

or a linear combination of Kronecker deltas, when \mathbf{k}_-^+ represents two different modes,

$$n_{\mathbf{k}}^{\text{RJ}} \rightarrow \alpha \delta_{\mathbf{k}, \mathbf{k}_1} + (1 - \alpha) \delta_{\mathbf{k}, \mathbf{k}_2}, \quad 0 < \alpha < 1, \quad (3.20)$$

for example $\mathbf{k}_1 = (\epsilon, 1)$, $\mathbf{k}_2 = (1, 1)$ at the \triangleleft point.

Eventually in the singular limit (3.19) (or (3.20)) all three invariants are contained in the mode(s) \mathbf{k}_-^+ while the rest of \mathbf{k} -space contributes a vanishingly small amount: the invariants have condensed at the fundamental mode(s) \mathbf{k}_-^+ . Simultaneously we must have $T \rightarrow 0$ in order to keep the total (Ω, E, Z) constant. We stress that this condensation happens entirely within the RJ spectrum, unlike the case for the 3D GPE where a singular spectrum at $\mathbf{k} = 0$ arises to absorb the excess particles below a finite transition temperature.

We examine the approach to condensation in figure 3.4, where in each panel of three triptychs we plot the ratio of each invariant that is contained in mode $\mathbf{k}_-^+(\lambda)$ to the total, for example $\Omega_{\mathbf{k}_-^+}/\Omega$ etc., as we approach points on the RJ boundary representative of each \mathbf{k}_-^+ . These lines of approach are shown schematically in figure 3.2(b).

In figure 3.4(a) we plot these fractions as a function of $\delta\mu = |\mu - \mu_-^+(\lambda)|$, i.e. moving along a blue line in figure 3.2(b) towards $\mu_-^+(\lambda)$. $T > 0$ in the top row of triptychs and $T < 0$ in the bottom row. (In panel 3.4(a,b)(ii), $\lambda^{(1/2)}$ is the value that makes $k_y^+(\lambda^{(1/2)}) = 1/2$.)

In figure 3.4(b) we approach the same points on the RJ boundary horizontally, along the red lines in figure 3.2(b), plotting the fractions of invariants contained in mode \mathbf{k}_-^+ as a function of $\delta\lambda = |\lambda - \lambda_-^+(\mu)|$. Again $T > 0$ in the top row and $T < 0$ in the bottom row.

Within each triptych, the system size increases moving down the panels. The plots are qualitatively similar whichever locations on the RJ boundary are chosen within the \mathbf{k}_-^+ regimes.

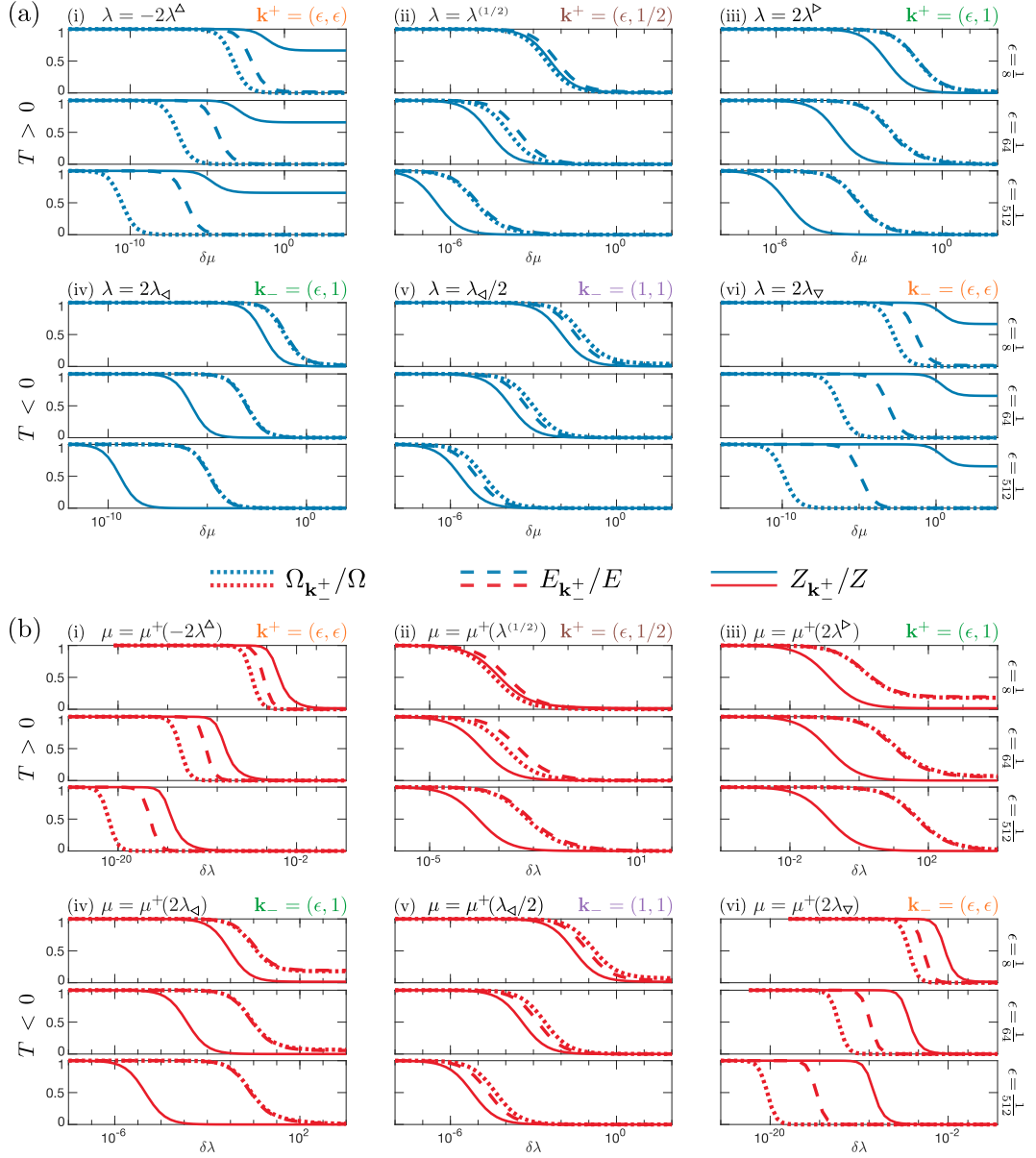


Figure 3.4: Fraction of the total invariants that are contained within mode \mathbf{k}_+^+ as a function of (a) $\delta\mu$, or (b) $\delta\lambda$, for the representative points on the RJ boundary within each regime of \mathbf{k}_+^+ shown schematically in figure 3.2(b). $T > 0$ for the top row in parts (a) and (b) and $T < 0$ in the bottom row in both parts. Within each triptych, each panel represents a different system size ϵ .

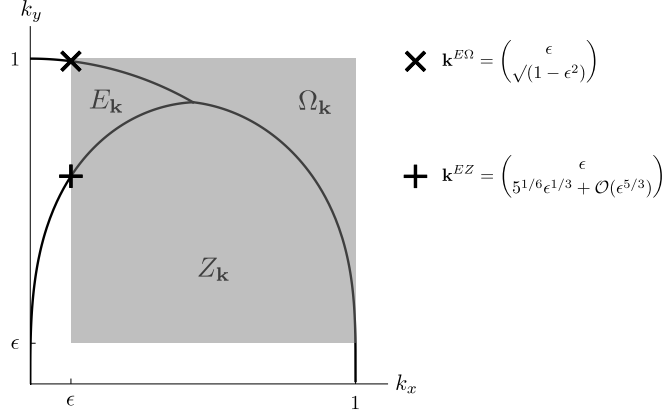


Figure 3.5: Sectors of \mathbf{k} -space labelled by the invariant spectrum that is dominant deep inside each sector. The grey square is $S_{1/8}$, whose left-hand edge intersects the isolines $E_{\mathbf{k}} = \Omega_{\mathbf{k}}$ and $E_{\mathbf{k}} = Z_{\mathbf{k}}$ at the points marked by \times and $+$ respectively.

3.5.1 Finite-size condensation at the edge of the RJ region

Examining figure 3.4, we see that as we approach the RJ boundary from either direction, all three invariants condense into the fundamental mode \mathbf{k}_-^+ for any finite ϵ , as predicted above. We also see that for different parts of the RJ boundary (different \mathbf{k}_-^+ regimes), different invariants condense first, i.e. at larger $\delta\lambda$ or $\delta\mu$. Which invariant condenses first can be explained by considering which invariant spectrum is dominant at the \mathbf{k}_-^+ under consideration. In figure 3.5 we plot the isolines where each pair of invariant spectra are equal ($E_{\mathbf{k}} = Z_{\mathbf{k}}$ etc.). This divides L_ϵ into three sectors, deep inside of which one invariant will dominate the other two. The strength of this dominance at a particular \mathbf{k} goes as the ratio of the dominant invariant to the others, at the \mathbf{k} in question.²

Thus, when $n_{\mathbf{k}}^{\text{RJ}}$ is becoming increasingly concentrated at $\mathbf{k}_-^+ = (\epsilon, \epsilon)$, it is $Z_{\mathbf{k}}$ that dominates there and so zonostrophy condenses first into that mode, as we find in figure 3.4(a,b)(i) and 3.4(a,b)(vi). Note that the $+$ point on the $E_{\mathbf{k}} = Z_{\mathbf{k}}$ boundary converges to the origin as $\epsilon^{1/3}$. This is slower than the convergence of the mode (ϵ, ϵ) , guaranteeing that this mode remains in the $Z_{\mathbf{k}}$ sector as $\epsilon \rightarrow 0$, and so is always associated with zonostrophy condensing first.

Similar arguments show that the concentration of $n_{\mathbf{k}}^{\text{RJ}}$ into zonal modes $\mathbf{k}^+ = (\epsilon, k_y^+)$ is associated with energy condensing first. In figure 3.4(a,b)(ii) we monitor condensation into $\mathbf{k}^+ = (\epsilon, 1/2)$. The ratio of energy to enstrophy densities is $E_{\mathbf{k}}/\Omega_{\mathbf{k}} = k^{-2}$, which goes as $\sim 1/4$ at this mode as $\epsilon \rightarrow 0$, so E condenses ahead of Ω by a factor which tends to a constant. By contrast $E_{\mathbf{k}}/Z_{\mathbf{k}} = k^8/k_x^2$ so the

²As mentioned in section 3.2, figure 3.5 is also instrumental in applying the Fjørtoft argument to weakly-nonlinear CHM systems. If the system is forced at a particular \mathbf{k}_f then one can draw three sectors whose boundaries intersect at \mathbf{k}_f exactly as in figure 3.5. Each sector will host the cascade of the invariant whose density dominates there, see [36].

condensation of Z lags that of E at a rate $\sim \epsilon^{-2}$ at this mode.

When $n_{\mathbf{k}}^{\text{RJ}}$ becomes concentrated into the smallest-scale zonal mode $\mathbf{k}_{-}^{\pm} = (\epsilon, 1)$, this mode lies near the boundary of the $\Omega_{\mathbf{k}}$ and $E_{\mathbf{k}}$ sectors (the \times point on this boundary converges quickly to the point $(\epsilon, 1)$ so as $\epsilon \rightarrow 0$), hence the simultaneous condensation of enstrophy and energy into this mode seen in figure 3.4(a,b)(iii), and 3.4(a,b)(iv).

Finally for concentration of $n_{\mathbf{k}}^{\text{RJ}}$ into $\mathbf{k}_{-} = (1, 1)$, this point lies deep in the $\Omega_{\mathbf{k}}$ sector, hence enstrophy condensing first in figures 3.4(a,b)(v).

To summarise, for any system of finite size there exists a layer in λ - μ space adjacent to the RJ boundary, within which we expect all three invariants to condense into mode \mathbf{k}_{-}^{\pm} . Although this is important to note, we do not expect these states to be dynamically significant as the only relevant initial conditions that will equilibrate to these states have spectra that are already highly concentrated around \mathbf{k}_{-}^{\pm} . This is to say that the very edge of the RJ region where all invariants condense will be accessed by initial conditions lying in an insignificant volume in the function space of all possible initial conditions.

However, a wider “boundary layer” of (λ, μ) values has RJ spectra that manifest condensates of one invariant, if the corresponding \mathbf{k}_{-}^{\pm} lies deep inside the sector in figure 3.5 in which that invariant density dominates. (If the \mathbf{k}_{-}^{\pm} lies near the boundary between two sectors then the wider boundary layer represents condensates of those two invariants, e.g. condensation of Ω and E but not Z for $\mathbf{k}_{-}^{\pm} = (\epsilon, 1)$.) This boundary layer of (λ, μ) values corresponds to the set in the functional space of initial conditions that will equilibrate to an RJ spectrum with one (or two) condensate(s). Comparing the size of this set to the set of initial conditions that does not lead to condensation is outside the scope of this study.

3.5.2 Lack of condensation in the infinite box limit

In figures 3.4(a)(ii)-(v), we see that the boundary layer of $\delta\mu$ values where condensates are forming gets pushed to progressively smaller values as we decrease ϵ (move down the panels within each triptych). It appears in figures 3.4(a)(i) and (vi) as if the zonostrophy condensate survives in the $\epsilon \rightarrow 0$ limit, however figures 3.4(b)(i) and (vi) reveal that approaching the same points on the RJ boundary along lines of constant μ again sends the boundary layer to progressively smaller $\delta\lambda$ as we decrease ϵ . Examining figure 3.2(b), we see that the orange parts of the RJ boundary with $\mathbf{k}_{-}^{\pm} = (\epsilon, \epsilon)$ become increasingly parallel to lines of constant λ as $\epsilon \rightarrow 0$, i.e. the $\delta\mu$ axes in figures 3.4(a)(i) and (vi) remain within the boundary layer even for large $\delta\mu$. Likewise the $\delta\lambda$ axes in figures 3.6(b)(ii)-(iv) also remain in the boundary layer, due to the shallowness of the gradient of the RJ boundary in λ - μ space in these cases.

We conclude that when we approach the RJ boundary in a perpendicular

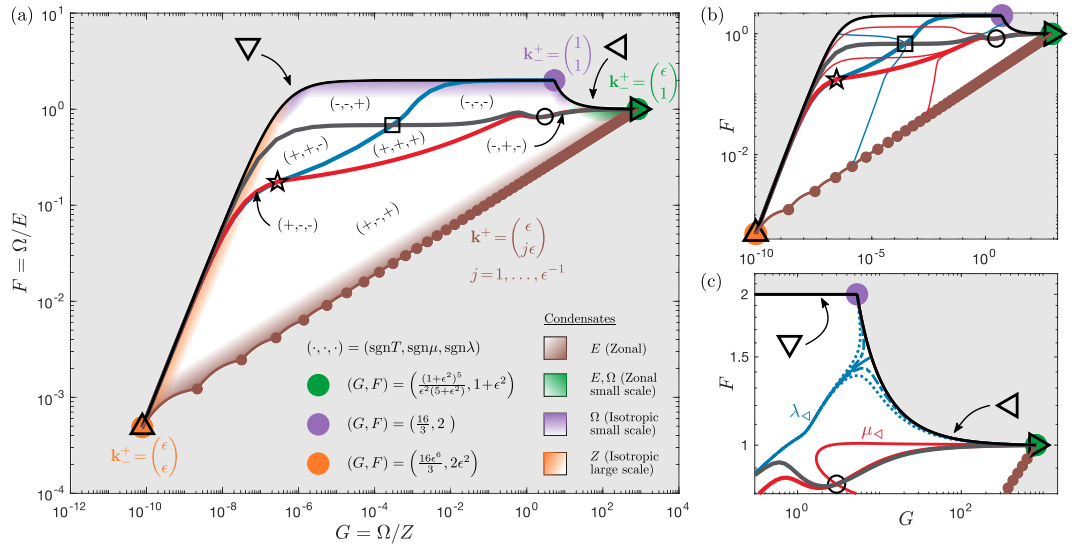


Figure 3.6: CHM phase diagram for $\epsilon=1/64$. (a) Sectors of the phase diagram are marked according to $(\text{sgn } T, \text{sgn } \mu, \text{sgn } \lambda)$, partitioned by the lines $\lambda=0$ (thick blue), $\mu=0$ (thick red), and $T, \mu, \lambda \rightarrow \infty$ (thick grey). Shaded areas suggest the boundary layer where one or two dominant invariants condense first. (b) The phase diagram with the RJ sail traversed by lines of constant λ (blue) and constant μ (red). (c) Upper right portion of the phase diagram, showing the lines $\lambda = \lambda_{\triangleleft}$ (solid blue), $\lambda_{\triangleleft} \pm 4 \times 10^{-5}$ (dashed blue), $\lambda_{\triangleleft} \pm 12 \times 10^{-5}$ (dotted blue), and $\mu = \mu_{\triangleleft}$ (solid red).

direction, transverse to the boundary layer (figures 3.4(b)(i), (vi) and (a)(ii)-(v)), we see that the boundary layer becomes progressively narrower as $\epsilon \rightarrow 0$ (although the boundary layer for the dominant invariant shrinks slower than that of the subdominant invariants). This is to say that condensation within the RJ spectrum does not remain in the infinite box limit, entirely in agreement with the Mermin-Wagner-Hohenberg theorem.

3.6 CHM phase diagram

By specifying the initial spectrum of the system we can prescribe the amount of (Ω, E, Z) present. These invariants retain their value as the spectrum evolves to equilibrium. If it is possible to accommodate the initial invariants in an RJ spectrum, then the three thermodynamic parameters (T, μ, λ) will have values that yield (Ω, E, Z) via Eqs. (3.12). We can eliminate the temperature T by considering the ratios

$$G(\mu, \lambda) = \frac{\Omega}{Z} \quad \text{and} \quad F(\mu, \lambda) = \frac{\Omega}{E}. \quad (3.21)$$

Viewing G and F as control parameters that we can manipulate through the initial spectrum, we can consider what subset of G - F space corresponds to initial conditions that equilibrate to an RJ spectrum. We find this subset by varying

λ and μ over their allowed values for physical spectra, i.e. fixing λ and sweeping μ through $(-\infty, \mu_-(\lambda)) \cup (\mu^+(\lambda), \infty)$, then fixing μ and sweeping λ through $(-\infty, \lambda_-(\mu)) \cup (\lambda^+(\mu), \infty)$. This allows us to calculate G and F via equations (3.12), and map out the sail-shaped region shown in figure 3.6. This “RJ sail” shows the range of control parameters that equilibrate to different kinds of RJ spectra, and can thus be viewed as the phase diagram of weakly nonlinear CHM turbulence. Figure 3.6 is plotted for $\epsilon = 1/64$ but is qualitatively similar for general ϵ .

3.6.1 Interior of the RJ sail

In figure 3.6(a) we show that the RJ “sail” is divided into different sectors by the thick blue line $\lambda = 0$, the thick red line $\mu = 0$, and the thick grey line. The latter is drawn by setting $|\lambda| = \text{const} \gg 1$ and sweeping through the allowed μ ; as we send $|\lambda| \rightarrow \infty$ the line collapses onto the grey line shown, which coincides with the line drawn by setting $|\mu| = \text{const} \gg 1$, sweeping λ , and sending $|\mu| \rightarrow \infty$. On this line in order to retain nonvanishing (Ω, E, Z) we need to also send $T \rightarrow \infty$, i.e. the grey line represents all of $(T, \mu, \lambda) \rightarrow \infty$.

Thus, the sectors in figure 3.6(a) each contain different combinations positive and negative (T, μ, λ) (with the $(+, -, -)$ and $(-, +, -)$ sectors lying in the indicated regions, too small to visualise at this scale). Note that by varying (G, F) continuously one can pass smoothly through the $\mu = 0$, $\lambda = 0$, and $T \rightarrow \infty$ lines continuously with no dramatic phase change, c.f. [87, 66]. The latter line separates the $T > 0$ sectors below from the $T < 0$ sectors above, which comports with the interpretation of negative temperature states being “hotter than any positive temperature” [88, 66, 89].

The coloured shading in figure 3.6(a) suggests schematically the areas near the edge of the RJ sail where we expect invariants to condense, following the arguments of section 3.5. We indicate only the condensation of the invariant(s) associated with the fundamental mode \mathbf{k}_\pm^+ that dominates the behaviour near the edge of the sail. There will also be a narrower layer adhering to the edge of the sail (not shown in figure 3.6(a)) where all three invariants condense.

Important points of reference in the interior of the RJ sail are the point \star (representing $\lambda = \mu = 0$); and the points \square (for $\mu = \pm\infty$), which is an accumulation point for all lines of constant λ at their $\mu \rightarrow \pm\infty$ limit; and \circ (for $\lambda = \pm\infty$) which accumulates all lines of constant μ at their $\lambda \rightarrow \pm\infty$ limit. The accumulation of constant λ and μ lines at \square and \circ is shown in figure 3.6(b) where we plot several lines of constant λ and μ to chart out the coordinate lines in the interior of the RJ sail.

3.6.2 Boundary of the RJ sail

The RJ boundary in the G - F plane is defined by the singular limits of the RJ spectrum (3.19) and (3.20). In particular when the spectrum becomes a single Kronecker delta (3.19), the entire segment of the RJ boundary in λ - μ space corresponding to that \mathbf{k}_-^+ collapses to a point in G - F space. These are the orange, green, purple, and brown points in figure 3.6, labelled with their respective \mathbf{k}_-^+ in figure 3.6(a). The ϵ dependences of the first three points are also given in the figure; we see that as $\epsilon \rightarrow 0$ the RJ sail expands to cover the entire part of G - F space with $F \leq 2$ (limited from above by the entire spectrum condensing into $\mathbf{k}_- = (1, 1)$).

The orange and green points also coincide respectively with the \triangle and \triangleright points that mark the transition between different \mathbf{k}^+ regimes, as per (3.18). This reflects the fact that each \mathbf{k}^+ transition happens at a single mode, (ϵ, ϵ) and $(\epsilon, 1)$ respectively.

By contrast, the transitions \triangleleft and ∇ each involve two different \mathbf{k}_- modes, see (3.17), so the spectrum at these points becomes the sum of two Kronecker deltas (3.20). Their relative weighting α will depend on the direction of approach to the RJ boundary: along a line of constant μ , a line of constant λ , or some other angle. This is demonstrated in figure 3.6(c) for the \triangleleft point. In the λ - μ plane the lines $\lambda = \lambda_{\triangleleft}$ and $\mu = \mu_{\triangleleft}$ both approach the *same* point \triangleleft on the RJ boundary, but from different directions, (consequently their respective approach to the \triangleleft point favours $\mathbf{k}_- = (\epsilon, 1)$ or $(1, 1)$ in different amounts). However the images of these lines in the G - F plane terminate on the RJ boundary at *different* points. Changing the angle of approach to \triangleleft in λ - μ space changes the weighting $\alpha \in [0, 1]$ in (3.20), which sweeps out the black line labelled \triangleleft in figure 3.6 that forms the upper right boundary of the RJ sail.

We also plot the lines $\lambda = \lambda_{\triangleleft} \pm \Delta\lambda, 3\Delta\lambda$, with $\Delta\lambda = 4 \times 10^{-5}$, to show that lines either side of λ_{\triangleleft} terminate at the purple (+ sign) and green (- sign) points representing their respective \mathbf{k}_- modes. Viewed as a dynamical system, the λ_{\triangleleft} trajectory is the separatrix between the basins of attraction of the purple and green stable fixed points, which attract constant λ trajectories.

Similarly the entire upper left boundary (black in figure 3.6) is formed by the spectrum linearly interpolating between the \mathbf{k}_- modes at the ∇ point, and the lower right boundary (brown) is formed by the $(\epsilon^{-1} - 1)$ interpolations between the successive zonal modes $\mathbf{k}^+ = (\epsilon, j\epsilon)$, $j = 1, 2, \dots, \epsilon^{-1}$.

As mentioned in section 3.5, as we approach the boundary of the RJ sail, the denominator of $n_{\mathbf{k}}^{\text{RJ}}$ is shrinking to zero, so in order to keep (Ω, E, Z) finite, T must also vanish. In figure 3.6 we must have $T \rightarrow 0^+$ as we approach the brown boundary, and $T \rightarrow 0^-$ as we approach either black boundary.

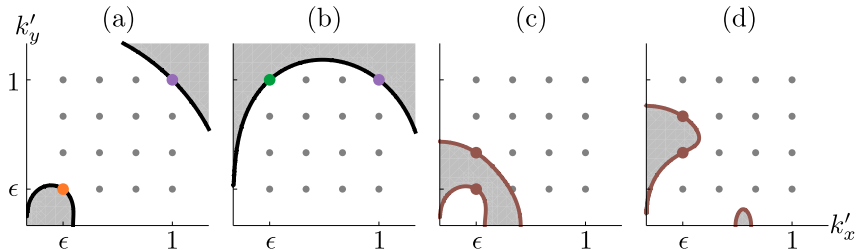


Figure 3.7: $\text{sgn } P(\alpha, \mathbf{k}_1, \mathbf{k}_2, \mathbf{k}')$ over \mathbf{k}' space for $L_\epsilon = 1/4$, $\alpha = 1/2$. We choose \mathbf{k}_1 and \mathbf{k}_2 so that P represents perturbations of the spectrum away from boundaries of the RJ sail in figure 3.6: (a) ∇ black boundary, (b) \triangleleft black boundary, (c) first segment of the lower brown boundary, (d) second segment of the lower brown boundary. The thick black or brown lines are contours of $P = 0$, white areas denote $P > 0$, and grey areas $P < 0$.

3.6.3 Outside the RJ sail

In section 3.5.2 we noted that condensates within the RJ spectrum only exist at finite size and do not remain in the $\epsilon \rightarrow 0$ limit. Equivalently, in this limit any spectrum initialised over the lattice L_ϵ equilibrates to an RJ spectrum with some physically meaningful (T, μ, λ) . A related question is, for finite ϵ , whether singular spectra could exist that contain a macroscopic amount of invariants, but which lie outside the RJ spectrum. If such a spectrum exists, this possibility would be similar to Bose-Einstein condensation in the 3D GPE in a spatially infinite system, where below the condensation temperature excess particles are absorbed into the singular spectrum $\delta(\mathbf{k})$. Equivalently we can ask whether there are initial spectra that contain combinations of (Ω, E, Z) that cannot be accommodated by any (T, μ, λ) in an RJ spectrum. This amounts to asking whether there is any physical spectrum that maps to a point outside the RJ sail.

To address this we note that in the discrete description, any arbitrary but physically meaningful spectrum is a non-negative function over L_ϵ , i.e. it is a linear combination of Kronecker deltas on each lattice point: $n_{\mathbf{k}} = \sum_{\mathbf{k}' \in L_\epsilon} a_{\mathbf{k}'} \delta_{\mathbf{k}, \mathbf{k}'}$. In particular, any spectrum that maps to a point outside the RJ sail in the $G-F$ plane must also have this structure. We therefore proceed by choosing a spectrum corresponding the boundary of the RJ sail and examining all possible small perturbations

$$n_{\mathbf{k}}^{\text{RJ}(\text{bdry})} \rightarrow n_{\mathbf{k}}^{\text{RJ}(\text{bdry})} + \eta \delta_{\mathbf{k}, \mathbf{k}'}, \quad (3.22)$$

where $\eta \ll 1$, $\mathbf{k}' \in L_\epsilon$, and $n_{\mathbf{k}}^{\text{RJ}(\text{bdry})}$ is the limiting spectrum (3.20) on the RJ boundary. (We do not consider the limit (3.19) as the observations of section 3.6.2 show that such spectra map to a finite number of isolated points in the $G-F$ plane.) If all such small perturbations to the spectrum were to map to points in the $G-F$ plane that are inside the RJ sail, we conjecture that any finite perturbation would

map to a points even further inside the sail. We further reason that any arbitrary combination of finite perturbations from the boundary would also land inside the RJ sail, i.e. *any* physical spectrum would be represented inside the RJ sail in G - F space.

First we recall that the black and brown boundary lines of the RJ sail represent systems with spectra given by (3.20), i.e. a sum of two Kronecker deltas. For any of these boundaries, a point parametrised by α has e.g. zonestrophy

$$Z^\delta = \alpha\varphi_1 + (1 - \alpha)\varphi_2,$$

and similarly enstrophy Ω^δ and energy E^δ with $\varphi_{\mathbf{k}}$ replaced by k_x and $|\omega_{\mathbf{k}}|$ respectively.³

This point on the RJ boundary in G - F space has coordinates $G^\delta = \Omega^\delta/Z^\delta$ and $F = \Omega^\delta/E^\delta$. The tangent vector in the G - F plane is then $(\partial_\alpha G^\delta, \partial_\alpha F^\delta)$, and the inward pointing normal vector

$$\mathbf{N}^\delta = \pm \left(\partial_\alpha F^\delta, -\partial_\alpha G^\delta \right)$$

is selected by choosing the appropriate sign.

We then perturb the spectrum by introducing a Kronecker delta at \mathbf{k}' as in (3.22), and calculate the invariants

$$Z^\eta = \alpha\varphi_1 + (1 - \alpha)\varphi_2 + \eta\varphi_{\mathbf{k}'}$$

etc, then take ratios to find G^η and F^η . The vector

$$\mathbf{X}^\eta = (\partial_\eta G^\eta, \partial_\eta F^\eta)_{\eta=0}$$

then indicates the direction that the perturbation (3.22) takes the point lying on the RJ boundary in the G - F plane. Finally, the sign of the quantity

$$P(\alpha, \mathbf{k}_1, \mathbf{k}_2, \mathbf{k}') = \mathbf{N}^\delta \cdot \mathbf{X}^\eta$$

determines whether the perturbation (3.22) takes the (G, F) point into the RJ region ($P > 0$) or outside it ($P < 0$).

In figure 3.7 we plot $\text{sgn } P(\alpha, \mathbf{k}_1, \mathbf{k}_2, \mathbf{k}')$ over \mathbf{k}' space, for $\mathbf{k}_1, \mathbf{k}_2$ corresponding to: (a) the upper left black boundary ∇ of the RJ sail; (b) the upper right black boundary \triangleleft ; (c) the first segment of the lower right brown boundary with $\mathbf{k}_1 = (\epsilon, \epsilon)$, $\mathbf{k}_2 = (\epsilon, 2\epsilon)$; and (d) another segment of the lower right brown boundary

³In this section superscripts label the character of spectra, invariants, etc. and no longer refer to quantities on the $T > 0$ branch of the RJ spectrum. Nor do they imply any summation over tensor indices.

with $\mathbf{k}_1 = (\epsilon, j\epsilon)$, $\mathbf{k}_2 = (\epsilon, (j+1)\epsilon)$; here $j=2$ but the diagram is similar for any $1 < j < (\epsilon^{-1}-1)$. The black and brown contours mark $P = 0$, the white regions denote $P > 0$ and the grey regions $P < 0$. In figures 3.7(a)-(d) we have chosen $\epsilon = 1/4$ for clarity, but the figures are qualitatively similar as we decrease ϵ . We plot the figures with $\alpha = 1/2$; as we change α the contours of $P = 0$ do not change appreciably, however the contours inside $P > 0$ and $P < 0$ (not shown in figure 3.7 for clarity) change scale rapidly with α .

In all of figures 3.7(a)-(d), we observe that $P \geq 0$ for each $\mathbf{k}' \in L_\epsilon$. We note that in (c) the $P < 0$ region isolates the lattice point $\mathbf{k}' = (\epsilon, \epsilon)$ from the rest of L_ϵ , however in all cases we have examined, no lattice point lies within the $P < 0$ region. We thus conclude that no infinitesimal perturbation of the spectrum away from $n_{\mathbf{k}}^{\text{RJ(bdry)}}$ can reach a point outside the RJ sail pictured in figure 3.6. By the argument above we conjecture that no finite perturbation from (3.20), i.e. no physically allowable spectrum, corresponds to a point outside the sail: every physical spectrum will thermalise to an RJ distribution.

3.7 Discussion and conclusion

We have carried out a comprehensive study of the equilibrium RJ spectra of the CHM equation in its WT limit, in a double Fourier-truncated system. We have identified the range of thermodynamic parameters λ and μ that correspond to physical equilibria, and the fundamental modes \mathbf{k}_\pm^+ at which the RJ spectrum becomes singular and condense significant fractions of the dynamical invariants. The presence of three invariants widens the variety of fundamental modes that can accumulate condensates, as compared to the 2D Euler and GPE cases with two invariants. In addition to condensates at the gravest (largest-scale) and smallest-scale mode, as in the two-invariant case, in the three-invariant CHM system we have condensates at every zonal mode.

We have found that the invariant (or invariants) that condense at each fundamental \mathbf{k}_\pm^+ is the invariant whose density dominates in the sector where that \mathbf{k}_\pm^+ is located. Thus, Ω condenses into the smallest-scale modes, either isotropic or zonal; E condenses into zonal modes; and Z into the gravest isotropic mode. We have thus an explanation for the turbulent construction of ordered structures such as zonal jets, and large and small vortices in quasi-2D flows with a β effect, in terms of the equilibria sought by the turbulence. This explanation is the equilibrium equivalent of the the Fjørtoft argument regarding how the condensates will form dynamically via the cascade of invariants [36]. Indeed the two scenarios work hand in hand, with dynamical cascades bringing the system from its initial condition to an RJ equilibrium.

Furthermore, we can speculate on the subsequent evolution if there is weak dissipation in the system, for example viscous processes at the smallest scale. The Fjørtoft argument can be expressed in terms of the centroids of invariants: scales that characterise the location of the invariants in \mathbf{k} -space. If the spectrum changes, it does so in such a way that the centroid of each invariant moves deeper into its respective sector [36, 3]. The leak of Ω from the system at high k due to viscous dissipation would simultaneously push the E and Z centroids deeper into their sectors. Dissipation at high k would thus strengthen zonal or large-scale isotropic condensates. A similar process has been suggested for the dynamic formation of Bose-Einstein condensates via evaporative cooling in the GPE [3]. We expect that in the CHM, initial spectra that equilibrate to states without condensates in a closed system (the initial spectra have invariants such that the (G, F) point lands deep inside the RJ sail) will eventually grow zonal and/or large-scale isotropic condensates if the dynamics includes high- k dissipation. This would be demonstrated by monitoring the (G, F) point, which would move under dissipative dynamics towards the origin of the G - F plane as Ω is lost from the system. As the system nears the boundary of the RJ sail, a condensate will develop at the \mathbf{k}^\pm corresponding to the nearest point on the sail boundary. It would be interesting to relate this mode to the location of the E and Z centroids as they move from their initial location, c.f. [36]. Such a study would link the turbulent dynamics of the triple cascade to the equilibrium picture we have elucidated in this work. (However, initial conditions will have to be carefully chosen so as to keep the system within the weak WT regime, see below.)

We note that the condensates we have described in this chapter do not survive in the infinite box limit. However, the large-scale character of Rossby (drift) waves and zonal flows is such that their size is comparable to the planetary atmosphere or ocean (fusion device) in which they propagate. Thus the examination we have carried out here of finite-sized systems remains practically relevant.

This analytical study leaves open some questions regarding the dynamical relevance of condensates, in terms of relating the width of the “boundary layer” near the RJ edge to the volume of initial conditions that can equilibrate to a condensed state. This is to say, whether a wide range of initial conditions will evolve into an equilibrium state with a condensate, or whether it is necessary to start with an initial condition that is already similar to an RJ spectrum with a condensate. Careful characterisation of this question would require relating physically-relevant norms in the functional space of initial conditions to the area of the boundary layer in the λ - μ plane.

We also have not related states of negative thermodynamic potential to entropy derivatives, as has been recently done for GPE-like systems [89, 90]. We leave

this challenge open to future work.

All the results we have presented here take place in the context of ensembles of weakly-nonlinear waves characterised by the dispersion relation (3.2) and evolving according to the kinetic equation (3.4). Once a strong condensate has formed by dynamical turbulent processes such as the triple cascade, the weak WT description is no longer applicable, and it is natural to enquire what the leading-order changes to the dynamics are in this case. This question has most fully been answered for the case of zonal energy condensates, where the principal influence of a strong zonal flow can be summarised as the suppression of small-scale waves [33, 70, 37, 39]. Briefly, the leading-order effect is a modification of the dispersion relation (3.2) to account for the Doppler shift induced by the velocity of the zonal flow, which is strongly sheared in the y direction. As a consequence of this coordinate-dependent Doppler shift, wavepackets of small-scale waves will be distorted as they move across the shear [33, 70]. A WKB analysis reveals that the waveaction of these packets remains constant, whereas their energy decreases. However, the total energy of the system must remain constant, and so the net effect is the nonlocal transfer from the small-scale wavepackets to the large-scale zonal flows [91, 37]. Indeed, this effect of suppression of small-scale turbulence by the zonal flows is the key feature of CHM systems that makes it such a fundamental object of study in geo- and plasma physics [39]. (For a strong isotropic condensate the same shearing mechanism will dominate the interaction between small-scale wavepackets and the large-scale isotropic vortex.) These effects are in stark contrast to the case of the GPE, where the WT of 4-wave interactions described in 3.A breaks down when the condensate becomes strong, to be replaced by 3-wave turbulence of Bogoliubov waves fluctuating about a strong condensate [19].

The crossover between the regime of equilibration to the RJ states that we have characterised in this chapter, and the scenario outlined above where waves directly interact with strong condensates, merits further investigation via numerical studies. It would be very interesting indeed to probe precisely in what way the assumptions of weak WT break down during this crossover. For example, we expect the emergence of a strongly nonlinear condensate to be associated with phase correlations between Fourier modes, the spread of these correlations, and the emergence of a regime of critical balance where the linear and nonlinear timescales equalise for these modes. The full characterisation of such effects would be a research direction that would touch at the heart of WT theory.

Finally, we note that the three-invariant case considered here arises in the small-scale limit of the CHM $\rho k \gg 1$. In the large-scale limit $\rho k \ll 1$, which is more relevant to fusion plasmas, there is a fourth invariant [92], termed the semi-action [39]. The Fjørtoft argument was extended to this four-invariant case by

Harper and Nazarenko [40]. Classifying the condensation behaviour in this case, using the methodology we have developed here, is an obvious next step in fully characterising Rossby and drift wave turbulence.

3.A Appendix: Application to the Gross-Pitaevskii equation

Here we summarise the results of the GPE in spatially infinite systems, and state how our results on the finite-sized CHM apply to the GPE.

3.A.1 Review of the GPE in an infinite-sized domain

The Gross-Pitaevskii equation [93, 94],

$$i\frac{\partial\psi}{\partial t} + \nabla^2\psi + s|\psi|^2\psi = 0, \quad (3.23)$$

is a classical model used to study condensation in Bose gases [78], and also in light propagating in a dispersive medium with a local Kerr nonlinearity [19] (in the optical case the dimensionality $d < 3$). In the Bose gas case $\psi(\mathbf{x}, t)$ is the boson wavefunction, and in the optical case it represents the modulating envelope of the input beam. We consider the defocusing GPE with $s = -1$, in which case condensates are stable.

Proceeding as in section 3.3.1, we work in Fourier space and define the waveaction spectrum $n_{\mathbf{k}} = (\frac{L}{2\pi})^d \langle |\psi_{\mathbf{k}}|^2 \rangle$. We make the standard WT assumptions, which allow us to derive a four-wave kinetic equation, describing the evolution of $n_{\mathbf{k}}$ for small-amplitude waves with dispersion relation $\omega_{\mathbf{k}} = k^2$ fluctuating over a zero background [19]:

$$\partial_t n_{\mathbf{k}} = 4\pi \int n_1 n_2 n_3 n_{\mathbf{k}} \left[\frac{1}{n_{\mathbf{k}}} + \frac{1}{n_3} - \frac{1}{n_1} - \frac{1}{n_2} \right] \delta_{3\mathbf{k}}^{12} \delta(\omega_{3\mathbf{k}}^{12}) d\mathbf{k}_1 d\mathbf{k}_2 d\mathbf{k}_3,$$

where $\delta_{3\mathbf{k}}^{12} = \delta(\mathbf{k}_1 + \mathbf{k}_2 - \mathbf{k}_3 - \mathbf{k})$ and $\delta(\omega_{3\mathbf{k}}^{12}) = \delta(\omega_1 + \omega_2 - \omega_3 - \omega_{\mathbf{k}})$.

This kinetic equation preserves \mathcal{N} , the total waveaction, or number of particles in the boson case, and the linear energy \mathcal{E} ,

$$\mathcal{N} = \int n_{\mathbf{k}} d\mathbf{k} \quad \text{and} \quad \mathcal{E} = \int \omega_{\mathbf{k}} n_{\mathbf{k}} d\mathbf{k}, \quad (3.24)$$

and has a class of stationary solution that are the equilibrium RJ spectra

$$n_{\mathbf{k}}^{\text{RJ}} = \frac{T}{\omega_{\mathbf{k}} + \mu} \quad (3.25)$$

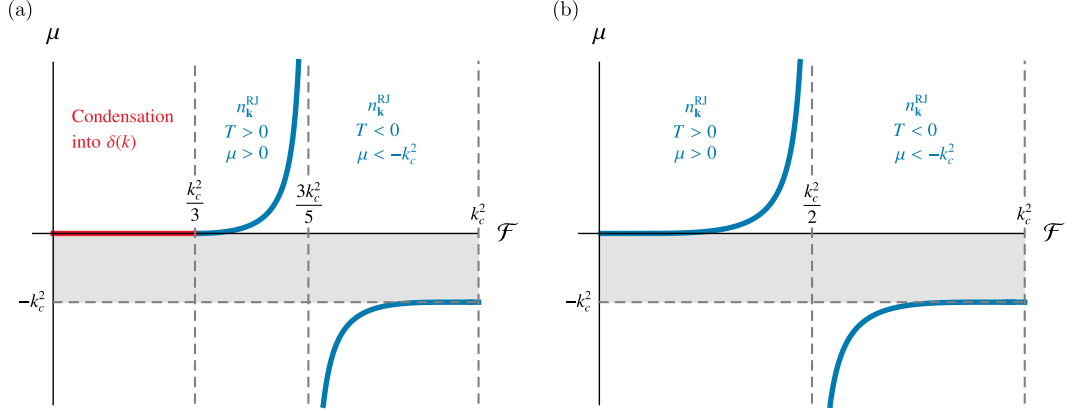


Figure 3.8: Chemical potential μ as a function of the energy per particle $\mathcal{F} = \mathcal{E}/\mathcal{N}$ for an infinite-sized GPE system with high-wavenumber cutoff at $|\mathbf{k}| = k_c$, in (a) 3D, and (b) 2D. For both dimensionalities the RJ spectrum has a positive and a negative (T, μ) branch. Condensation into a singular spectrum happens in 3D but not in 2D.

where T is the temperature and μ is the chemical potential.

On the RJ spectrum (3.25) the invariant $\sigma = (\mathcal{E} + \mu\mathcal{N})/T$ is partitioned equally across all Fourier modes. Again this leads to the ultraviolet catastrophe if Fourier space is unbounded. In [20] this is regularised by introducing a radial cutoff k_c to the \mathbf{k} -space integrals in (3.24). This hard cutoff is more physically motivated in [3] for the case of particles obeying Bose-Einstein statistics, with distribution $n_{\mathbf{k}} = (\exp[(k^2 + \mu)/T] - 1)^{-1}$. The RJ spectrum (3.25) is the low- k limit of the Bose-Einstein distribution, whereas at high k the distribution becomes a Gaussian cutoff $n_{\mathbf{k}} \sim \exp(-k^2/T)$. Whether hard or exponential, the ultraviolet cutoff arrests the runaway excitation of high wavenumbers during thermalisation, allowing (3.25) to become a nontrivial stationary spectrum.

For spatially infinite domains there is no low- k cutoff, and (3.24) remain as continuous integrals.

3.A.2 RJ spectra and Bose-Einstein condensation in 3D.

We consider a 3D system initialised with some amount of waveaction and energy, and evolving to an equilibrium state. If this equilibrium can be described by (3.25) then μ and T will be defined in terms of the initial \mathcal{N} and \mathcal{E} , which in the spatially infinite system with a \mathbf{k} -space cutoff at k_c are

$$\mathcal{N} = 4\pi T \int_0^{k_c} \frac{k^2}{k^2 + \mu} dk \quad \mathcal{E} = 4\pi T \int_0^{k_c} \frac{k^4}{k^2 + \mu} dk.$$

These integrals can be evaluated explicitly, see [20] for their closed-form expression. For $\mu > 0$ at fixed $T > 0$, both \mathcal{N} and \mathcal{E} monotonically decrease with μ . At $\mu = 0$

both integrands vary as k^α with $\alpha \geq 0$, so both \mathcal{N} and \mathcal{E} converge at the lower limit in 3D. Thus for every $T > 0$ the values of $(\mathcal{N}, \mathcal{E})$ that can be accommodated in the RJ spectrum are bounded from above by their value at $\mu = 0$.

We define the energy per particle

$$\mathcal{F}(\mu) = \frac{\mathcal{E}}{\mathcal{N}},$$

which is independent of T , and can be considered a control parameter in numerical simulations by choosing the initial spectrum appropriately. Following [95] we plot the μ that characterises the equilibrium spectrum as a function of the initial \mathcal{F} , see figure 3.8(a).

As $\mu \rightarrow 0^+$, \mathcal{N} and \mathcal{E} increase to their local maxima while their ratio decreases to a critical value $\mathcal{F}(0)$, which in the case of a radial cutoff equals $k_c^2/3$. Systems initialised with $\mathcal{F} < \mathcal{F}(0)$ (red region in figure 3.8(a)) cannot be accommodated by the RJ spectrum. Einstein's argument [77] is that once $n_{\mathbf{k}}^{\text{RJ}}$ reaches its capacity at $\mu = 0$ any extra particles are absorbed into the zero-energy state, i.e. into a singular distribution at $\mathbf{k} = 0$. This is the true Bose-Einstein condensate, and can exist at nonzero temperature.

At the critical value $\mathcal{F} = 0$ for condensation, $\mu = 0$ and the RJ spectrum represents equipartition of \mathcal{E} . Above the condensation threshold, systems initialised with $k_c^2/3 < \mathcal{F} < 3k_c^2/5$ equilibrate to an RJ spectrum with no condensate, and positive (μ, T) .

As $\mathcal{F} \rightarrow (3k_c^2/5)^{\mp}$ we have $\mu \rightarrow \pm\infty$. For finite $(\mathcal{N}, \mathcal{E})$ this means that $T \rightarrow \pm\infty$, and the RJ spectrum is one of equipartition of \mathcal{N} .

For $\mathcal{F} > 3k_c^2/5$ physical RJ solutions exist with $T < 0$ and $-\infty < \mu < -k_c^2$, in the sense that $n_{\mathbf{k}}^{\text{RJ}} > 0$ for all $\mathbf{k} : 0 \leq k \leq k_c$. These negative temperature RJ states are characterised by $n_{\mathbf{k}}$ rising with k , becoming increasingly peaked as μ increases from $-\infty$. As $\mu \rightarrow (-k_c^2)^-$ and $\mathcal{F} \rightarrow k_c^2$ we must have $T \rightarrow 0^-$ so as to keep $(\mathcal{N}, \mathcal{E})$ finite. Eventually the RJ spectrum becomes singular $n_{\mathbf{k}}^{\text{RJ}} \rightarrow \mathcal{N}\delta(k-k_c)/4\pi k^2$. As this limit is approached, \mathcal{E} and \mathcal{N} get increasingly concentrated into spherical shells of decreasing thickness $|k_c - k| \rightarrow 0$ (with the \mathcal{E} shell being thicker than the \mathcal{N} shell). This is condensation in the sense that we defined in section 3.3.2.2, extended to continuous \mathbf{k} -space, i.e. macroscopic occupation of the invariants in a set of Fourier modes whose measure vanishes in the limit.

For $-k_c^2 < \mu < 0$, in between the positive and negative (μ, T) branches of $n_{\mathbf{k}}^{\text{RJ}}$, there exists a gap in which no physical RJ solution is possible. This gap is shaded grey in figure 3.8.

To summarise: in 3D, for all initial $(\mathcal{N}, \mathcal{E})$ that are physically realisable, the GPE dynamics drive the system to equilibria that consist of either a condensate with some RJ component, an RJ spectrum with (μ, T) positive, or an RJ distribution

with (μ, T) negative.

3.A.3 RJ spectra in 2D with no true Bose-Einstein condensation

For an infinite system in 2D with an isotropic cutoff at high wavenumber, the wave-action and energy on an RJ spectrum are

$$\mathcal{N} = 2\pi T \int_0^{k_c} \frac{k}{k^2 + \mu} dk \quad \mathcal{E} = 2\pi T \int_0^{k_c} \frac{k^3}{k^2 + \mu} dk.$$

Again for $T > 0$ both \mathcal{N} and \mathcal{E} are maximised as $\mu = 0$, when the integrands become k^{-1} and k respectively. The integral for \mathcal{E} converges, indicating a finite capacity for the RJ spectrum to absorb energy at positive temperature. However the \mathcal{N} integral diverges logarithmically at the lower limit, indicating that the RJ spectrum can accommodate an arbitrarily large number of particles. In order to fit this large \mathcal{N} into the RJ spectrum, while keeping \mathcal{E} constant we must have $T \rightarrow 0^+$ as $\mu \rightarrow 0^+$: in an infinite 2D system there is no true Bose-Einstein condensation of particles at finite temperature [79, 80].

This is reflected in the μ vs. \mathcal{F} plot in figure 3.8(b). We have $\mu \rightarrow 0^+$ as $\mathcal{F} \rightarrow 0^+$, with no condensation (and the spectrum at $\mu = 0$ representing equipartition of \mathcal{E}). In the range $0 < \mathcal{F} < k_c^2/2$, the RJ spectrum has $(\mu, T) > 0$. In $k_c^2/2 < \mathcal{F} < k_c^2$ the RJ spectrum has $T < 0$ and $-\infty < \mu < -k_c^2$; for such a spectrum $n_{\mathbf{k}}^{\text{RJ}}$ increases with k .

As $\mathcal{F} \rightarrow (k_c^2/2)^{\mp}$ both $(\mu, T) \rightarrow \pm\infty$, and \mathcal{N} is partitioned equally amongst wave modes. As $\mathcal{F} \rightarrow (k_c^2)^-$ and $\mu \rightarrow (-k_c^2)^-$ the spectrum reaches a singular limit, $n_{\mathbf{k}}^{\text{RJ}} \rightarrow \mathcal{N}\delta(k - k_c)/2\pi k$ with $T \rightarrow 0^-$ to keep the invariants finite. The density of \mathcal{E} dominates that of \mathcal{N} for such a spectrum. Again this is condensation in the sense of section 3.3.2.2, extended to continuous integrals.

3.A.4 The 2D GPE in a finite domain

We now turn to the GPE in a finite domain in 2D. We consider a system with the same setup as we used for the CHM equation in section 3.3.2.2, with a high-wavenumber cutoff at k_{max} and low-wavenumber cutoff at k_{min} in both the k_x and k_y directions, the variables rescaled to k_{max} as in (3.11), and the integrals for in (3.24) replaced by sums over the \mathbf{k} -space lattice L_ϵ . We calculate \mathcal{N} and \mathcal{E} numerically to find $\mathcal{F}(\mu) = \mathcal{E}/\mathcal{N}$, and plot μ vs. \mathcal{F} in figure 3.9(a).

Once again we observe that the RJ spectrum has a positive T branch and a negative (μ, T) branch, which are characterised by the spectrum falling or rising with k respectively. Between the two branches $\mu \rightarrow \pm\infty$ as \mathcal{F} approaches the limiting value $\mathcal{F}(\pm\infty)$ from below or above. Summing over the lattice L_ϵ we find

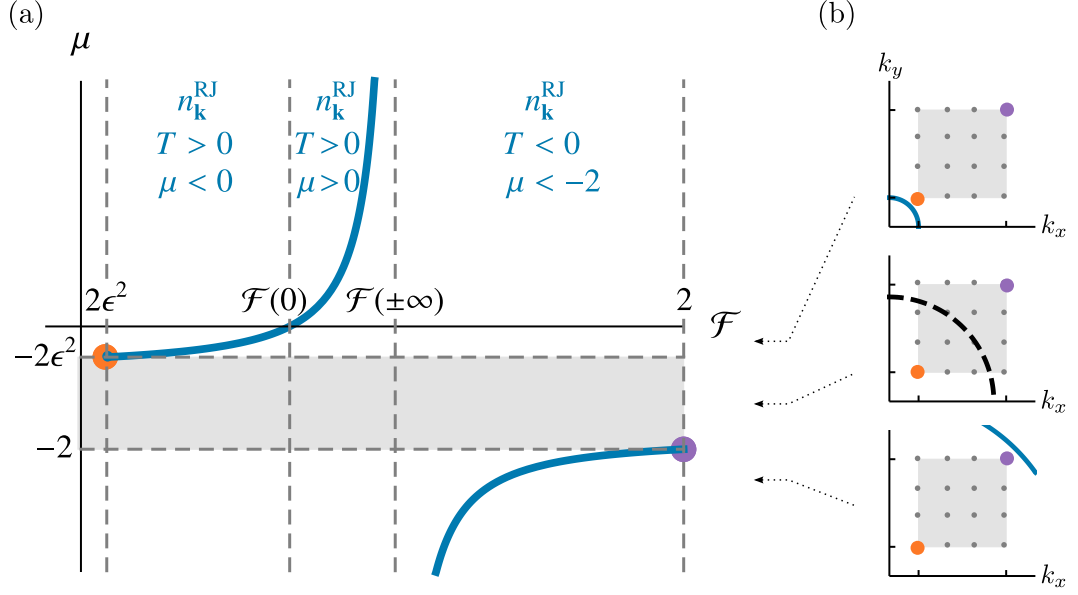


Figure 3.9: (a) Chemical potential μ vs. energy per particle $\mathcal{F} = \mathcal{E}/\mathcal{N}$ for a 2D GPE system of finite size, with high and low wavenumber cutoffs in k_x and k_y . The introduction of a finite box size induces a portion of $\mu < 0$ on the $T > 0$ branch of the RJ spectrum. (b) The curve of $D = 0$ moving through the k_x - k_y plane as μ swings from the $\mu < 0, T > 0$ branch of $n_{\mathbf{k}}^{\text{RJ}}$ (top panel), into the RJ-forbidden region (middle), and onto the $T < 0, \mu < -2$ branch of $n_{\mathbf{k}}^{\text{RJ}}$ (bottom).

$\mathcal{F}(\pm\infty) = (2 + 3\epsilon + \epsilon^2)/3$. As in the infinite-size case, this limit corresponds to equipartition of \mathcal{N} with $T \rightarrow \pm\infty$.

On the positive T branch of $n_{\mathbf{k}}^{\text{RJ}}$, we see that the introduction of the box size pushes the curve downwards in figure 3.9(a), so that there is now a $\mu < 0, T > 0$ part of the branch and a $(\mu, T) > 0$ part. The $\mu < 0$ part terminates as $\mathcal{F} \rightarrow 2\epsilon^2$, with $\mu \rightarrow \mu^+ = -2\epsilon^2$ and $T \rightarrow 0$, with all limits approached from above. In this limit the spectrum becomes a Kronecker delta at the gravest mode $\mathbf{k}^+ = (\epsilon, \epsilon)$, signified by the orange dot in figure 3.9. This is the condensate, as defined in section 3.2.1. Here the waveaction density dominates over the energy density, so as this limit is approached \mathcal{N} condenses first, with condensation of \mathcal{E} following. This is exactly like the condensation of Z in the CHM equation, except that in the GPE the absence of the third invariant leaves room for \mathcal{N} to dominate in the entire sector $k \ll 1$.

The negative T branch terminates at $\mathcal{F} = 2$ when the whole spectrum is concentrated at the smallest-scale mode $\mathbf{k}_- = (1, 1)$, signified by the purple dot. In this sector the energy density dominates over the waveaction density, so this limit represents condensation of primarily \mathcal{E} , and then finally \mathcal{N} in the limit, as $\mu \rightarrow \mu^- = -2$ and $T \rightarrow 0$ from below (c.f. the condensation of Ω in the CHM equation).

In figure 3.9(b) we show the k_x - k_y plane and how the curve $D = 0$ changes

(where $D(\mathbf{k}, \mu)$ is the denominator of (3.25)) as μ is swung from the $T > 0$ branch with $\mu^+ < \mu < 0$ (top panel), to inside the RJ-forbidden range $\mu^+ > \mu > \mu_-$ (middle panel), to the $T < 0$, $\mu < \mu^-$ branch (bottom panel). We see that in the RJ-forbidden range of μ (grey region in figures 3.8 and 3.9(b)), the $D = 0$ line enters S_ϵ , and “captures” modes of L_ϵ , reversing the sign of the spectrum on these modes. Only when $D = 0$ has captured all of L_ϵ does the spectrum become sign-definite again, on the $(\mu, T) < 0$ branch.

Chapter 4

Wave turbulence in self-gravitating Bose gases and nonlocal nonlinear optics

4.1 Chapter summary

In this chapter we develop the theory of weak wave turbulence in systems described by the Schrödinger-Helmholtz equations in two and three dimensions. This model contains as limits both the familiar cubic nonlinear Schrödinger equation, and the Schrödinger-Newton equations. The latter, in three dimensions, are a nonrelativistic model of fuzzy dark matter which has a nonlocal gravitational self-potential, and in two dimensions they describe nonlocal nonlinear optics in the paraxial approximation. We show that in the weakly nonlinear limit the Schrödinger-Helmholtz equations have a simultaneous inverse cascade of particles and a forward cascade of energy. We interpret the inverse cascade as a nonequilibrium condensation process, which is a precursor to structure formation at large scales (for example the formation of galactic dark matter haloes or optical solitons). We show that for the Schrödinger-Newton equations in two and three dimensions, and in the two-dimensional nonlinear Schrödinger equation, the particle and energy fluxes are carried by small deviations from thermodynamic distributions, rather than the Kolmogorov-Zakharov cascades that are familiar in wave turbulence. We develop a differential approximation model to characterise such “warm cascade” states.

Note that in this chapter, we refer to the Gross-Pitaevskii equation (2.3) by its alias, the (cubic, local) nonlinear Schrödinger equation, in order to highlight its kinship to the Schrödinger-Helmholtz equations.

4.2 Introduction

4.2.1 Wave turbulence cascades

The dynamical and statistical behaviour of random weakly-interacting waves is responsible for many important physical effects across applications ranging from quantum to classical and to astrophysical scales [4, 3]. Assuming weak nonlinearity and random phases, such behaviour is described by the theory of weak wave turbulence [4, 3]. As in the theory of classical hydrodynamic turbulence, weak wave turbulence theory can predict nonequilibrium statistical states characterised by cascades of energy and/or other invariants through scales. Sometimes, similarly to 2D classical turbulence, such cascades are dual, with one invariant cascading to small scales (direct cascade) and the other invariant towards large scales (inverse cascade). An inverse cascade often leads to accumulation of the turbulence spectrum near the largest scale of the system, which is analogous to Bose-Einstein condensation. Large-scale coherent structures may form out of such a condensate and further evolve via mutual interactions and interactions with the background of random waves, thereby realising a scenario of order emerging from chaos.

In the present chapter, we will study a precursor to such a process of coherent structure formation by developing the wave turbulence theory and describing the dual cascade in the so-called “Schrödinger-Helmholtz equations” that arise in cosmological and nonlinear optics applications.

4.2.2 Schrödinger-Helmholtz equations

The Schrödinger-Helmholtz equations are the nonlinear partial differential equations

$$i\partial_t\psi + \nabla^2\psi - V[|\psi|^2]\psi = 0, \quad (4.1a)$$

$$\nabla^2V - \Lambda V = \gamma|\psi|^2 \quad (4.1b)$$

for a complex scalar field $\psi(\mathbf{x}, t)$ in which $V[|\psi|^2]$ plays the role an interaction potential and Λ and γ are constants. We will be interested in systems set in three and two spatial dimensions (3D and 2D, respectively).

Before proceeding in the body of this chapter with developing the statistical description of the nonlinear field ψ in the framework of Eqs. (4.1), we will first outline in this Sec. 4.2.2 the important physical contexts in which Eqs. (4.1) have been used, the previous results found, and the findings that we anticipate will arise from our approach.

Notice that depending on the spatial scale of interest ℓ , one term or the other on the left-hand side of Eq. (4.1b) is dominant. For $\ell \gg \ell_* = 1/\sqrt{\Lambda}$ the

Schrödinger-Helmholtz equations (4.1) become the more familiar cubic nonlinear Schrödinger equation, discussed in Sec. 4.2.2.1, while for $\ell \ll \ell_*$ they turn into the Schrödinger-Newton equations, see Sec. 4.2.2.2. Finally, in Sec. 4.2.2.3 we return to interpret the Schrödinger-Helmholtz Eqs. (4.1) in light of the discussion of these limits.

4.2.2.1 Large-scale limit: The nonlinear Schrödinger equation

In the limit of large scales, $\ell \gg \ell_*$, the first term on the left-hand side of Eq. (4.1b) can be neglected and one immediately finds that $V[|\psi|^2] = -(\gamma/\Lambda)|\psi|^2$. The constant γ/Λ can be removed by proper renormalization of $|\psi|^2$, leaving only the sign of this constant, denoted as $s = \pm 1$. Thus the Schrödinger-Helmholtz Eqs. (4.1) become the nonlinear Schrödinger equation

$$i\partial_t\psi + \nabla^2\psi + s|\psi|^2\psi = 0, \quad (4.2)$$

also known as the Gross-Pitaevskii equation [78]. This equation has a cubic, spatially local, attractive (for $s = +1$) or repulsive (for $s = -1$) interaction.

The nonlinear Schrödinger Eq. (4.2) is well known in the study of Bose-Einstein condensates [78], where ψ is the wavefunction of a system of identical bosons in the Hartree-Fock approximation [93, 94] and the nonlinearity is due to s -wave scattering. (As well as normalising the coupling constant s to ± 1 , units are further chosen such that the reduced Planck constant $\hbar = 1$ and the boson mass $m = 1/2$.)

Equation (4.2) is also familiar in the field of nonlinear optics [96, 97] when a light beam, whose electric field is slowly modulated by an envelope ψ (such that its intensity is $|\psi|^2$), impinges on a dispersive, nonlinear medium, inducing a nonlinear change in the medium's refractive index via the Kerr effect. Equation (4.2) then describes the evolution of the beam's envelope in the paraxial approximation, where t becomes the length along the beam axis, and the remaining spatial directions are transverse to the beam. (In the optics application units are chosen such that $k_0 n_0 = 1/2$ where k_0 is the free space wavenumber of the input beam and n_0 is the refractive index of the medium, normalising the coefficient of the Laplacian term to unity.)

In this context s is the normalised Kerr coefficient, and the cases with $s = +1$ or -1 are known as the focusing or defocusing nonlinear Schrödinger equation respectively, terminology that we adopt here in the general case.

The nonlinear Schrödinger Eq. (4.2) is studied in a great many other systems due to its universality in describing the slowly-varying envelope of a monochromatic wave in a weakly nonlinear medium [98]. We shall not pursue its other applications

in this work, instead merely noting that due to its universality many monographs and papers have been dedicated to the study of Eq. (4.2) and its solutions.

4.2.2.2 Small-scale limit: The Schrödinger-Newton equations

Now we focus on scales $\ell \ll \ell_*$, when the second term in the left-hand side of Eq. (4.1b) dominates. Then the Schrödinger-Helmholtz Eqs. (4.1) simplify to the coupled equations

$$i\partial_t\psi + \nabla^2\psi - V[|\psi|^2]\psi = 0, \quad (4.3a)$$

$$\nabla^2 V = \gamma|\psi|^2. \quad (4.3b)$$

In three dimensions if we retain the interpretation of $\psi(\mathbf{x}, t)$ as a boson wavefunction, we see that the nonlinearity in Eq. (4.3a) is nonlocal, coming from an extended potential $V[|\psi|^2]$ that solves the Poisson Eq. (4.3b) for which the source is proportional to the boson number density $\rho = |\psi|^2$. Specifying $\gamma = \pi$, and noting that we have chosen units in which $\hbar = 1$, $m = 1/2$, and Newton’s gravitational constant $G = 1$, we observe that Eqs. (4.3) describe a dilute Bose gas moving at nonrelativistic speeds under the influence of a Newtonian gravitational potential generated by the bosons themselves. It is for this reason that Eqs. (4.3) are known as the Schrödinger-Newton equations. (The derivation of Eqs. (4.3) from a Klein-Gordon action with a general relativistic metric can be found in the literature, for example [99, 100].)

The use of Eqs. (4.3) to represent self-gravitating Bose gases in the Newtonian limit is important in cosmology, where they are used to model “fuzzy dark matter”. This is the hypothesis that dark matter is comprised of ultra-light ($m \lesssim 1 \times 10^{-22}$ eV) scalar bosons whose de Broglie wavelengths are on the order of galaxies ($\lambda_{\text{dB}} \sim 1$ kpc) [101–103, 99, 104, 105]. In this scenario galactic dark matter haloes are gigantic condensates of this fundamental boson, trapped by their own gravity and supported by quantum pressure arising from the uncertainty principle [101, 106, 107, 103, 108, 109, 100], as illustrated in figure 4.1.

Fuzzy dark matter is an alternative to the standard model of cosmology which supposes that dark matter is comprised of thermal but sub-luminal, weakly interacting massive particles, i.e., “cold dark matter” [111]. While cold dark matter is successful at describing the observed large-scale structure of the universe, its accelerated expansion, and the fluctuations of the cosmic microwave background [112, 113], at small scales it fails to reconcile observations with cosmological simulations, particularly in matching the inferred flat density profiles of galactic dark matter haloes with the cuspy profiles found in simulations, and the lack of observed satellite dwarf galaxies as compared to theoretical predictions [114, 115]. By contrast, in fuzzy dark matter galactic cores arise naturally as compact soliton-like structures with

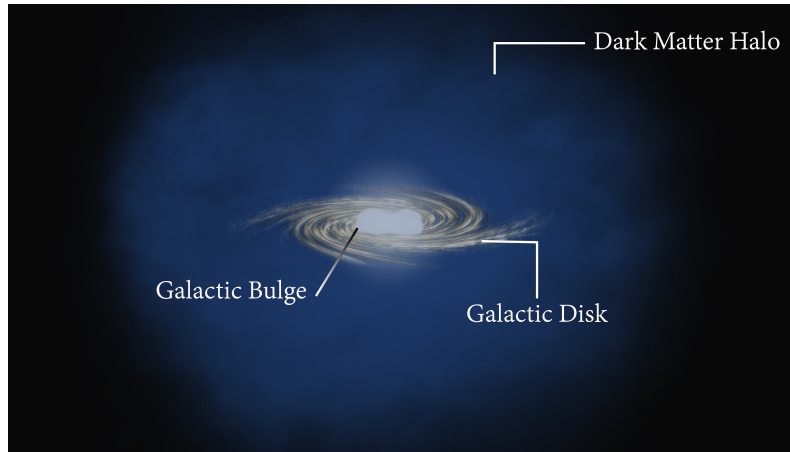


Figure 4.1: Schematic sketch of a spiral galaxy, embedded in a dark matter halo [110]. In the fuzzy dark matter model, such a halo consists of a solitonic condensate of a self-gravitating scalar boson field that can be described by the Newtonian limit of the Schrödinger-Helmholtz equations.

core radii on the order of λ_{dB} , below which fine structure is suppressed by the uncertainty principle [116, 117] and, when included in the model, *s*-wave scattering [103, 107, 118], providing a resolution to the small-scale problems of cold dark matter. At large scales the two models become indistinguishable [108]. Thus, until the precise nature of dark matter particles is identified, fuzzy dark matter must be considered alongside cold dark matter when investigating the formation of large-scale structure in the early universe [108, 119–121].

Like the nonlinear Schrödinger Eq. (4.2), the Schrödinger-Newton Eqs. (4.3) also have applications in nonlinear optics. Here (4.3a) is again the equation for the envelope of the beam in two transverse spatial dimensions and the distance along the beam is again the time-like dimension. $V[|\psi|^2]$ is now the change in refractive index of the optical sample induced by the incident beam, whose nonlocality is expressed in Eq. (4.3b). This can be due to the refractive index being temperature-dependent and (4.3b) describing the diffusion of the incident beam energy through the medium as heat: the thermo-optic effect [97, 122]. Alternatively, in nematic liquid crystals the refractive index depends on the orientation of the liquid crystal molecules with respect to the wavevector of the incident beam, and (4.3b) describes the reorientation induced by the electric (or magnetic) field of the beam, which diffuses through the sample due to long-range elastic interactions between the molecules [123]. Indeed, 1D optical wave turbulence experiments using liquid crystals have already been carried out, and modelled theoretically by the Schrödinger-Helmholtz equations, including in its Newtonian limit [21, 22]; results from the latter reference are reproduced for illustration in figure 4.2.

Nonlocal nonlinear optics manifest many phenomena that are the nonlocal

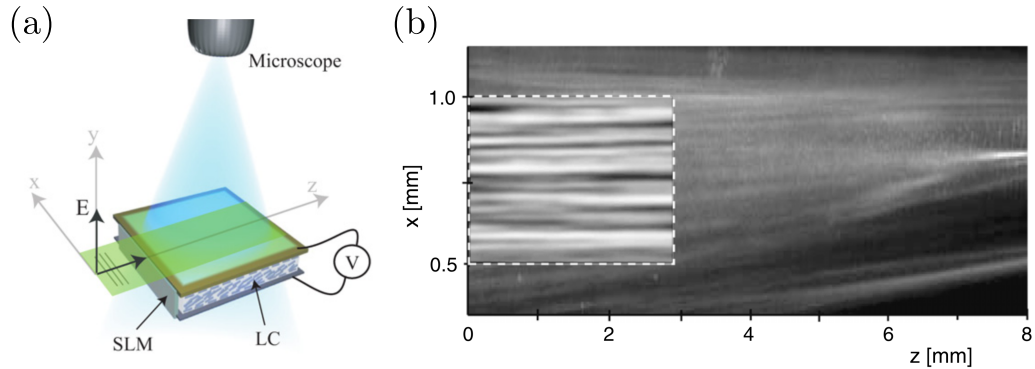


Figure 4.2: An optical wave turbulence experiment using liquid crystal as the non-local nonlinear medium [22]. The experimental setup is shown in (a). Results of numerical modelling of the system using the Schrödinger-Helmholtz equations is shown in (b). Note that the dynamics in this system occurred in one spatial direction, the x direction, and the z direction is analogous to time. In this chapter we carry out theoretical analysis of the wave turbulence of analogous optical systems in 2D.

versions of the equivalent local phenomenon, for example (but by no means limited to) solitons [124, 122, 125, 126], soliton interactions [127], modulational instability and collapse [128–130], and shocks and shock turbulence [131, 132]. In addition, comparisons can be made between nonlinear optical systems and fuzzy dark matter by virtue of Eqs. (4.3) describing them both. Indeed recent optics experiments [133, 134], and theoretical works [135, 136] have drawn direct analogies between optical systems that can be realised in the laboratory and astrophysical systems on the scale of galaxies.

4.2.2.3 Physical applications of the Schrödinger-Helmholtz equations

The Schrödinger-Helmholtz Eqs. (4.1), then, are a model that captures the physics present in both Eq. (4.2) and Eqs. (4.3). Applied to fuzzy dark matter the diffusive term in Eq. (4.1b) represents gravity in the Newtonian approximation of the Einstein field equations, as per Sec. 4.2.2.2, while the local term corresponds to the inclusion of a cosmological constant Λ in this approximation [137]. This is necessary if one wants to account for a dark energy component to cosmology in a Newtonian approximation. It is also a means to regularise the so-called “Jeans swindle”—the specification that Eq. (4.3b) only relates the fluctuations of density and potential around an unspecified equilibrium [138], see Appendix 4.A to this chapter.

In the optical context Eqs. (4.1) model a system where both Kerr (local) effects and thermo-optic or elastic (diffusive nonlocal) effects are important (alternatively, the diffusive term in Eq. (4.1b) can be used to take account of heat losses at the edges of the optical sample [131, 133]).

We therefore take the Schrödinger-Helmholtz Eqs. (4.1), as our model of interest as they comprise a model that is physically relevant in both astrophysics and nonlinear optics, depending on the choice of dimensionality and units. They contain as limits both the nonlinear Schrödinger equation, about which much is known, and the Schrödinger-Newton equations, whose relevance is starting to come to the fore. Next we discuss weak and strong turbulence in these latter models, and introduce the process of dual cascade of invariants, which is a precursor to the formation of structures at the largest scale in Schrödinger-Helmholtz systems.

4.2.3 Turbulence in the nonlinear Schrödinger and Schrödinger-Newton equations

Turbulence in laboratory Bose-Einstein condensates [139–145] and optics [22, 19, 146] is now a well-established field, and much has been understood by using the local nonlinear Schrödinger Eq. (4.2). Its dynamics is rich, with weakly nonlinear waves typically coexisting with coherent, strongly nonlinear structures. The nature of these structures depends radically on the sign of the interaction term s in Eq. (4.2). In the defocusing (repulsive) case they include stable condensates: accumulations of particles (in the Bose-Einstein condensate case) or intensity (optics) at the largest scale, with turbulence manifesting as a collection of vortices in 2D, or a tangle of vortex lines in 3D, on which the density is zero and which carry all the circulation, propagating through the condensate [143, 144, 3]. In the focusing (attractive) case solitons and condensates are unstable above a certain density, with localised regions of over-density collapsing and becoming singular in finite time [19, 147].

On the other hand, turbulence in the Schrödinger-Newton Eqs. (4.3) has only recently been investigated by direct numerical simulation in the cosmological setting [119] and appears to contain features of both the focusing and the defocusing nonlinear Schrödinger equation. As mentioned above, at large scales the Schrödinger-Newton model exhibits gravitationally-driven accretion into filaments which then become unstable and collapse into spherical haloes [120, 121] (cf. collapses in the focusing nonlinear Schrödinger model driven by the self-focusing local contact potential). However, within haloes the condensate is stable, with turbulence in an envelope surrounding the core manifesting as a dynamic tangle of reconnecting vortex lines, as in the defocusing nonlinear Schrödinger model [119]. This is to be expected, given that the attractive feature of the Schrödinger-Newton model in cosmology is that it is simultaneously unstable to gravitational collapse and stable once those collapse event have regularised into long-lived structures, and so it should contain features of both the unstable (focusing) and stable (defocusing) versions of the nonlinear Schrödinger model.

To understand more fully the phenomenology recently reported in the Schrödinger-

Newton Eqs. (4.3), it is tempting to apply theoretical frameworks that have been successful in explaining various aspects of turbulence in the nonlinear Schrödinger equation. One such theory is wave turbulence: the study of random broadband statistical ensembles of weakly interacting waves [3, 4]. The “turbulent” behaviour referred to here is the statistically steady-state condition where dynamically conserved quantities cascade through scales in the system via the interaction of waves, a process analogous to the transfer of energy in 3D classical fluid turbulence (and respectively energy and enstrophy in 2D). Wave turbulence theory is integral to the quantitative description of both the wave component and the evolution of the coherent components of the nonlinear Schrödinger system and is relevant in three regimes: de Broglie waves propagating in the absence of a condensate [19, 3], Bogoliubov acoustic waves on the background of a strong condensate [19, 3], and Kelvin waves that are excited on quantized vortex lines in a condensate [3, 18]. If the system is focusing, then the condensate is modulationally unstable and vortices do not appear, so acoustic and Kelvin wave turbulence will not be realised [the gravitational-type nonlinearity present in Eqs. (4.3) is of focusing type and so this is the situation that is most relevant to this chapter]. Nonetheless, in both focusing and defocusing systems de Broglie wave turbulence theory describes how, starting from a random ensemble of waves, a dual cascade simultaneously builds up the large-scale condensate while sending energy to small scales [3]. As we will describe in Sec. 4.3.3 below, this dual cascade is generic in any system of interacting waves with two quadratic dynamical invariants (particles and energy in the cases of interest here). The theory of wave turbulence thus provides a universal description of how large-scale coherent structures can arise from a random background.

As mentioned above, the wave turbulence of Eqs. (4.1), the fundamental process of dual cascade, and the spectra on which such cascades can occur, have already been investigated theoretically and in optics experiments in the one-dimensional case [21, 22] in the large-scale and small-scale limits where the dynamical equations become Eq. (4.2) and Eqs. (4.3) respectively. To our knowledge such a study of the wave turbulence of (4.1) has not been made in higher dimensions. We begin this study in the current work.

Having said this, we note that Ref. [146] refers to the “optical wave turbulence” of nonlocal systems, of which the Schrödinger-Helmholtz equations are an important example. Much of Ref. [146], and references therein, pertains to the dynamics of inhomogeneous systems (such as modulational instability and collapse, studied by a Vlasov equation). By contrast here we are concerned with the dynamics that govern statistically homogeneous systems. We comment on the difference in approaches to inhomogeneous vs. homogeneous systems in Appendix 4.B. Furthermore, a recent paper [148] has examined the formation of large-scale structure in

astrophysical Bose gases obeying Eqs. (4.3), using a kinetic formulation which was termed “wave turbulence” in Ref. [100]. We describe the similarities and differences between Ref. [148] and this work in Sec. 4.5.1.

4.2.4 Organisation of this chapter

In this chapter, then, we develop the theory of wave turbulence for the Schrödinger-Helmholtz Eqs. (4.1) in the case of fluctuations about a zero background. By taking the limits of small and large Λ we obtain the wave turbulence of the Schrödinger-Newton Eqs. (4.3) and also review known results of the nonlinear Schrödinger Eq. (4.2). Our aim is to describe the fundamental dynamical processes that govern the first stages of formation of a large-scale condensate from random waves in cosmology and in nonlinear optics. From this structure gravitational-type collapses will ensue and the phenomenology described above will develop.

In Secs. 4.3.1 and 4.3.2 we overview the wave turbulence theory and arrive at the wave kinetic equation that describes the evolution of the wave content of the system. Section 4.3.3 describes the dual cascade of energy towards small scales and particles towards large scales in the system. In Secs. 4.3.4 and 4.3.5 we describe respectively the scale-free pure-flux spectra and equilibrium spectra that are formal stationary solutions of the wave kinetic equation. However in Sec. 4.3.6 we show that these stationary spectra yield the wrong directions for the fluxes of energy and particles, as compared with the directions predicted in Sec. 4.3.3. We resolve this paradox by developing a reduced model of the wave dynamics in Secs. 4.3.7 and 4.3.8 and using it in Sec. 4.4 to reveal the nature of the dual cascades in the nonlinear Schrödinger and the Schrödinger-Newton limits of the Schrödinger-Helmholtz equations. We conclude in Sec. 4.5 and suggest further directions of research incorporating wave turbulence into the study of the Schrödinger-Helmholtz equations.

4.3 Building blocks of Schrödinger-Helmholtz wave turbulence

In this section we overview the aspects of the wave turbulence theory that we require in our description of turbulence in the Schrödinger-Helmholtz model.

4.3.1 Hamiltonian formulation of the Schrödinger-Helmholtz equations

To put Schrödinger-Helmholtz turbulence in the context of the general theory of wave turbulence we need to formulate the Schrödinger-Helmholtz Eqs. (4.1) in Hamil-

tonian form. For that goal we first set the system in the periodic box $\Omega = \mathbb{T}_L^d$ and decompose variables into Fourier modes

$$\psi_{\mathbf{k}}(t) = \frac{1}{L^d} \int_{\Omega} \psi(\mathbf{x}, t) e^{-i\mathbf{k}\cdot\mathbf{x}} d\mathbf{x},$$

and similarly for $V_{\mathbf{k}}(t)$. The dynamical equations become

$$i\partial_t \psi_{\mathbf{k}} - k^2 \psi_{\mathbf{k}} - \sum_{1,2} V_1 \psi_2 \delta_{12}^{\mathbf{k}} = 0, \quad (4.4a)$$

$$-(k_1^2 + \Lambda) V_1 = \gamma \sum_{3,4} \psi_3 \psi_4^* \delta_{14}^3, \quad (4.4b)$$

where $V_j = V_{\mathbf{k}_j}$, $\psi_j = \psi_{\mathbf{k}_j}$, $\sum_{i\dots j} = \sum_{\mathbf{k}_i, \dots, \mathbf{k}_j}$ and $\delta_{12}^{\mathbf{k}} = \delta(\mathbf{k} - \mathbf{k}_1 - \mathbf{k}_2)$ is the Kronecker delta, equal to unity if $\mathbf{k} = \mathbf{k}_1 + \mathbf{k}_2$ and zero otherwise.¹

Equations (4.4) can be rewritten as the canonical Hamiltonian equation

$$i\partial_t \psi_{\mathbf{k}} = \frac{\partial H}{\partial \psi_{\mathbf{k}}^*}, \quad H = H_2 + H_4, \quad (4.5a)$$

$$H_2 = \sum_{\mathbf{k}} \omega_{\mathbf{k}} \psi_{\mathbf{k}} \psi_{\mathbf{k}}^*, \quad (4.5b)$$

$$H_4 = -\frac{1}{2} \sum_{1234} W_{34}^{12} \psi_1 \psi_2 \psi_3^* \psi_4^* \delta_{34}^{12}. \quad (4.5c)$$

Here the Hamiltonian H is comprised of the quadratic part H_2 , which leads to linear waves with dispersion relation $\omega_{\mathbf{k}} = k^2$, and the interaction Hamiltonian H_4 which describes four-wave coupling of the $2 \leftrightarrow 2$ type. The interaction coefficient W_{34}^{12} can be written in the symmetric form

$$W_{34}^{12} = \frac{\gamma}{4} (A_{1234} + A_{2134} + A_{1243} + A_{2143}), \quad (4.5d)$$

$$A_{1234} = 1 / [(\mathbf{k}_1 - \mathbf{k}_4) \cdot (\mathbf{k}_3 - \mathbf{k}_2) + \Lambda]. \quad (4.5e)$$

If we are using the Jeans swindle from the outset (see Footnote 1) then the sum in Eq. (4.5c) must exclude all terms when any two wavenumbers are equal.

For completeness, we note that if we include a local cubic self-interaction term $-s|\psi|^2\psi$ on the right-hand side of Eq. (4.3a) as well as the gravitational term then the four-wave interaction coefficient would be

$$W_{34}^{12} = -s + \frac{\gamma}{4} (A_{1234} + A_{2134} + A_{1243} + A_{2143}),$$

¹If we start with Eq. (4.3b), i.e., $\Lambda = 0$, from the outset, then we need to set $V_{\mathbf{k}=0} = 0$, which is the Jeans swindle in Fourier space. This corresponds to subtraction of the mean as in Eq. (4.29), i.e., $\langle \rho \rangle_{\Omega} = 0$.

with A_{1234} as in Eq. (4.5e). Finally, the four-wave interaction coefficient for the cubic nonlinear Schrödinger Eq. (4.2) is simply

$$W_{34}^{12} = -s .$$

4.3.2 Kinetic equation and conserved quantities

In the theory of weak wave turbulence we consider ensembles of weakly interacting waves with random phases uniformly distributed in $[0, 2\pi)$, and independently distributed amplitudes [3, 50–52]. We define the wave spectrum

$$n_{\mathbf{k}} = \left(\frac{L}{2\pi} \right)^d \langle |\psi_{\mathbf{k}}|^2 \rangle ,$$

where the angle brackets $\langle \dots \rangle$ denote averaging of “...” over the random phases and amplitudes.

In the limit of an infinite domain $L \rightarrow \infty$ and for weak nonlinearity $|H_4/H_2| \ll 1$ one can derive [19, 3, 4] a wave kinetic equation for the evolution of the spectrum. For $2 \leftrightarrow 2$ wave processes with the interaction Hamiltonian (4.5c), the kinetic equation is

$$\partial_t n_{\mathbf{k}} = 4\pi \int |W_{3\mathbf{k}}^{12}|^2 \delta_{3\mathbf{k}}^{12} \delta(\omega_{3\mathbf{k}}^{12}) n_1 n_2 n_3 n_{\mathbf{k}} \left[\frac{1}{n_{\mathbf{k}}} + \frac{1}{n_3} - \frac{1}{n_1} - \frac{1}{n_2} \right] d\mathbf{k}_1 d\mathbf{k}_2 d\mathbf{k}_3 , \quad (4.6)$$

where $\delta_{3\mathbf{k}}^{12}$ is now a Dirac delta function that imposes wavenumber resonance $\mathbf{k} + \mathbf{k}_3 = \mathbf{k}_1 + \mathbf{k}_2$; likewise frequency resonance $\omega_{\mathbf{k}} + \omega_3 = \omega_1 + \omega_2$ is enforced by the Dirac delta $\delta(\omega_{3\mathbf{k}}^{12})$.

The kinetic equation (4.6) describes the irreversible evolution of an initial wave spectrum via four-wave interaction.² It is the central tool of wave turbulence theory at the lowest level of closure of the hierarchy of moment equations (the theory also allows the study of higher moments or even the full probability density function [3, 50–52]). Equation (4.6) allows one to study the dynamical evolution of a wave spectrum from an arbitrary initial condition, provided the interaction is weak. The spectra that are of greatest interest in wave turbulence theory are the stationary solutions that we discuss in Secs. 4.3.4 and 4.3.5. As well as being the first checkpoint in analysing the wave turbulence of a new system, these spectra also frequently characterise the time-dependent dynamics. We shall return to this point in Sec. 4.5.1.

²Note that the interaction coefficient enters Eq. (4.6) only through its squared modulus, so that the sign of the interaction does not play a role in the weakly nonlinear limit. This means that, for example, in the case of Eq. (4.2) the buildup of a large-scale condensate via an inverse cascade is the same for both the focusing and defocusing case, and the difference only enters in the strongly nonlinear evolution.

As the spectrum evolves under the action of Eq. (4.6) the following two quantities are conserved by the kinetic equation

$$N = \int n_{\mathbf{k}} \, d\mathbf{k}, \quad (4.7a)$$

$$E = \int \omega_{\mathbf{k}} n_{\mathbf{k}} \, d\mathbf{k}. \quad (4.7b)$$

Here N is known as the (density of) waveaction, or particle number, and is conserved for all times by the original Eqs. (4.1), and E is referred to as the (density of) energy. It is the leading-order part of the total Hamiltonian, i.e., H_2 , and is only conserved by Eqs. (4.1) over timescales for which the kinetic equation (4.6) is valid.

For isotropic systems such as Eqs. (4.1) we can express the conservation of invariants (4.7) as scalar continuity equations for the waveaction

$$\partial_t N_k^{(1D)} + \partial_k \eta = 0, \quad N_k^{(1D)} = \mathbb{A}^{(d-1)} n_{\mathbf{k}} k^{d-1}, \quad (4.8a)$$

and for the energy

$$\partial_t E_k^{(1D)} + \partial_k \epsilon = 0, \quad E_k^{(1D)} = \omega_{\mathbf{k}} N_k^{(1D)}. \quad (4.8b)$$

Here $\eta = \eta(k)$ and $\epsilon = \epsilon(k)$ are, respectively, the flux of waveaction and energy through the shell in Fourier space of radius $k = |\mathbf{k}|$. In Eq. (4.8a) we have defined the isotropic 1-dimensional (1D) waveaction spectrum $N_k^{(1D)}$, where $\mathbb{A}^{(d-1)}$ is the area of a unit $(d-1)$ -sphere; likewise in Eq. (4.8b) $E_k^{(1D)}$ is the isotropic 1D energy spectrum.

In the rest of this chapter we will consider a forced-dissipated system, with forcing in a narrow band at some scale k_f and dissipation at the large and small scales k_{\min} and k_{\max} respectively, and assume that these scales are widely separated $k_{\min} \ll k_f \ll k_{\max}$. The interval $k_f < k < k_{\max}$ is known as the direct inertial range, and $k_{\min} < k < k_f$ is called the inverse inertial range, because of the directions that E and N flow through these ranges, as we describe in the next section. In this open setup the local conservation Eqs. (4.8) will hold deep inside the inertial ranges but the global quantities N and E are only conserved if the rates at which they are injected match their dissipation rates.

We examine the open system because it allows the nonequilibrium stationary solutions of Eq. (4.6) to form and persist, revealing the dual cascade in its purest manifestation. The alternative would be to study turbulence that evolves freely from an initial condition. In that case features of the stationary solutions still often characterise the evolving spectra, see Sec. 4.5.1. We leave the study of the time-evolving case to future work and here establish the forms of the stationary spectra

by considering the forced-dissipative setup.

4.3.3 Fjørtoft argument for two conserved invariants

The presence of two dynamical invariants E and N whose densities differ by a monotonic factor of k , here by $\omega_{\mathbf{k}} = k^2$, places strong constraints on the directions in which the invariants flow through \mathbf{k} -space, as pointed out by Fjørtoft [63]. We recapitulate his argument in its open-system form.³

Consider the system in a steady state where forcing balances dissipation: at k_f energy and particles are injected at rate ϵ and η respectively, and dissipated at those rates at k_{\min} or k_{\max} . The ratio of the density of energy to the density of particles is k^2 , and so the energy and particle flux must be related by the same factor at all scales. At the forcing scale this means that $\epsilon \sim k_f^2 \eta$.

The argument proceeds by contradiction. Suppose that the energy is dissipated at the large scale k_{\min} at the rate $\sim \epsilon$ that it is injected. Then at this scale particles would be removed at rate $\sim \epsilon/k_{\min}^2 \sim \eta k_f^2/k_{\min}^2 \gg \eta$ which is impossible because then the particle dissipation rate would exceed the rate of injection. Therefore in a steady state most of the energy must be dissipated at small scales k_{\max} . Likewise, if we assume the particles are removed at the small scale k_{\max} at rate $\sim \eta$ then energy would be removed at the impossible rate $\sim \epsilon k_{\max}^2/k_f^2 \gg \epsilon$ so most of the particles must be removed at large scales k_{\min} instead.

Therefore, this argument predicts that the scale containing most of the energy must move towards high k while the scale containing the most particles must move towards low k . Particles are then removed if k_{\min} represents a dissipation scale. However if there is no dissipation here then the spectrum develops a localised bump as the particles accumulate at the largest scale—this is the condensate. In this case k_{\min} represents the transition scale between the condensate, which becomes strongly nonlinear as the dual cascade proceeds, and the weakly nonlinear wave component of the system which continues to obey Eq. (4.6).

It is thus the Fjørtoft argument that robustly predicts that particles accumulate at the largest available scale in the system, while energy is lost by the dissipation at k_{\max} , a process of simultaneous nonequilibrium condensation and “evaporative cooling” [8].

The Fjørtoft argument does not specify whether the invariants move via local scale-by-scale interactions, or by a direct transfer from the intermediate to the extremal scales. In the next Sec. 4.3.4 we consider spectra on which the two invariants move via a local cascade.

³See also the argument based on centroids in section 2.6.

4.3.4 Kolmogorov-Zakharov flux spectra as formal solutions of the kinetic equation

The landmark result of the theory of weak wave turbulence is the discovery of spectra on which invariants move with constant flux through \mathbf{k} -space via a local scale-by-scale cascade, potentially realising the predictions of the Fjørtoft argument. [However, anticipating the results of Sec. 4.3.6, it turns out that for the Schrödinger-Newton Eqs. (4.3) and nonlinear Schrödinger Eq. (4.2) these spectra lead in most cases to cascades with the fluxes in the wrong direction, a contradiction that we resolve in the remainder of this chapter.] These are the Kolmogorov-Zakharov spectra [4] and are analogous to Kolmogorov's famous $k^{-5/3}$ energy cascade spectrum for 3D classical strongly-nonlinear hydrodynamical turbulence [5]. When they exist, they are steady nonequilibrium solutions of the kinetic equation in which the spectra are scale-invariant, i.e.,

$$n_{\mathbf{k}} \propto k^{-x}. \quad (4.9)$$

Necessary (but not sufficient) conditions for such spectra to exist are that both the dispersion relation and interaction coefficient are themselves both scale-invariant. In our case the dispersion relation is $\omega_{\mathbf{k}} = k^2$. For the interaction coefficient we require a homogeneous function in the sense that

$$W_{\mu\mathbf{k}_3 \mu\mathbf{k}_4}^{\mu\mathbf{k}_1 \mu\mathbf{k}_2} = \mu^\beta W_{\mathbf{k}_3 \mathbf{k}_4}^{\mathbf{k}_1 \mathbf{k}_2}.$$

For the Schrödinger-Helmholtz Eqs. (4.1) we obtain a scale-invariant interaction coefficient in either the Schrödinger-Newton limit $\ell \ll \ell_*$ (in which case $\beta = -2$) or in the nonlinear Schrödinger limit $\ell \gg \ell_*$ (where $\beta = 0$).

The Kolmogorov-Zakharov spectra are obtained by making a so-called Zakharov-Kraichnan transform in the kinetic equation (4.6) and using the scaling behaviour of all quantities under the integral [19, 3, 4], or via dimensional analysis [3, 149]. We omit the details and quote the results here.

For systems of $2 \leftrightarrow 2$ wave scattering in d spatial dimensions, the spectrum that corresponds to a *constant flux of particles* and zero flux of energy has index

$$x_{\text{FN}} = d + \frac{2\beta}{3} - \frac{2}{3}.$$

The spectrum of *constant energy flux* with zero particle flux is

$$x_{\text{FE}} = d + \frac{2\beta}{3}.$$

In particular for the Schrödinger-Newton Eqs. (4.3) we have $\beta = -2$, so

$$x_{\text{FN}} = 1, \quad x_{\text{FE}} = 5/3 \quad \text{for} \quad d = 3, \quad (4.10a)$$

$$x_{\text{FN}} = 0, \quad x_{\text{FE}} = 2/3 \quad \text{for} \quad d = 2, \quad (4.10b)$$

while for the nonlinear Schrödinger Eq. (4.2) $\beta = 0$, so

$$x_{\text{FN}} = 7/3, \quad x_{\text{FE}} = 3 \quad \text{for} \quad d = 3, \quad (4.10c)$$

$$x_{\text{FN}} = 4/3, \quad x_{\text{FE}} = 2 \quad \text{for} \quad d = 2. \quad (4.10d)$$

Results (4.10c) and (4.10d) are known [19, 4, 3] but the pure-flux Kolmogorov-Zakharov spectra Eqs. (4.10a) and (4.10b) for the Schrödinger-Newton equations are new results that we report for the first time here.

4.3.5 Equilibrium spectra

The kinetic equation redistributes E and N over the degrees of freedom (wave modes) as it drives the system to thermodynamic equilibrium. Equilibrium is reached when the invariant $\sigma = (E + \mu N)/T$ is distributed evenly across all wave modes. This is realised by the Rayleigh-Jeans spectrum⁴

$$n_{\mathbf{k}} = \frac{T}{\omega_{\mathbf{k}} + \mu}, \quad (4.11)$$

where T is the temperature and μ is the chemical potential.

In particular the spectrum is scale invariant, satisfying Eq. (4.9), when there is equipartition of particles only (the thermodynamic potentials $\mu, T \rightarrow \pm\infty$ such that $T/\mu = n_{\mathbf{k}} = \text{const}$) or of energy only (obtained when $\mu = 0$). We denote the corresponding spectral indices for thermodynamic equipartition of particles and energy, respectively, as

$$x_{\text{TN}} = 0 \quad \text{and} \quad x_{\text{TE}} = 2. \quad (4.12)$$

4.3.6 Directions of the energy and particle fluxes and realisability of the scale-invariant spectra

With the various indices for the stationary Kolmogorov-Zakharov and Rayleigh-Jeans power-law spectra in hand, we now turn to the following simple argument to determine the directions of the particle and energy fluxes $\eta(x)$ and $\epsilon(x)$.

⁴Formally, achieving the Rayleigh-Jeans spectrum depends on there being a small-scale cutoff k_{max} to prevent σ being shared over an infinite number of wave modes, i.e., the trivial solution $n_{\mathbf{k}} = 0$ for every \mathbf{k} .

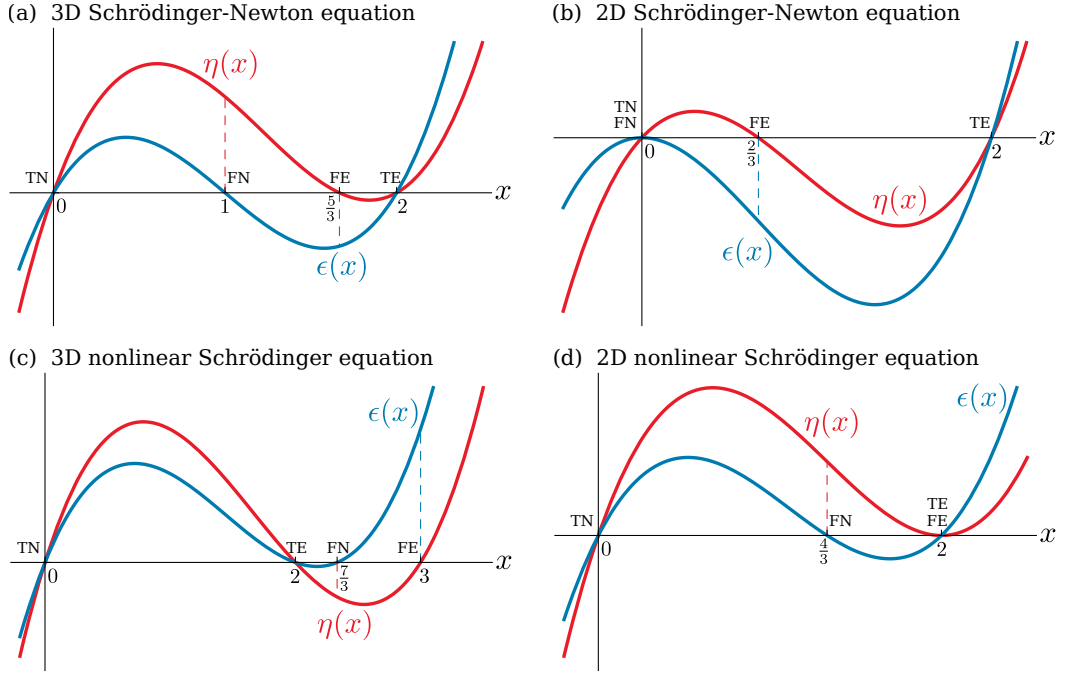


Figure 4.3: Particle flux $\eta(x)$ (in red) and energy flux $\epsilon(x)$ (in blue) as a function of spectral index x for the limits of the Schrödinger-Helmholtz model. Upper panels for the Schrödinger-Newton model in (a) $d = 3$, and (b) in $d = 2$. Lower panels for the nonlinear Schrödinger model in (c) $d = 3$, and (d) $d = 2$. Dashed lines indicate the signs of the fluxes when the spectral index takes the values x_{FN} and x_{FE} .

We consider what the flux directions will be when the spectrum is a power-law as in Eq.(4.9). We expect the fluxes to respond to a very steep spectrum by spreading the spectrum out. Therefore for x large and positive (spectrum sharply increasing towards low wavenumber) we expect both $\eta, \epsilon > 0$, and for x large and negative (spectrum ramping at high wavenumber) we expect $\eta, \epsilon < 0$. Furthermore, both fluxes will be zero for both thermal equilibrium exponents x_{TN} and x_{TE} . Finally, the particle flux vanishes for the pure energy flux spectrum with exponent x_{FE} , and the energy flux vanishes for the pure particle flux exponent x_{FN} . By continuity the signs of both fluxes for all x are fully determined by their signs at infinity and the locations of their zero crossings. The fluxes will schematically vary in the manner shown in Fig.4.3(a,b) for the Schrödinger-Newton model and Fig.4.3(c,d) for the nonlinear Schrödinger model.

First we consider the Schrödinger-Newton equations. In both 3D and 2D at the spectral index corresponding to pure energy flux x_{FE} we find that ϵ is negative. On x_{FN} , the pure particle flux spectrum, we find that η is positive in 3D, whereas in 2D there is a degeneracy with the particle equipartition spectrum $x_{\text{FN}} = x_{\text{TN}}$ and correspondingly $\eta = 0$ there. These findings are in contradiction to the Fjørtoft argument.

For the nonlinear Schrödinger equation in 3D ϵ is positive at x_{FE} and η is negative at x_{FN} . This is in agreement with the Fjørtoft argument. We therefore naively expect that in 3D the Kolmogorov-Zakharov flux cascades are possible. It turns out that the inverse particle Kolmogorov-Zakharov spectrum is realised, with a scale-by-scale transfer of particles to small scales, however the direct energy cascade is nonlocal and the spectrum must be modified to correct a logarithmic divergence in the infrared limit, see refs. [19, 3] for details.

For the 2D nonlinear Schrödinger equation the energy flux and equipartition spectra are degenerate $x_{\text{FE}} = x_{\text{TE}}$, giving $\epsilon = 0$ there, and at the particle flux spectral index x_{FN} we find η is positive.

These results for the Schrödinger-Newton equations and 2D nonlinear Schrödinger equation are in contradiction to the Fjørtoft argument for a forward energy cascade and inverse particle cascade. However the Fjørtoft argument is robust and predicts that if an initial spectrum evolves, it must push most of the energy towards small scales and particles towards large scales. We therefore conclude that the Schrödinger-Newton Eqs. (4.3), and the nonlinear Schrödinger Eq. (4.2) in 2D, do not accomplish this via the Kolmogorov-Zakharov spectra that are determined solely by the values of the flux. To resolve this paradox we develop a simplified theory to reduce the integro-differential kinetic equation to a partial differential equation that is analytically tractable.

4.3.7 Differential approximation model for wave turbulence

The Kolmogorov-Zakharov solutions of the kinetic equation for the Schrödinger-Newton equations in 3D and 2D, and for the nonlinear Schrödinger equation in 2D, predict the wrong directions for the fluxes as compared to the Fjørtoft argument. Such solutions cannot be realised for any finite scale separation between forcing and dissipation. From experience with other wave turbulence systems we expect that the flux-carrying spectra in these cases are instead close to the zero-flux thermal Rayleigh-Jeans solutions, but with deviations that carry the flux [3, 150, 151]. These deviations are small deep inside the inertial ranges but become large at the ends, making the spectrum decay rapidly to zero near the dissipation scales. Spectra of this sort are termed “warm” cascades [150, 152, 16, 17]. A feature of these solutions is that the thermodynamic potentials T and μ will be functions of the flux they have to accommodate,⁵ and the scales at which the spectrum decays, i.e.,

$$\frac{T}{\mu} = f(\eta, \omega_{\text{min}}) \quad (4.13)$$

⁵Note that the temperature T of the warm cascade refers to the energy shared between wave modes, and is not related to the temperature of particle or molecular degrees of freedom of the material at hand (Bose gas or nonlinear optical sample), which plays no role in this analysis.

for the inverse cascades and

$$T = g(\epsilon, \omega_{\max}) \quad (4.14)$$

for direct cascades [3, 150, 151], where the functional forms of f and g are to be found, and we have converted from wavenumber to frequency using the dispersion relation $\omega = k^2$ (we will continue to refer to “scales” when discussing frequencies as the isotropy of the spectrum allows us to use the dispersion relation to convert between spatial and temporal scales).

To describe warm cascade states we develop a differential approximation model that simplifies the kinetic equation by assuming that interactions are super-local in frequency space ($\omega_k \approx \omega_1 \approx \omega_2 \approx \omega_3$). This allows the collision integral to be reduced to a purely differential operator. Asymptotically-correct stationary solutions of this reduced model can then be found analytically, and these will be qualitatively similar to the solutions for the full kinetic equation [19, 150–152, 16, 17, 153].

The reduction of the general four-wave kinetic equation to the differential approximation model is done explicitly in Ref. [19]. Here we take a heuristic approach based on the scaling of the kinetic equation and neglect the full calculation of numerical prefactors.

We integrate over angles in \mathbf{k} -space and change variables to frequency. The general form of the differential approximation model is then an ordinary differential equation in local conservative form

$$\omega^{d/2-1} \frac{\partial n}{\partial t} = \frac{\partial^2 R}{\partial \omega^2}, \quad (4.15a)$$

where $n = n(\omega)$ is the spectrum expressed as a function of ω , and the quantity

$$R = S\omega^\lambda n^4 \frac{\partial^2}{\partial \omega^2} \left(\frac{1}{n} \right) \quad (4.15b)$$

is constructed so as to ensure that the Rayleigh-Jeans spectrum is a stationary solution [$\partial_{\omega\omega}(1/n)$ term], the n^4 term derives from the fact that four-wave interactions are responsible for the spectral evolution, the total n scaling matches the kinetic equation, and S is a constant.

To find λ for the systems considered in the present chapter we examine how the kinetic Eq. (4.6) scales with ω . Schematically the kinetic equation is

$$\dot{n} = \int W^2 n^3 \delta(\mathbf{k}) \delta(\omega) (d\mathbf{k})^3 \sim n^3 k^{2\beta+2d-2} \sim n^3 \omega^{\beta+d-1}$$

while the differential approximation (4.15) scales as

$$\omega^{d/2-1}\dot{n} \sim n^3\omega^{\lambda-4} .$$

Comparing powers of ω we find that

$$\lambda = \beta + \frac{3d}{2} + 2 . \quad (4.16)$$

4.3.8 Fluxes in the differential approximation

Comparing Eq. (4.15a) with (4.8a) and (4.8b) we see that the particle and energy fluxes expressed as a function of ω are, up to a geometrical factor that can be absorbed into S ,

$$\eta = -\frac{\partial R}{\partial \omega} \quad \text{and} \quad \epsilon = -\omega \frac{\partial R}{\partial \omega} + R . \quad (4.17)$$

respectively.

Putting a power law spectrum $n = \omega^{-x/2}$ into Eqs. (4.15) and (4.17) allows us to find expressions for the fluxes. The particle flux is

$$\eta = -\frac{x}{2} \left(\frac{x}{2} - 1 \right) \left(\beta + \frac{3d}{2} - \frac{3x}{2} \right) S \omega^{\beta+3d/2-3x/2-1}$$

and vanishes when $x = 0$ or $x = 2$, corresponding to the thermodynamic particle and energy spectral indices of Eqs. (4.12). The particle flux also vanishes when $x = d + \frac{2\beta}{3}$, corresponding to the energy flux spectral index x_{FE} of Eqs. (4.10a) to (4.10d). The energy flux is

$$\epsilon = -\frac{x}{2} \left(\frac{x}{2} - 1 \right) \left(\beta + \frac{3d}{2} - \frac{3x}{2} - 1 \right) S \omega^{\beta+3d/2-3x/2}$$

and is again zero for the Rayleigh-Jeans spectra where $x = 0$ or $x = 2$, and for the constant particle flux (zero energy flux) Kolmogorov-Zakharov spectrum with $x = d + \frac{2\beta}{3} - \frac{2}{3}$.

Thus in the differential approximation model we recover the results of Secs. 4.3.4 and 4.3.5. Furthermore, this model gives a quantitative prediction of $\eta(x)$ and $\epsilon(x)$ for all values of x (to within the limits of the super-local assumption, and the numerical determination of S). For example taking $S = 1$ and $\omega = 1$ we have the cubic functions

$$\begin{aligned} \eta &= -\frac{x}{2} \left(\frac{x}{2} - 1 \right) \left(\beta + \frac{3d}{2} - \frac{3x}{2} \right) , \\ \epsilon &= -\frac{x}{2} \left(\frac{x}{2} - 1 \right) \left(\beta + \frac{3d}{2} - \frac{3x}{2} - 1 \right) , \end{aligned}$$

that are drawn in Fig. 4.3, with $\beta = -2$ for the Schrödinger-Newton Eqs. (4.3) and $\beta = 0$ for the nonlinear Schrödinger Eq. (4.2).

4.4 Turbulent spectra in the Schrödinger-Helmholtz model

4.4.1 Reconciling with the Fjørtoft argument

Having established the cases in which the Kolmogorov-Zakharov spectra give either the wrong flux directions or zero fluxes for the Schrödinger-Newton and the nonlinear Schrödinger models, we now seek the spectra that give the correct fluxes. To agree with the Fjørtoft argument we require a spectrum for the direct inertial range that carries the constant positive energy flux ϵ from the forcing scale ω_f up to the dissipation scale ω_{\max} , but carries no particles. Setting $\eta = \partial_\omega R = 0$ in eqs. (4.17) we obtain the ordinary differential equation

$$\epsilon = R = \text{const} > 0 \tag{4.18}$$

in the direct inertial range.

Likewise in the inverse inertial range we require a spectrum that carries the constant negative particle flux η from ω_f to dissipate at ω_{\min} , but carries zero energy. Setting $\epsilon = 0$ in Eq. (4.17) we obtain $\partial_\omega R = R/\omega$ and so

$$\eta = -\frac{R}{\omega} = \text{const} < 0 \tag{4.19}$$

in the inverse inertial range.

We now proceed in turn through the 3D and 2D Schrödinger-Newton equations, followed by the 2D nonlinear Schrödinger equation, and use Eqs. (4.18) and (4.19) to resolve the predictions from Sec. 4.3.6 that are in conflict with the Fjørtoft argument.

(A full qualitative classification of the single-flux stationary spectra in the differential approximation model for four-wave turbulence is presented in Ref. [154], based on the phase space analysis of an auxiliary dynamical system. Those general results are relevant to the systems under consideration in this chapter, however here we will concentrate on the particular functional form of the flux-carrying spectra in the inertial range, and establish the relationships (4.13), (4.14) between the thermodynamic potentials and the fluxes, in the spirit of Refs. [3, 150, 151].)

4.4.2 Spectra in the 3D Schrödinger-Newton model

In Sec. 4.3.6 we found that in the 3D Schrödinger-Newton Eqs. (4.3) both the particle and the energy cascade had the wrong sign on their respective Kolmogorov-Zakharov

spectra. We specialise Eq. (4.16) to this model by setting $\beta = -2$ and $d = 3$ and, following Ref. [3], we use the ordinary differential Eqs. (4.18) and (4.19) to seek warm cascade solutions that carry the fluxes in the directions predicted by Fjørtoft’s argument.

4.4.2.1 Warm inverse particle cascade in the 3D Schrödinger-Newton model

The warm cascade is an equilibrium Rayleigh-Jeans spectrum with a small deviation. Thus we propose the spectrum

$$n = \frac{T}{\omega + \mu + \theta(\omega)} \quad (4.20)$$

and assume that the disturbance $\theta(\omega)$ is small deep in the inverse inertial range, i.e., $\omega_{\min} \ll \omega \ll \omega_f$. We substitute this into Eqs. (4.15) and impose the constant-flux condition (4.19) for the inverse cascade. Linearising with respect to the small disturbance, we obtain the equation

$$\theta''(\omega) = -\frac{\eta}{ST^3} \frac{(\omega + \mu)^4}{\omega^{7/2}}.$$

Integrating twice, and noting that $|\eta|$ is negative, yields the following expression for the deviation away from the thermal spectrum that is valid deep in the inertial range

$$\theta(\omega) = \frac{|\eta|}{ST^3} \left(\frac{4\omega^{5/2}}{15} + \frac{16\mu\omega^{3/2}}{3} - 24\mu^2\omega^{1/2} + \frac{16\mu^3}{3\omega^{1/2}} + \frac{4\mu^4}{15\omega^{3/2}} \right), \quad (4.21)$$

where we have absorbed the two integration constants by renormalising T and μ .

We can use (4.21) to obtain a relation between the flux and thermodynamic parameters of the form (4.13) via the following “approximate matching” argument. We need the warm cascade spectrum to terminate at the dissipation scale ω_{\min} . Therefore near the dissipation scale we expect $\theta(\omega)$ to become significant, compared to the other terms in the denominator of (4.20), i.e., we expect $\theta(\omega) \sim \omega + \mu$ near ω_{\min} . We put these terms into balance at ω_{\min} and assume the ordering⁶ $\omega_{\min} \ll \mu$. Taking the leading term from Eq. (4.21), we obtain the flux scaling

$$\left(\frac{T}{\mu} \right)^3 \sim \frac{4}{15S} |\eta| \omega_{\min}^{3/2}. \quad (4.22)$$

Of course this matching procedure is not strictly rigorous as Eq. (4.21) was derived

⁶If instead we set $\omega_{\min} \sim \mu$ or $\omega_{\min} \gg \mu$ then $\theta(\omega)$ would not become small for any $\omega \geq \omega_{\min}$, contradicting the assumption under which we derived Eq. (4.21).

for small θ and we are extending it to where θ is large. Nevertheless, we expect that the scaling relation (4.22) will give the correct functional relationship between the thermodynamic parameters and the flux and dissipation scale. (Results derived in a similar spirit in other systems give predictions that agree well with direct numerical simulations, see e.g., Ref. [150].)

Now we examine the structure of the inverse cascade near the dissipation scale. Assuming that the spectrum around $(\omega - \omega_{\min}) \ll \omega_{\min}$ is analytic, the condition $n(\omega_{\min}) = 0$ suggests that the spectrum terminates in a compact front whose leading-order behaviour is of the form $n = A(\omega - \omega_{\min})^\sigma$. Again we substitute this ansatz into Eqs. (4.15), and demand that the flux is carried all the way to the dissipation scale, i.e., we impose the condition (4.19). Requiring that the flux is frequency independent fixes A and σ , and we obtain the compact front solution at the dissipation scale

$$n = \left[\frac{9 |\eta| (\omega - \omega_{\min})^2}{10 S \omega_{\min}^{7/2}} \right]^{1/3}. \quad (4.23)$$

We shall find below that the compact front solution is nearly identical near each dissipation range in each model and dimensionality that we examine. This is because the $\sim n^3$ scaling of the spectrum in Eqs. (4.15), and the need for the compact front to vanish at the respective dissipation scale ω_* fixes $\sigma = 2/3$. The only difference will be the flux and the power of the respective ω_* in the coefficient, and the sign difference in the power law.

We note that Eq. (4.21) suggests that $\theta(\omega)$ could again become large at high frequency. Arguing as above, this permits the spectrum to terminate at a compact front at frequency $\omega_+ > \omega_{\min}$. One could argue likewise for the warm direct energy cascade spectrum, see Eq. (4.24) below. Indeed all the warm cascade spectra discussed in this chapter contain the possibility that they might be bounded by two compact fronts. We discuss this matter in Appendix 4.C.

Using the differential approximation we have shown how the inverse cascade of particles in the 3D Schrödinger-Newton Eqs. (4.3) is carried by a warm cascade that closely follows a Rayleigh-Jeans spectrum in the inertial range, with a strong deviation near the dissipation scale that gave us an approximate scaling relation between the thermodynamic parameters and the cascade parameters. We also investigated the structure of the spectrum at the dissipation scale and found it to be a compact front with a $\frac{2}{3}$ -power law that vanishes at ω_{\min} .

In the rest of this chapter we will use the same procedures, with the model and dimensionality under consideration giving us the appropriate ω -scaling in the differential approximation, to identify similar features of the cascades. First, we turn to the direct cascade of energy in the 3D Schrödinger-Newton Eqs. (4.3).

4.4.2.2 Warm direct energy cascade in the 3D Schrödinger-Newton model

To find a direct cascade of energy for the 3D Schrödinger-Newton equations we again use the warm cascade ansatz (4.20) and this time impose the constant energy flux condition (4.18). We go through the same approximate matching procedure as in Sec. 4.4.2.1: we find $\theta(\omega)$ under the assumption that it is small,

$$\theta(\omega) = \frac{\epsilon}{ST^3} \left(\frac{4\omega^{3/2}}{3} - 16\mu\omega^{1/2} + \frac{8\mu^2}{\omega^{1/2}} + \frac{16\mu^3}{15\omega^{3/2}} + \frac{4\mu^4}{35\omega^{5/2}} \right), \quad (4.24)$$

where again we have absorbed the two integration constants into T and μ . Extending (4.24) towards ω_{\max} where we require it to balance the other terms in the denominator of (4.20), and assuming⁷ $\mu \ll \omega_{\max}$ gives a scaling relation of the type (4.14)

$$T^3 \sim \frac{4}{3S} \epsilon \omega_{\max}^{1/2}. \quad (4.25)$$

In the immediate vicinity of ω_{\max} we again expect a compact front. Substituting $n = A(\omega_{\max} - \omega)^\sigma$ into (4.18) gives the leading-order structure

$$n = \left[\frac{9\epsilon(\omega_{\max} - \omega)^2}{10S\omega_{\max}^{9/2}} \right]^{1/3}.$$

Again we note that Eq. (4.24) suggests that θ can be made large at some low frequency that would lead to a second compact-front cutoff at $\omega_- < \omega_{\max}$. All the warm cascade spectra we discuss here have the potential to be terminated at two compact fronts. This is discussed in Appendix 4.C.

4.4.2.3 Warm dual cascade in the 3D Schrödinger-Newton model

In summary, the results of Secs. 4.4.2.1 and 4.4.2.2 predict that for the 3D Schrödinger-Newton model in the forced-dissipative setup, the movement of particles to large scales and energy to small scales is realised by a dual warm cascade spectrum. This spectrum starts close to the Rayleigh-Jeans distribution (4.11) near the forcing scale ω_f and then deviates strongly away, until it vanishes at compact 2/3 power-law fronts at the dissipation scales ω_{\min} and ω_{\max} . We show the dual warm cascade in Fig. 4.4, which was obtained by numerically integrating Eq. (4.18) forwards and Eq. (4.19) backwards from the initial condition that the spectrum and its derivative matched the Rayleigh-Jeans spectrum (4.11) at $\omega_f = 10^5$, with $T = \mu = 10^4$. The warm cascades carry a particle flux $\eta = -3.75$ to large scales and energy flux $\epsilon = \omega_f^2 |\eta|$ to

⁷For $\omega_{\max} \sim \mu$ or $\omega_{\max} \gg \mu$ there is no range of $\omega \leq \omega_{\max}$ for which $\theta(\omega)$ is small.

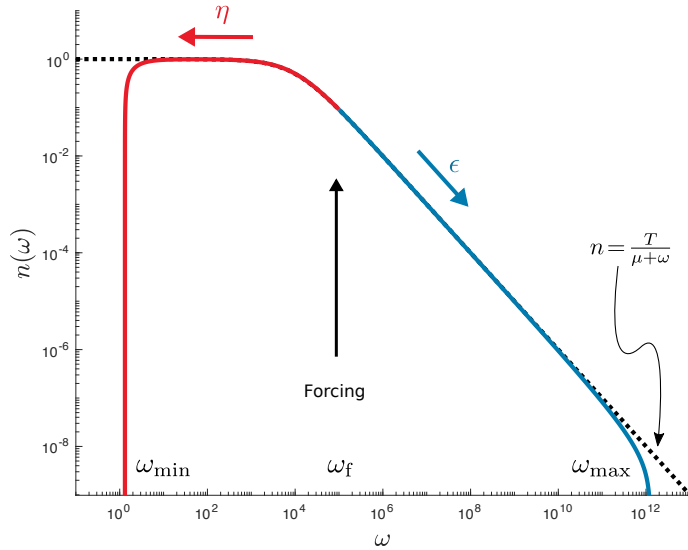


Figure 4.4: Dual warm cascade in the 3D Schrödinger-Newton equations. The inverse particle cascade, with negative particle flux η , is shown in red. In blue is the direct energy cascade with positive flux ϵ . The black dashed line is the thermodynamic equipartition spectrum (4.11). (See main text for parameters.)

small scales, and the geometric constant $S = 1$.

The dual warm cascade for the 2D Schrödinger-Newton and 2D nonlinear Schrödinger models can be obtained in a similar fashion. They are qualitatively similar to Fig. 4.4 so we omit displaying them.

4.4.3 Spectra in the 2D Schrödinger-Newton model

Now we turn to the 2D Schrödinger-Newton Eqs. (4.3), setting $\beta = -2$ and $d = 2$ in Eq. (4.16). In Sec. 4.3.6 we found that the particle equipartition and cascade spectra coincided, making the particle flux zero, and that the energy flux had the wrong sign.

4.4.3.1 Log-corrected inverse particle cascade in the 2D Schrödinger-Newton model

The degeneracy between the particle Rayleigh-Jeans and Kolmogorov-Zakharov spectra $n \sim \omega^0$ can be lifted by making a logarithmic correction to this spectrum. Substituting the trial solution $n = B \ln^z(\omega/\omega_{\min})$ into Eqs. (4.15) and enforcing constant negative particle flux (4.19) that is independent of ω gives

$$n = \left[\frac{3|\eta|}{S} \ln\left(\frac{\omega}{\omega_{\min}}\right) \right]^{1/3} \quad (4.26)$$

to leading order deep in the inverse inertial range.

To find a relation between the thermodynamic parameters and the cascade parameters we carry out the approximate matching procedure described in Sec. 4.4.2.1 at low frequency $\omega \sim \omega_{\min} \ll \mu$, obtaining

$$\left(\frac{T}{\mu}\right)^3 \sim \frac{|\eta|}{S} \ln \omega_{\min}.$$

As $\omega \rightarrow \omega_{\min}$ the spectrum in Eq. (4.26) becomes zero, as we would expect given ω_{\min} is a dissipation scale. However we note that this is only a qualitative statement as subleading terms will start to dominate in this limit, meaning that Eq. (4.26) is no longer the correct stationary spectrum there. To obtain the correct leading-order structure near ω_{\min} we look for a compact front solution and find once again a 2/3 power law,

$$n = \left[\frac{9|\eta|(\omega - \omega_{\min})^2}{10S\omega_{\min}^2} \right]^{1/3}.$$

4.4.3.2 Warm direct energy cascade in the 2D Schrödinger-Newton model

To find a forward energy cascade for the 2D Schrödinger-Newton model we again look for a warm cascade, substituting Eq. (4.20) into (4.15) and seeking a constant energy flux (4.18). Solving for the perturbation and matching the deviation to the other terms in the denominator in (4.20) at $\omega \sim \omega_{\max} \gg \mu$ gives the scaling relation

$$T^3 \sim \frac{\epsilon\omega_{\max}^2}{6S}.$$

The compact front near ω_{\max} has leading-order form

$$n = \left[\frac{9\epsilon(\omega_{\max} - \omega)^2}{10S\omega_{\max}^3} \right]^{1/3}.$$

4.4.4 Spectra in the 2D nonlinear Schrödinger model

In Sec. 4.3.6 we found that the Kolmogorov-Zakharov particle flux spectrum for the nonlinear Schrödinger model was positive rather than negative, and that the Kolmogorov-Zakharov energy flux spectrum coincides with the Rayleigh-Jeans energy equipartition spectrum. We specialise to the 2D nonlinear Schrödinger Eq. (4.2) by setting $\beta = 0$ and $d = 2$ in Eq. (4.16) and take these issues in turn. (These results recapitulate and extend the discussion in chapter 15 of Ref. [3].)

4.4.4.1 Warm inverse particle cascade in the 2D nonlinear Schrödinger model

The approximate matching procedure described above gives the scaling relation

$$\left(\frac{T}{\mu}\right)^3 \sim \frac{|\eta|}{6S\omega_{\min}^2}$$

for the inverse cascade. The compact front solution at the dissipation scale has the structure

$$n = \left[\frac{9|\eta|(\omega - \omega_{\min})^2}{10S\omega_{\min}^4} \right]^{1/3}.$$

4.4.4.2 Log-corrected direct energy cascade in the 2D nonlinear Schrödinger model

The degeneracy of $n \propto \omega^{-1}$ corresponding to both the Kolmogorov-Zakharov energy flux spectrum and the Rayleigh-Jeans energy equipartition spectrum can be again lifted by making a logarithmic correction. Substituting the spectrum $n = (B/\omega) \ln^z(\omega_{\max}/\omega)$ into Eqs. (4.15) and imposing Eq. (4.18) we obtain

$$n = \frac{1}{\omega} \left[\frac{3\epsilon \ln(\omega_{\max}/\omega)}{S} \right]^{1/3}. \quad (4.27)$$

Comparing Eq. (4.27) to the energy equipartition spectrum $n = T/\omega$ we have a relation of the kind in Eq. (4.14), namely

$$T^3 \sim \frac{3\epsilon}{S} \ln \omega_{\max}. \quad (4.28)$$

We obtain the same scaling [apart from the factor of 3 on the right-hand side of Eq. (4.28)] if we assume a warm cascade and carry out the approximate matching procedure as described in Sec. 4.4.2.1. This is natural as the log-corrected solution (4.27) is of a prescribed form whereas in the warm cascade argument the perturbation θ is not constrained from the outset, so the two solutions are two different perturbations from the thermal spectrum. However by continuity they should give the same scaling of thermal with cascade parameters, differing only by an $\mathcal{O}(1)$ constant.

As in Sec. 4.4.3.1 the log-corrected spectrum (4.27) becomes zero at the dissipation scale. However the structure will not be correct here as sub-leading terms would start to become significant. The correct leading-order structure for the front is again the 2/3 power-law

$$n = \left[\frac{9\epsilon(\omega_{\max} - \omega)^2}{10S\omega_{\max}^5} \right]^{1/3}.$$

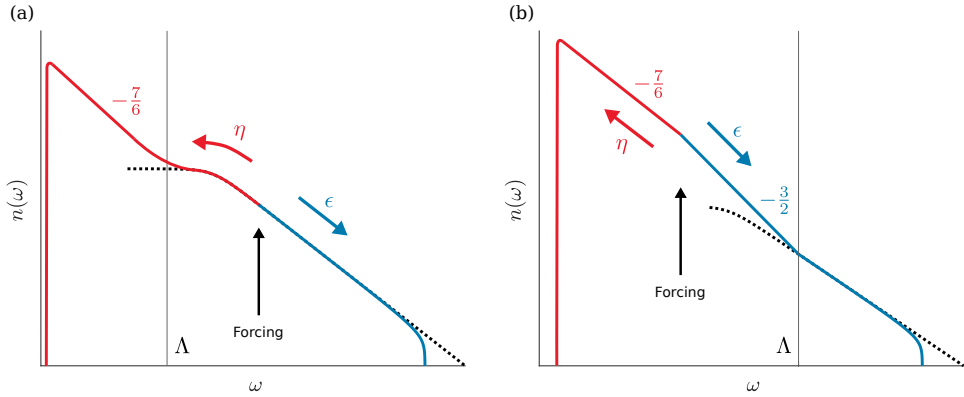


Figure 4.5: Sketch of the crossover from a warm cascade [which follows closely the thermodynamic spectrum (4.11) shown in black dashes] to a scale-free cascade, the latter with the Kolmogorov-Zakharov spectral indices shown, in the 3D Schrödinger-Helmholtz equations. The crossover happens around $\omega \approx \Lambda$, with the warm cascade in $\omega \gg \Lambda$ and the Kolmogorov-Zakharov cascade in $\omega \ll \Lambda$. Depending on placement of the forcing scale the crossover happens (a) in the inverse cascade (shown in red) or (b) in the direct cascade (shown in blue).

4.4.5 Crossover from warm to Kolmogorov-Zakharov cascade in the 3D Schrödinger-Helmholtz model

As mentioned in Sec. 4.3.6 the dual cascade in the 3D nonlinear Schrödinger limit of (4.1) is achieved by a scale-invariant Kolmogorov-Zakharov spectrum, rather than the warm cascade discussed in Sec. 4.4.2 for the 3D Schrödinger-Newton limit. Both these two regimes may be accessed if the removal of waveaction from the weakly nonlinear wave content of the system (through dissipation or absorption into the condensate) is situated at larger scales than the cosmological constant which controls the crossover between the two limits of Eqs. (4.1), i.e., if $\omega_{\min} \ll \Lambda$. We sketch this schematically in Fig. 4.5(a) when $\omega_f \gg \Lambda$, so the crossover from the Kolmogorov-Zakharov to the warm cascade happens in the inverse inertial range, and in Fig. 4.5(b) when $\omega_f \ll \Lambda$ and the crossover happens in the direct inertial range.

Note that Fig. 4.5 is a sketch and not produced directly by using the stationary differential approximation model (4.17). This is because in the crossover regime $\omega \approx \Lambda$ the interaction coefficient (4.5d) cannot be put into scale-invariant form. Accurate realisations of Fig. 4.5 must await direct numerical simulation of Eqs. (4.1) in future work.

The crossover from a scale-invariant cascade dominated by flux to an equipartition-like spectrum at small scales is common in turbulence, when a flux-dominated spectrum runs into a scale where the flux stagnates and thermalises. The stagnation is due to a mismatch of flux rate between the scale-invariant spectrum and the

small-scale processes, whether that be (hyper-)dissipation in hydrodynamic turbulence [152, 155], or a different physical regime such as the crossover from hydrodynamic to Kelvin wave turbulence in superfluids [156]. Our case here, the crossover from the nonlinear Schrödinger to the Schrödinger-Newton regime, is more like the latter but again the details await further work.

4.5 Conclusion and outlook

4.5.1 Summary and discussion of results

In this chapter we have developed the theory of weak wave turbulence in the Schrödinger-Helmholtz Eqs. (4.1), which contain as limits both the nonlinear Schrödinger and Schrödinger-Newton Eqs. (4.2) and (4.3). We obtained the kinetic equation for the Schrödinger-Helmholtz model in the case of four-wave turbulence, that is of random fluctuations of the field with no condensate present, and we used the Fjørtoft argument to predict the dual cascade of particles upscale and energy downscale in this model.

Using the differential approximation of the full kinetic equation, we have characterised the statistically steady states of its Schrödinger-Newton and nonlinear Schrödinger limits in the case of a forced-dissipated system. We found that the dual cascade is achieved via a warm spectrum for the Schrödinger-Newton limit in 2D and 3D, and for the nonlinear Schrödinger limit in 2D. For the 3D nonlinear Schrödinger limit the Kolmogorov-Zakharov spectra are responsible for the cascades, and we have schematically illustrated the crossover between the warm and Kolmogorov-Zakharov cascades when both limits of the full Schrödinger-Helmholtz model are accessible.

Finally we found scaling relationships between the thermodynamic parameters and the fluxes and dissipation scales of the type (4.13) and (4.14) for these cascades. We have thus characterised the processes by which particles are condensed at the largest scales, and energy sent to small scales, in both limits of the Schrödinger-Helmholtz model. The results for the nonlinear Schrödinger model have appeared in the literature before, but the results for the Schrödinger-Newton model are new and are relevant to the problem of cosmological structure formation in a fuzzy dark matter universe, and to optical systems where nonlocal effects are significant.

For the bulk of this work we considered an open system where forcing matched dissipation. This allowed us to discuss the stationary warm spectra that will realise the dual cascade in the forced-dissipated system. There remains the question of how the dual cascade will be realised in the time-dependent case where turbulence evolves from an initial condition; such a case is far more relevant when discussing the formation of galaxies, and realistic protocols in an optics experiment.

Experience with other wave turbulence systems shows that time-dependent cascades are strongly controlled by the capacity of the relevant flux spectra, defined as follows. We consider pushing the dissipation scales towards the extremes $k_{\min} \rightarrow 0$ and $k_{\max} \rightarrow \infty$. If in this extremal case the integral defining an invariant, cf. (4.7), converges (or diverges) at the limit towards which that invariant is cascading, then the spectrum is said to have finite (infinite) capacity, respectively. It has been observed elsewhere that for finite capacity systems the cascading invariant fills out the inertial range in the wake of a self-similar front that reaches the dissipation scale in finite time, even in the extremal case, and then reflects back towards the forcing scale, with the Kolmogorov-Zakharov flux spectrum established behind the returning front. By contrast for infinite capacity systems the front takes infinite time to establish in the extremal case [157, 158, 41].

For the small and large-scale limits of the Schrödinger-Helmholtz equations we have found that the flux-carrying spectra are the Rayleigh-Jeans-like warm spectra, except for the nonlinear Schrödinger limit in 3D where they are Kolmogorov-Zakharov spectra. It is easy to check that for all these cases, the inverse particle cascade has finite capacity and the direct cascade has infinite capacity. We therefore expect that in an evolving system the inverse cascade will resemble the stationary spectra we have discussed, and that these spectra will be established in finite time, but will have parameters (μ and T in the warm case) that vary with time. As for the direct cascade, for an unforced system there is always a k_{\max} sufficiently remote that the energy in any initial condition is insufficient to fill the cascade spectrum. Therefore we do not expect that the direct energy cascade spectrum will be realised generically in systems evolving according to (4.1), although we might expect to see the cascade when k_{\max} is small enough, and the initial condition contains enough energy to act as a reservoir with which to fill the cascade spectrum.

Our hypotheses above regarding the time-evolving case are in broad agreement with numerical results in the recent study of the 3D Schrödinger-Newton equations by Levkov *et al.* [148]. They show by direct numerical simulation that, starting from a statistically homogeneous random field, the formation of coherent structures is preceded by a kinetic evolution, after which the structures become inhomogeneous due to a gravitational Jeans instability (the latter collapsed structures are what they call a condensate and the condensation time they report is the time of collapse, terminology we shall adhere to while comparing our study to theirs). Moreover, they argue that this kinetic evolution is governed not by pure flux spectra of Kolmogorov-Zakharov type, but rather by a process of thermalisation. Their conclusion entirely agrees with the scenario of large-scale structure formation via a warm cascade, but the theory we have developed in this work suggests an explanation that is different from the interpretation given in [148].

First, we can quantitatively demonstrate agreement between the wave turbulence theory of the work in this chapter and the numerics of Ref. [148] by estimating the characteristic timescale $\tau_{\text{kin}} \sim N/|\text{Coll}[n_{\mathbf{k}}]|$ over which Eq. (4.6) acts, where N is a typical value of the spectrum and $\text{Coll}[n_{\mathbf{k}}]$ is the right-hand side of (4.6), whose size is estimated in Appendix 4.B, Eq. (4.40). Taking values from the Gaussian initial spectrum of [148] we obtain a characteristic kinetic timescale of $\tau_{\text{kin}} \sim 4.3 \times 10^5$ in dimensionless units. This compares favourably to the condensation timescale of 1.08×10^6 reported in [148] for this initial condition: large-scale homogeneous structure forms over a timescale of roughly $2\tau_{\text{kin}}$ before a gravitational instability collapses this structure into a compact object. This lends credence to our kinetic equation capturing the essence of the condensation processes examined by Levkov *et al.* Furthermore they give timescale estimates for kinetic condensation in dimensional units for two models of self-gravitating bosons, which links our results to astrophysically relevant processes.

The points of difference between this study and Ref. [148] lie in the nature of the kinetic equations that are used in each. Levkov *et al.* derive a Landau-type differential kinetic equation by assuming that only boson-boson interactions that are strongly nonlocal in physical space contribute to the dynamics, which leads to small-amplitude scattering, an assumption that becomes more accurate at higher energies. They also imply that the lack of Kolmogorov-Zakharov cascades is due to the nonlocality of the system. By contrast our kinetic equation is derived without restriction to strong nonlocality, and is valid at arbitrary energies. Importantly, we attribute the lack of Kolmogorov-Zakharov cascades to the fact that they give the wrong flux directions, rather than the effects of nonlocality.

Additionally, when we reduce our kinetic equation (4.6) to the differential approximation model (4.15), the latter is explicitly constructed to keep the general Rayleigh-Jeans spectrum (4.11) as a stationary solution. However the only thermodynamic spectrum that solves the differential kinetic equation in Ref. [148] is the energy equipartition spectrum: (4.11) with $\mu = 0$. The low-energy part of the general Rayleigh-Jeans spectrum is excluded from their solution, yet we argue that this is the part responsible for the dynamical inverse cascade of particles that builds large-scale structure. Despite this, at the condensation time Levkov *et al.* observe excellent agreement between the spectrum obtained by direct numerical simulation of (4.3), the spectrum obtained by evolving their kinetic equation, and the low-energy part of the energy equipartition spectrum.

The agreement with the energy equipartition spectrum at the condensation time we explain by noting that $\mu = 0$ is indeed the criterion for condensation in the local Eq. (4.2) [20], and the arguments are sufficiently general that this criterion should apply universally. As mentioned above, we conjecture that the time-evolving

spectra might be Rayleigh-Jeans-like, with time-dependent thermodynamic parameters. As the system evolves towards the condensation time we expect to see $\mu(t)$ shrink to 0, leaving only the energy equipartition spectrum at the condensation time, as observed in [148]. The deviation of the observed spectrum from the thermodynamic one at high energies might be related to the infinite capacity of the direct warm cascade spectrum, meaning that the cascade may have had insufficient time to fill out at the highest frequencies, as mentioned above. Indeed Levkov *et al.* make reference to this part of the spectrum having a slow thermalisation timescale.

Thus, we summarise that our kinetic equation and its differential approximation is more general than that of Ref. [148], in terms of not being restricted to highly nonlocal interactions, and containing the general Rayleigh-Jeans spectrum that could explain more features of the evolution in the four-wave kinetic regime. Clearly further work is needed to explore and test these hypotheses.

4.5.2 Outlook for wave turbulence in Schrödinger-Helmholtz systems

We now speculate on what further perspectives wave turbulence could bring to the astrophysical and optical systems to which Eqs. (4.1) apply. Focusing first on the astrophysical application, our results suggest that the first process that starts to accumulate a condensate of dark matter particles at large scales in the early universe is an unsteady weakly nonlinear evolution that bears the hallmark of a warm dual cascade. Following this initial phase of condensation the subsequent evolution would follow the same broad lines as has already been documented in the literature, namely that gravitational collapse into a collection of virialised 3D spheroidal haloes will ensue [148, 120].

We also conjecture that wave turbulence may have much to say regarding certain other details that have already been noted. For example, the structure of haloes has been reported as a solitonic core that is free of turbulence surrounded by a turbulent envelope [119]. The exclusion of turbulence from the core is reminiscent of the externally trapped defocusing nonlinear Schrödinger Eq. (4.2), where wave turbulence combined with wavepacket (Wentzel-Kramers-Brillouin) analysis predicts the refraction of Bogoliubov sound waves towards the edges of the condensate, where transition from the three-wave Bogoliubov wave turbulence to four-wave processes could occur [8]. On the other hand the virialisation of haloes suggests a condition of critical balance where the linear propagation and nonlinear interaction timescales of waves are equal scale by scale. In that case the weak wave turbulence described here is not applicable and new spectral relations must be found based on the critical balance hypothesis [3, 159].

After the formation of haloes the next step of the evolution will be their

mutual interaction. As mentioned in Sec. 4.2.3, in nonlinear optics experiments and simulation of Eqs. (4.3) in one dimension (with six-wave interactions taken into account to break the integrability of the system), it has been observed that a random field creates a condensate via the dual cascade, which then collapses into solitons. These solitons then interact via the exchange of waves and finally merge into one giant soliton that dominates the dynamics [22, 21]. It seems plausible that the same phenomenology might carry over to the Schrödinger-Helmholtz equations, and into higher spatial dimensions.

Indeed, in cosmological simulations of binary and multiple halo collisions, scattering events, inelastic collisions, and mergers are all observed [119, 160–162]. Following such events, subsequent virialisation of the products involves ejection of some of the mass of the haloes [163, 164]. A detailed study of these processes should consider both the weakly nonlinear wave component and the strongly nonlinear haloes, and how the two components interact. Numerical studies could obtain effective collision kernels for those interactions in order to develop a kinetic equation for the “gas” of haloes that results from the collapse of a condensate. We note that work has been done in this spirit in Ref. [162] but without detailed consideration of the wave component. In our opinion it is crucial to incorporate wave turbulence into the study of the Schrödinger-Helmholtz model to uncover the full richness of the behaviour that this system manifests.

Finally, we expect that all the processes outlined above in the 3D astrophysical case—condensation via the dual cascade, fragmentation by modulational instability, soliton formation, and soliton interaction/merger via the exchange of weakly nonlinear waves—will be qualitatively the same in 2D. This makes them all amenable to direct observation by nonlocal nonlinear optics experiments. As mentioned in Sec. 4.2.2.2 theoretical [135, 136] and experimental [133, 134] comparisons have been made between astrophysical phenomena and experiments in thermo-optic media. To observe the wave turbulence cycle of condensation, collapse, and soliton interaction that we describe here one could also look to using nematic liquid crystals and modifying the one-dimensional experiments of [22, 21] to 2D. Any such experiment would need to have fine control over losses and nonlinearity strength in order to keep within the wave turbulence regime while the condensate is being built up. Liquid crystals are an attractive optical medium in this respect due to several inherently tunable parameters [165] that would assist in achieving conditions relevant to wave turbulence studies.

4.A Appendix: Relation between the cosmological constant and the Jeans swindle

In Sec. 4.2.2.3 we motivated the inclusion of a local term in Eq. (4.1b) in the dark matter application as representing a cosmological constant [137], and asserted that this is equivalent to using the “Jeans swindle”. In this Appendix we expand on this statement.

Eq. (4.3b) is well-posed for spatially infinite domains in which the support of $\rho(\mathbf{x}) = |\psi(\mathbf{x})|^2$ is compact, but if one seeks an equilibrium with spatially-constant V and ρ the only solution is the trivial null solution (an empty domain). The Jeans swindle [138] is the *ad hoc* replacement of V in Eq. (4.3a) with \tilde{V} that solves $\nabla^2 \tilde{V} = \gamma \tilde{\rho}$, where the tildes refer to fluctuations of quantities about a nonzero equilibrium, whose existence is entirely paradoxical. In a periodic domain $\Omega = \mathbb{T}_L^d$ of side L the equivalent problem is that Eq. (4.3b) can only be satisfied when Ω is empty, as can be seen by integrating over Ω , and using the divergence theorem and the periodic boundary conditions. The Jeans swindle is then implemented by replacing (4.3b) with

$$\nabla^2 \tilde{V} = \gamma (\rho - \langle \rho \rangle_\Omega) \quad (4.29)$$

where the box average of the number density $\langle \rho \rangle_\Omega = L^{-d} \int_\Omega \rho \, d\mathbf{x}$ is the equilibrium solution, and one solves only for \tilde{V} .

It is shown in Ref. [137] in the infinite-domain case that the Jeans swindle can formally be justified by considering the Helmholtz-like Eq. (4.1b) instead of Eq. (4.3b), as the former is well-posed without the restriction of the right-hand side needing to integrate to zero, and then taking the limit $\Lambda \rightarrow 0$. For the case of the periodic boundary we simply note that averaging (4.1b) gives $\langle V \rangle_\Omega = -\gamma \langle \rho \rangle_\Omega / \Lambda$. Substitution back into (4.1b) and writing $V = \tilde{V} + \langle V \rangle_\Omega$ recovers Eq. (4.29) in the limit $\Lambda \rightarrow 0$.

4.B Appendix: Wave turbulence in inhomogeneous systems

In the main body of this chapter we have applied the theory of weak wave turbulence to the Schrödinger-Helmholtz system, and described the initial stage of wave condensation via the dual cascade in a forced-dissipated setup. Crucial to this analysis is the assumption that the system is statistically spatially homogeneous, as only then can the dynamical variables, such as the spectrum and linear frequency, be characterised solely by time or axial distance t and wavenumber \mathbf{k} . However for inhomogeneous systems these quantities may vary with spatial position \mathbf{x} . This brings into play physical effects that are not present in homogeneous systems and

that are described by a different dynamical equation. In this Appendix we discuss the extension of wave turbulence theory to inhomogeneous systems and make simple estimates of the conditions under which the processes outlined in this chapter will be the dominant dynamical processes.

To take into account inhomogeneities of the wave field we define a local spectrum that can now vary with spatial position, with characteristic spatial scale D , via the Wigner transform of the $\psi(\mathbf{x}, t)$ field [166]:

$$n_{\mathbf{k}}(\mathbf{x}, t) = \int \langle \psi(\mathbf{x} - \mathbf{y}/2, t) \psi^*(\mathbf{x} + \mathbf{y}/2, t) \rangle e^{-i\mathbf{y} \cdot \mathbf{k}} d\mathbf{y}. \quad (4.30)$$

Let K be a characteristic wavenumber associated with the spectrum. If $DK \gg 1$ a Wentzel-Kramers-Brillouin analysis gives the following Vlasov-like equation of motion for the local spectrum (see, e.g., [166, 167, 70, 168–171, 148]):

$$\frac{\partial n_{\mathbf{k}}}{\partial t} + \nabla_{\mathbf{k}} \tilde{\omega}_{\mathbf{k}} \cdot \nabla_{\mathbf{x}} n_{\mathbf{k}} - \nabla_{\mathbf{x}} \tilde{\omega}_{\mathbf{k}} \cdot \nabla_{\mathbf{k}} n_{\mathbf{k}} = \text{Coll}[n_{\mathbf{k}}]. \quad (4.31)$$

The term $\text{Coll}[n_{\mathbf{k}}]$ on the right-hand side of Eq. (4.31) is the collision integral of the wave kinetic equation (4.6) which describes spectral evolution via nonlinear wave interactions.⁸

The left-hand side of (4.31) is the Liouville operator describing the motion of wavepackets through phase (\mathbf{k}, \mathbf{x}) space, in which trajectories are given by Hamilton's equations. The latter are $\partial_t \mathbf{x} = \nabla_{\mathbf{k}} \tilde{\omega}_{\mathbf{k}}$ and $\partial_t \mathbf{k} = -\nabla_{\mathbf{x}} \tilde{\omega}_{\mathbf{k}}$, where the effective Hamiltonian is the renormalised dispersion relation $\tilde{\omega}_{\mathbf{k}}$ which, as we shall shortly discuss, is a function of the local spectrum. If the collision integral vanishes, wavepackets move ballistically in phase space in a manner that conserves waveaction. As they move across the inhomogeneous wave field, e.g., through a turbulent patch, the amplitude of the spectrum changes and therefore $\tilde{\omega}_{\mathbf{k}}$ changes. In this manner wavepackets can be distorted as they move, leading to a redistribution of the spectrum and an exchange of energy between the wavepackets and the background turbulence [167, 70, 169, 170].

The distortion of wavepackets brings about two effects: either wavepackets are dispersed [second term on the left-hand side of (4.31), noting that $\nabla_{\mathbf{k}} \tilde{\omega}_{\mathbf{k}} = \mathbf{v}_{\mathbf{g}}$, the group velocity], or in the case of a focusing nonlinearity such as the gravitational one considered in this chapter, the wavepacket can become unstable and bunch up in physical space (third term). As we justify below, these collapsing events are an incoherent version of the monochromatic modulational instability, and lead to the formation of compact strongly-nonlinear structures, studied in deep water gravity

⁸Note that in $\text{Coll}[n_{\mathbf{k}}]$ the spectrum $n_{\mathbf{k}}$ is now the local spectrum defined in (4.30). The frequency resonance condition $\delta(\omega_{3\mathbf{k}}^2)$ can be taken between the linear frequencies of waves in the tetrad as the nonlinear frequency (4.33) gives higher-order corrections to $\text{Coll}[n_{\mathbf{k}}]$ that are not significant during the time over which the wave kinetic equation is valid.

waves in Ref. [170], and in 1D local [169] and nonlocal optical turbulence [172]. These collapses were also observed in the 3D Schrödinger-Newton equations in their dark matter context [148], after a period of evolution governed by four-wave kinetics, such as we describe in the main body of this chapter (see Sec. 4.5.1). It is thus important to distinguish when processes associated with inhomogeneity will occur faster than processes due to four-wave interaction. Below we derive conditions to evaluate which of these two types of processes dominate the dynamics.

For any nonlinear equation with even-wave interactions of the type $M \leftrightarrow M$, such as the Schrödinger-Helmholtz equations (of type $2 \leftrightarrow 2$), the linear dispersion relation $\omega_{\mathbf{k}}$ is modified by the nonlinearity [3]. This can be seen in Eq. (4.5c) where the diagonal terms in the nonlinear Hamiltonian give a contribution whose effect is to shift the linear frequency by ω_{NL} , i.e., the dispersion relation is renormalised to

$$\tilde{\omega}_{\mathbf{k}} = \omega_{\mathbf{k}} + \omega_{\text{NL}}. \quad (4.32)$$

This frequency shift is the leading effect of the nonlinearity, and does not lead to interaction between wave modes.

For the Schrödinger-Helmholtz equations the nonlinear frequency correction is

$$\omega_{\text{NL}}(\mathbf{k}) = -\gamma \sum_{\mathbf{k}_1} \left(\frac{1}{|\mathbf{k} - \mathbf{k}_1|^2 + \Lambda} + \frac{1}{\Lambda} \right) |\psi_{\mathbf{k}_1}|^2 \quad (4.33)$$

and depends on both \mathbf{k} and the spectrum. When the spectrum is spatially dependent, as in (4.30), then the renormalised frequency also varies in space, leading to the distortion of wavepackets described above.

We can conveniently estimate the size of ω_{NL} in the case of weak inhomogeneity $DK \gg 1$. Then in physical space Eq. (4.33) is replaced by

$$\omega_{\text{NL}}(\mathbf{x}, t) = -\gamma \int G_{\ell_*}(\mathbf{x} - \mathbf{y}) \mathcal{N}(\mathbf{y}, t) d\mathbf{y} \quad (4.34)$$

[171], where $\mathcal{N}(\mathbf{x}, t) = (2\pi)^{-d} \int n_{\mathbf{k}}(\mathbf{x}, t) d\mathbf{k} = \langle |\psi(\mathbf{x}, t)|^2 \rangle$ is the average local level of fluctuations, whose typical amplitude we denote N . Here $G_{\ell_*}(\mathbf{x} - \mathbf{y})$ is the Green's function for Eq. (4.1b). It is useful to extract the explicit dependence on $\ell_* = 1/\sqrt{\Lambda}$ by the scaling space as $\mathbf{x} = \ell_* \boldsymbol{\xi}$ and defining $G(\boldsymbol{\xi})$ as the normalised Green's function satisfying $(\nabla_{\boldsymbol{\xi}}^2 - 1)G(\boldsymbol{\xi}) = \delta^{(d)}(\boldsymbol{\xi})$, and that integrates to unity. Doing so we find $G(\boldsymbol{\xi}) = \ell_*^{d-2} G_{\ell_*}(\mathbf{x})$. (For self-consistency, passing to the local limit requires that $\tilde{\gamma} = \gamma \ell_*^2 \rightarrow \text{const.}$) We approximate the convolution in (4.34) by multiplying the average fluctuation level N with the volume of the d -ball of size ℓ_* . Neglecting geometrical factors and the sign we obtain

$$\omega_{\text{NL}} \sim 2\gamma \ell_*^2 N. \quad (4.35)$$

For $l_*K \ll 1$ Eq. (4.33) reduces to the well-known value for the nonlinear Schrödinger equation $-2\tilde{\gamma} \sum_{\mathbf{k}} \langle |\psi_{\mathbf{k}}|^2 \rangle$, so the estimate in (4.35) becomes exact.

We now provide estimates on the various terms in Eq. (4.31) in order to determine when the wavepacket collapse due to inhomogeneity will dominate over either dispersion, or four-wave nonlinear interactions.

4.B.1 Incoherent modulational instability

We assume an isotropic spectrum that has spectral width ΔK about the representative wavenumber K . Thus, in terms of the measure of the average fluctuations N and neglecting geometric factors, the spectrum can be estimated as

$$n_{\mathbf{k}} \sim \frac{N}{K^{d-1} \Delta K}. \quad (4.36)$$

With estimates (4.35) and (4.36) we can estimate the sizes of the second and third terms on the left-hand side of (4.31). The second term describes the dispersion of wavepackets, which is a stabilising process. Noting that the linear frequency $\omega_{\mathbf{k}} = k^2$, that ω_{NL} is \mathbf{k} -independent, and that the inhomogeneity of the spectrum has characteristic size D , we estimate

$$\nabla_{\mathbf{k}} \tilde{\omega}_{\mathbf{k}} \cdot \nabla_{\mathbf{x}} n_{\mathbf{k}} \sim \frac{N}{DK^{d-2} \Delta K}. \quad (4.37)$$

Turning to the focusing term, we note that $\nabla_{\mathbf{x}} \tilde{\omega}_{\mathbf{k}} = \nabla_{\mathbf{x}} \omega_{\text{NL}}$ as the linear frequency is \mathbf{x} -independent. The spectrum varies over length D , however the convolution in (4.34) “smears out” the variations of the spectrum over the length ℓ_* , meaning that ω_{NL} will vary over a length $\max(D, \ell_*)$. Additionally the spectrum has a \mathbf{k} -space width of ΔK by assumption, so we can approximate the gradient in $\nabla_{\mathbf{k}} n_{\mathbf{k}}$ by $1/\Delta K$. Bringing these considerations together, we estimate the focusing term as

$$\nabla_{\mathbf{x}} \tilde{\omega}_{\mathbf{k}} \cdot \nabla_{\mathbf{k}} n_{\mathbf{k}} \sim \frac{\gamma \ell_*^2 N^2}{\max(D, \ell_*) K^{d-1} (\Delta K)^2}. \quad (4.38)$$

Comparing (4.37) and (4.38) we find that wavepacket collapse into incoherent solitons is favoured over wave dispersion when

$$\frac{D}{\max(D, \ell_*)} \frac{\tilde{\gamma} N}{K \Delta K} > 1. \quad (4.39)$$

To justify the assertion that these collapse events are the result of an incoherent modulational, (or Benjamin-Feir) instability, we note that the latter has been extensively studied in the 1D local nonlinear Schrödinger equation, for example in the context of extreme ocean waves [173]. In the oceanic literature an important dimensionless number has been identified that controls the tendency for polychro-

matic wavepackets to destabilise and form strongly nonlinear structures such as rogue waves: the Benjamin-Feir Index (BFI) [170, 174]. In the notation we have established in this Appendix, this is

$$BFI = \sqrt{\frac{\tilde{\gamma}N}{K^2}},$$

with the modulational instability triggering the formation of nonlinear structures when $BFI > 1$ [174]. However our condition (4.39) for inhomogeneity on scales greater than the nonlocality length ($D > \ell_*$) and with a spectrum whose width is of the same order as the characteristic wavenumber ($\Delta K \sim K$) is just $BFI^2 > 1$ for wavepacket collapse. Thus we conclude that the ratio on the left-hand side of (4.39) contains the same physics as the BFI, so we identify the third term in Eq. (4.31) with modulational instability and wavepacket collapse. Note that (4.39) is valid for both local and nonlocal nonlinearities, indicating that our condition is a generalisation of the BFI to the nonlocal case, and for the spectra of arbitrary width ΔK .

4.B.2 Kinetic regime

The derivation of the wave kinetic equation requires that the nonlinearity is small in the original equation of motion. Quantitatively this means that the linear wave period is much smaller than the characteristic timescale for nonlinear evolution [3], or in other words $|\omega_{\mathbf{k}}n_{\mathbf{k}}| \gg |\text{Coll}[n_{\mathbf{k}}]|$. We estimate the collision integral as

$$\text{Coll}[n_{\mathbf{k}}] \sim \frac{\gamma^2 N^3}{(K^2 + 1/\ell_*^2)^2 K^{d+2}}, \quad (4.40)$$

giving the first condition for wave turbulence

$$(\gamma N)^2 \ll \frac{(K^2 + 1/\ell_*^2)^2 K^5}{\Delta K}. \quad (4.41)$$

In inhomogeneous domains, wave turbulence processes will only dominate if in Eq. (4.31) the collision integral is larger than the focusing term that leads to wavepacket collapse, i.e., $|\text{Coll}[n_{\mathbf{k}}]| > |\nabla_{\mathbf{x}}\tilde{\omega}_{\mathbf{k}} \cdot \nabla_{\mathbf{k}}n_{\mathbf{k}}|$. This gives a second condition for wave turbulence when the kinetic regime dominates over wavepacket collapse:

$$\frac{1}{\max(D, \ell_*)} \frac{\ell_*^2 (K^2 + 1/\ell_*^2)^2 K^3}{\gamma N (\Delta K)^2} < 1. \quad (4.42)$$

We now examine what our conditions (4.39), (4.41) and (4.42) imply about the applicability of the kinetic regime.

4.B.2.1 Kinetic regime in the local limit

For Eq. (4.31) to be valid, and for the nonlinearity to be local, we have $D \gg 1/K \gg \ell_*$. In this limit, condition (4.41) becomes $(\tilde{\gamma}N)^2 \ll K^5/\Delta K$, and the condition for the modulational instability to be stable [i.e., (4.39) with the ordering reversed] is $\tilde{\gamma}N < K(\Delta K)$. If the spectrum is broad ($\Delta K \sim K$) then the conditions for weak nonlinearity and modulational stability become identical, $(\tilde{\gamma}N)^2 \ll K^4$, which agrees with the physical intuition that for weak wave turbulence processes one must not have the spectrum collapsing into strongly nonlinear objects.

In the local limit condition (4.42) becomes $K^3/D(\Delta K)^2 < \tilde{\gamma}N$. Thus for wave turbulence to be the dominant process the nonlinearity must satisfy the double inequality

$$\frac{K^3}{D(\Delta K)^2} < \tilde{\gamma}N < \min\left(K(\Delta K), \frac{K^{5/2}}{(\Delta K)^{1/2}}\right). \quad (4.43)$$

These inequalities are violated when either the spectrum is too narrow, or the inhomogeneity length is too short. If ΔK is small then no matter how large D is, the system is still vulnerable to modulational instability via the first term on the right-hand side of (4.43), and if the spectrum is broad but $D \rightarrow 1/K$ the system again becomes modulationally unstable from the left-hand side of (4.43), as both sides of the inequality approach the same value.

We thus conclude that wave turbulence in the Schrödinger-Helmholtz equations in their local limit requires that the spectrum is sufficiently broad everywhere, *and* that the inhomogeneity length of the spectrum is sufficiently long.

4.B.2.2 Kinetic regime in the nonlocal limit

Validity of (4.31) and a nonlocal nonlinearity both require $D, \ell_* \gg 1/K$. We now consider the ordering $\ell_* \sim D$ or $\ell_* \gg D$. These give $K^6/(\Delta K)^2 \ll \gamma N$ for condition (4.42), whereas condition (4.41) becomes $(\gamma N)^2 \ll K^9/\Delta K$. For a broad spectrum this means that γN is both much smaller and much greater than K^8 , which is impossible (the violation of the inequalities is worse for a narrow spectrum).

We conclude that nonlocal wave turbulence is not possible when $\ell_* \sim D$ or $\ell_* \gg D$. Instead, The ordering $D \gg \ell_* \gg 1/K$ allows for wave turbulence for sufficiently large D .

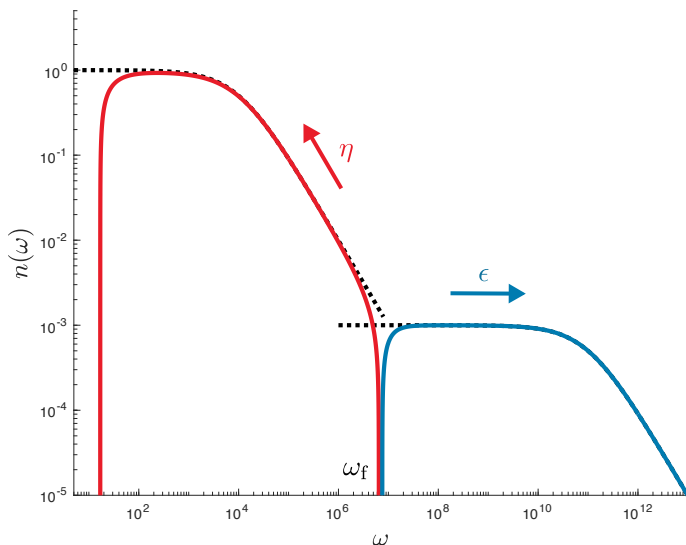


Figure 4.6: Double-peaked spectra representing a solution of the differential approximation model where particles are swept upscale (red curve) and energy downscale (blue curve) from forcing at ω_f at a zero value for the spectrum. Black dashed lines represent the two different thermodynamic spectra that match the middle of the two peaks of the spectrum. For parameters see main text.

4.C Appendix: Bimodal cascade spectra in the differential approximation model

In Sec. 4.4.2 we noted that Eqs. (4.21) and (4.24) permitted the deviation away from the Rayleigh-Jeans spectrum $\theta(\omega)$ to become large at both low and high frequencies for both the inverse and direct cascades. This led to the intriguing possibility that we could have a warm inverse cascade spectrum, which carries only particles, arising from the cutoff at ω_+ , becoming large at intermediate ω and terminating at the cutoff at ω_{\min} . Similarly one could imagine that the warm direct cascade of energy might exist between ω_- and ω_{\max} , terminating at compact fronts at those frequencies. For both of these to be realised the combined spectrum would have two maxima. The frequency where the two cascades met would then be the forcing scale, i.e., $\omega_f = \omega_+ = \omega_-$, and the forcing would be such that all the particles were swept upscale and the energy downscale with the spectrum at ω_f vanishing. This scenario is illustrated in Fig. 4.6.

(To obtain the direct cascade, shown in blue in Fig. 4.6, we have integrated (4.18) forwards to ω_{\max} and backwards to ω_- from a spectrum and its derivative matching Eq. (4.11) at $\omega = 10^{12}$ with $T = 10^8$ and $\mu = 10^{11}$. Likewise to obtain the inverse cascade shown in red, we integrated (4.19) backwards to ω_{\min} and forwards to ω_+ from a spectrum and its derivative matching Eq. (4.11)

at $\omega = 10^5$ with $T = \mu = 10^4$. The fluxes were $\eta = -150$ and $\epsilon = \omega_f^2 |\eta|$ with $\omega_f \approx \omega_- \approx \omega_+ = 6.44 \times 10^6$. In Fig. 4.6 we have chosen parameters to slightly separate ω_- and ω_+ for clarity.)

We argue here that this scenario, although technically possible within the differential approximation, is implausible for more realistic models like the wave kinetic equation (4.6) or the original dynamical equation itself [the Schrödinger-Helmholtz system (4.1) or its limits]. Note that this possibility is common to all the warm cascade spectra we discuss here. Following on from Sec. 4.4.2 we take the concrete example of the Schrödinger-Newton model in 3D, but similar arguments can be made for either the Schrödinger-Newton model or nonlinear Schrödinger model in 2D. The argument proceeds by seeking compatibility with wide inertial ranges, $\omega_{\min} \ll \omega_+$ for the inverse cascade and $\omega_- \ll \omega_{\max}$ for the direct cascade.

First considering the inverse particle cascade, Eq. (4.21) and the requirement that there exists a range of $\omega > \omega_{\min}$ for which $\theta(\omega)$ is small, gives the ordering $\omega_{\min} \ll \mu$. This ordering gave the relation (4.22) between flux and thermodynamic parameters. Now, a cutoff at ω_+ implies that in that vicinity the deviation must become comparable to the other terms in the denominator of the warm spectrum (4.20). We set $\theta(\omega_+) \sim \mu + \omega_+$ here. If we then let either $\omega_+ \sim \mu$ or $\omega_+ \ll \mu$ and substitute (4.22) then we obtain $\omega_+ \sim \omega_{\min}$, which is not compatible with a wide inertial range. A scale separation between forcing and dissipation is only possible if we have the ordering $\omega_{\min} \ll \mu \ll \omega_+$ for the inverse cascade.

Next we consider the direct energy cascade. Eq. (4.24) for the deviation, and the requirement that it must be small for some $\omega < \omega_{\max}$ gives the ordering $\mu \ll \omega_{\max}$. From this we obtained the relation (4.25). If we have a low-frequency cutoff at ω_- then near there it must match the other terms in the denominator of (4.20). We set $\theta(\omega_-) \sim \mu + \omega_-$ and consider $\omega_- \sim \mu$ and $\omega_- \gg \mu$. Substituting (4.25) gives $\omega_- \sim \omega_{\max}$ for these two cases, which is not compatible with a wide inertial range. Therefore for the direct cascade we must have $\omega_- \ll \mu \ll \omega_{\max}$.

Thus if we seek a double-peaked “flux-sweeping” spectrum with the inverse and direct warm cascades joining at ω_f and the spectrum being zero there, then the cascades could not share the same thermodynamic parameters, as μ must lie deep within the inertial ranges of both cascades. Indeed, to realise such a spectrum in Fig. 4.6 we have had to choose very different sets of thermodynamic parameters for each inertial range. This is technically possible within the differential approximation, as each steady cascade is described by a second order ordinary differential Eq. (4.18) or Eq. (4.19), which only requires for its solution the value of the spectrum and its derivative at the forcing scale.

However when considering a fuller model one must consider a more realistic forcing protocol, for example in simulations setting the spectrum to be drawn from

a particular distribution at a certain level in a narrow range around ω_f at each timestep. This sets the amplitude and derivative of the spectrum at the forcing scale at the same prescribed value for both cascades, corresponding to prescription of the thermodynamic parameters T and μ that both cascades share. It is therefore hard to imagine a scenario of forcing which could realise the double-peaked spectrum in a more realistic model like Eqs.(4.1) or Eq.(4.6). For example the four-wave collision integral in Eq.(4.6) has the effect of smoothing out irregularities in the spectrum, and so we expect that any stationary solution will be at least continuous and differentiable. In this respect, this discussion stands as a cautionary example that the differential approximation includes exotic solutions like the double-peaked spectrum of Fig. 4.6, that a more physically relevant model would not permit.

Chapter 5

The Schrödinger-Helmholtz equation in 2D: direct numerical simulations

5.1 Chapter summary and organisation

In order to verify the theoretical predictions of chapter 4, of large-scale structure formation via a turbulent inverse cascade in the SHE, it is necessary to perform direct numerical simulations. In this chapter we report preliminary results in this direction, for the 2D SHE. This is work that is still in progress, and further work is necessary in order to quantitatively demonstrate the validity of the theory developed in chapter 4. Nevertheless, our preliminary results appear to point favourably towards the general scenario of a warm dual cascade, with the inverse particle cascade giving rise to the formation of a coherent structure.

In section 5.2 we give an overview of the numerical methods employed in the code we have used in the work of this chapter. Then in section 5.3 we present the results generated by this code that provide some evidence for the warm cascade, and demonstrate condensation. We end in section 5.4 with a discussion of the results, and outline the future research directions that could be followed using this code to explore the WT behaviour of the 2D SHE.

5.2 Numerical methods

The simulations reported in this section were carried out using a pseudospectral code provided by Jason Laurie, with subsequent development by this author. In this section we outline the important aspects of this code.

We seek a solution $\psi(\mathbf{x}, t)$ to our model equation, the SHE,

$$i\partial_t\psi + \nabla^2\psi - V[|\psi|^2]\psi = 0, \quad (5.1a)$$

$$\nabla^2V - \Lambda V = \gamma|\psi|^2 \quad (5.1b)$$

in \mathbb{T}_L^d , the periodic box of size L in d dimensions. Here we choose $d = 2$, making this work more relevant to applications of the SHE in nonlinear optics. (The 3D SHE has been studied in the astrophysics community using pseudospectral methods [119–121, 162], similar to those used here, but not in the WT context.) We choose $L = 2\pi$ to make the wavenumber spacing simply $\Delta k = 2\pi/L = 1$ in each direction. We solve $\psi(\mathbf{x}, t)$ on a square spatial grid with N grid points in the x and y directions (i.e. $N = N_x = N_y$). As we will see, the pseudospectral method involves transforming back and forth between real and Fourier space, so N is also the number of Fourier modes in each direction (i.e. $k_x, k_y = -N/2, \dots, N/2 - 1$ for even N).

5.2.1 Pseudospectral methods for nonlinear partial differential equations

Pseudospectral methods are standard numerical techniques used in the study of WT, and turbulence in general [175, 176]. The methods are appropriate for simulation in simple domains, with periodic (or vanishing, or vanishing-derivative) boundary conditions. This makes it possible to decompose the smooth function $\psi(\mathbf{x})$ into a sum of spectral basis functions, whose coefficients are found numerically. As our domain $\mathbb{T}_{2\pi}^2$ is rectangular, we use a Fourier basis (2.11), enabling the Fourier coefficients $\psi_{\mathbf{k}}$ to be found using the FFTW [177] implementation of the Fast Fourier Transform (FFT) algorithm [178].

We outline the pseudospectral method for a general equation,

$$\frac{\partial}{\partial t}u(x, t) = \mathcal{L}u(x, t) + \mathcal{N}[u(x, t)], \quad (5.2)$$

in a one-dimensional domain for simplicity. The linear operator \mathcal{L} generally contains spatial derivatives, and \mathcal{N} is a nonlinear function of $u(x, t)$ and its derivatives. When x is promoted to a position vector we see that the equations studied in this thesis (2.1), (2.2), and (2.3) are manifestly of type (5.2).

The advantage of spectral methods is that the Fourier decomposition represents $u(x)$ as a sum of basis functions, i.e. globally. Spatial derivatives can then be obtained in the Fourier domain by the simple rule

$$\partial_x u(x) \rightarrow ik_x \hat{u}_k, \quad (5.3)$$

meaning that derivatives are also represented globally, as opposed to, say, finite

difference methods that represent derivatives using a truncated Taylor expansion, which is necessarily local. This gives the method exponential or “spectral” accuracy: with increasing grid number of grid points N , spectral methods converge faster than any finite algebraic power of N . Furthermore, the FFT algorithm enables the spectral coefficients \hat{u}_k to be found in $\mathcal{O}(N \log_2 N)$ time. Thus in principle, spectral methods offer both superior accuracy and speed compared to a generic finite difference method. In solving (5.2) we therefore calculate $\mathcal{L}u(x, t)$ by transforming $u(x)$ to Fourier space and calculating derivatives via (5.3).

5.2.1.1 Nonlinear term and de-aliasing

The “pseudo” in pseudospectral methods refers to how the nonlinear term \mathcal{N} is treated. Let us consider the specific case where \mathcal{N} involves the product of the fields $u(x)$ and $v(x)$. In terms of the Fourier decompositions of these fields, this product is

$$u(x)v(x) = \left(\sum_{k_1=-N/2}^{N/2-1} \hat{u}_1 e^{ik_1 x} \right) \left(\sum_{k_2=-N/2}^{N/2-1} \hat{v}_2 e^{ik_2 x} \right) = \sum_{k=-N}^{N-1} \hat{w}_k e^{ikx} \quad (5.4)$$

where $k = k_1 + k_2$, and

$$\hat{w}_k = \sum_{k'=-N/2}^{N/2-1} \hat{u}_{k-k'} \hat{v}_{k'}.$$

First we see that the Fourier coefficient \hat{w}_k of the product is the convolution of the fields \hat{u}_k and \hat{v}_k . This convolution has complexity $\mathcal{O}(N^2)$, which would be prohibitively expensive to solve in Fourier space. Instead, we use the inverse FFT, which again is an $\mathcal{O}(N \log_2 N)$ operation, to transform \hat{u}_k and \hat{v}_k back into x -space, where the fields can simply be multiplied pointwise, an $\mathcal{O}(N)$ operation.

Next, we see that the addition of wavenumbers makes the final sum in (5.4) over $2N$ modes rather than the original N . The nonlinearity has created higher harmonics that cannot be resolved if we maintain the original resolution N . If they are not accounted for then these higher harmonics outside the original range of resolution will be aliased back into lower harmonics inside the range. For example if mode $k = k_1 + k_2 > N/2$ then the amplitude of this mode will be unphysically added to the mode $k - N$. This represents an entirely unphysical “pollution” of the lower modes by the higher harmonics.

To account for this we must introduce a de-aliasing procedure that safely nullifies the higher harmonics that are generated by the nonlinearity. One possibility is to use the so-called three-halves method, in which one embeds the original fields \hat{u}_k^N, \hat{v}_k^N (where the superscript indicates the number of grid points in k or x space on which the fields are defined) into the central modes of new fields of size $M = 3N/2$.

The extra modes with $N/2 < |k| \leq M/2$ are sacrificial and initialised as zero at the start of each calculation of (5.4). The embedded fields \hat{u}_k^M, \hat{v}_k^M are then transformed into real space, with the fields $u^M(x), v^M(x)$ being defined on a spatial grid of size M . The fields are then multiplied in real space giving $w^M(x) = u^M(x)v^M(x)$. Transforming back into Fourier space, the high $|k|$ modes of \hat{w}_k^M contain spurious harmonics that have safely been captured in the sacrificial band. The modes in the range $|k| \leq N/2$ are then extracted to obtain the Fourier coefficients of the field \hat{w}_k^N . It is straightforward to show that for the quadratic nonlinearity (5.4), choosing $M = 3N/2$ keeps the spurious harmonics from being aliased back into the computational range of interest $|k| \leq N/2$.

For the actual problem of interest here, the 2D SHE, three-halves dealiasing is applied in both the x and y directions, embedding the computational $N \times N$ range into an $M \times M$ box. The nonlinearity of the SHE is cubic, and so the embeddings, back-and-forth transforms, and real-space multiplications are done twice, so that only quadratic multiplications are performed each time. This saves on embedding into a larger box, but also ensures that momentum is conserved [179].

5.2.2 Forcing and dissipation

To simulate the forced-dissipated setup described in chapter 4, we can include small-scale hyperviscosity and large-scale hypoviscosity into the linear operator in (5.1) so that in Fourier space it reads, for the SHE,

$$\hat{\mathcal{L}} = \underbrace{-ik^2}_{\text{linear dispersion}} - \underbrace{\nu k^{2p_\nu}}_{\text{hyper-viscosity}} - \underbrace{\alpha k^{2p_\alpha}}_{\text{hypo-viscosity}}. \quad (5.5)$$

The first term comes from the linear Laplacian in (5.1a) and gives the linear dispersion relation.

In the hyperviscosity term we choose a positive p_ν so that the hyperviscous dissipation ramps up rapidly with $|k|$, leading to rapid exponential decay of $\psi_{\mathbf{k}}$ for those modes. In the results presented here we have used $p_\nu = 8$.

Likewise in the hypoviscosity term in (5.5) one chooses a negative p_α to give dissipation at low $|k|$. (Although implemented in the code, we have not used hypoviscosity in the results presented here.)

Forcing is implemented via the Euler-Maruyama method, in a ring in \mathbf{k} -space $|k| = k_f \pm 1$. Each Fourier mode within this ring has stochastic noise added to it at each timestep (of length Δt),

$$\psi_{\mathbf{k}}(t + \Delta t) = \psi_{\mathbf{k}}(t) + A_f \sqrt{\frac{\Delta t}{2}} (\zeta + i\xi) \quad (5.6)$$

with noise amplitude A_f , and random variables ζ, ξ drawn from a normal distribution of mean zero and variance 1.

5.2.3 Time-stepping

The pseudospectral techniques outlined above give the RHS of (5.2) in the Fourier domain. We then integrate in time using the exponential time-differencing fourth-order Runge-Kutta (ETDRK4) method [180]. This involves solving for the linear part of (5.2) exactly using an integrating factor, writing

$$\hat{r}_k(t) = \hat{u}_k(t)e^{-\hat{\mathcal{L}}t},$$

so that in Fourier space equation (5.2) becomes

$$\partial_t \hat{r}_k(t) = e^{-\hat{\mathcal{L}}t} \hat{\mathcal{N}}[\hat{r}_k(t)e^{\hat{\mathcal{L}}t}]. \quad (5.7)$$

Equation (5.7) is then integrated forwards in time by means of a fourth order Runge-Kutta method.

Casting the dynamical equation this way alleviates the numerical stiffness introduced by the high spatial derivatives in the dissipation terms of $\hat{\mathcal{L}}$, which is where the highest derivatives occur in the problem.

For numerical stability the timestep Δt should be chosen so that

$$\omega_{\mathbf{k}} \times \Delta t < 2\pi \quad (5.8)$$

for every physical wave that we want to resolve in the problem. In our problem of interest, the 2D SHE, the physical waves are governed by the dispersion relation $\omega_{\mathbf{k}} = k^2$, and we choose to resolve every wave up to the maximum wavenumber in the $N \times N$ box, the corner mode $k = \sqrt{2(N/2)^2} = N/\sqrt{2}$.

5.3 Results on the freely-evolving and forced-dissipated 2D SHE

Using the code described in the previous section we have simulated the 2D SHE at resolution of $N_x = N_y = 128$. All our simulations were carried out with $\gamma = 1/2$ and $\Lambda = 1$, which puts them firmly in the Schrödinger-Newton limit of the SHE. These low-resolution results indicate a preliminary start to our investigations and clearly results need to be obtained at higher resolution in order to make our conclusions robust.

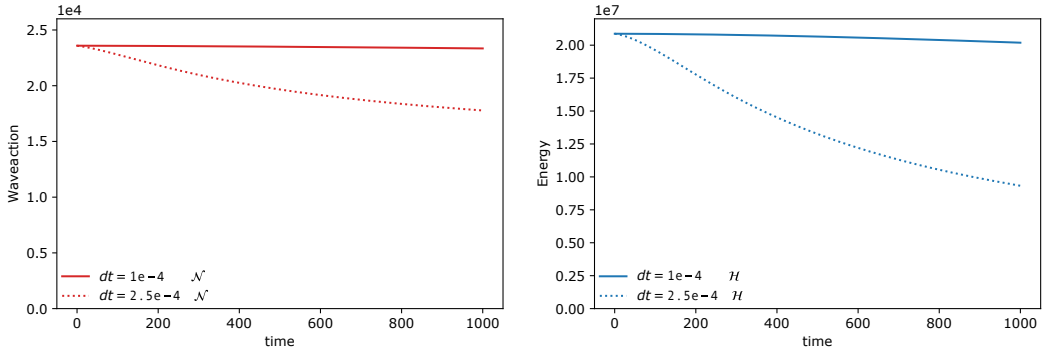


Figure 5.1: Time series of the total waveaction (left), and the total energy (right), for two freely-evolving runs with the same initial condition and two different timesteps.

5.3.1 Benchmarking: conservation of energy and waveaction

We began our discussion of WT by stating that equations of Schrödinger type conserve the total waveaction \mathcal{N} and energy \mathcal{H} . To check that our code has this property, we launched simulations with no forcing or dissipation, evolving from an initial condition

$$|\psi_{\mathbf{k}}| = \begin{cases} 10^4, & |k| = 32 \pm 4 \\ 0, & \text{otherwise} \end{cases} \quad (5.9)$$

and with random phases. This was evolved from $t = 0$ to $t = 1000$ in code units. We compare runs with two different timesteps, one with $\Delta t = 2.5 \times 10^{-4}$ and one with $\Delta t = 1.0 \times 10^{-4}$. Both choices satisfy the condition (5.8). The time series of the invariants are plotted in figure 5.1. It is clear that conservation of \mathcal{N} and \mathcal{H} is much better for $\Delta t = 1.0 \times 10^{-4}$ than for $\Delta t = 2.5 \times 10^{-4}$.

To investigate the loss of invariants from the system, we carried out a timestep convergence study. The relative global errors in the waveaction and energy are, respectively,

$$e_t(\mathcal{N}) = \max_t \frac{|\mathcal{N}(0) - \mathcal{N}(t)|}{\mathcal{N}(0)} \quad \text{and} \quad e_t(\mathcal{E}) = \max_t \frac{|\mathcal{E}(0) - \mathcal{E}(t)|}{\mathcal{E}(0)}.$$

As the ETDRK4 method we use here is fourth-order, we expect global errors in the solution ψ , and hence the errors $e_t(\mathcal{N})$ and $e_t(\mathcal{H})$, to be $\mathcal{O}((\Delta t)^4)$ functions of the timestep.

We launched five simulations from an identical realisation of the initial condition (5.9) with random phases, and ran them to $t = 50$ code units. Between the five simulations we progressively halved the timestep, from $\Delta t = 4.0 \times 10^{-4}$ down to 0.25×10^{-4} . We show the errors $e_t(\mathcal{N})$ and $e_t(\mathcal{H})$ from these runs and their dependence on the timestep in figure 5.2. We see that both errors are converging to zero as

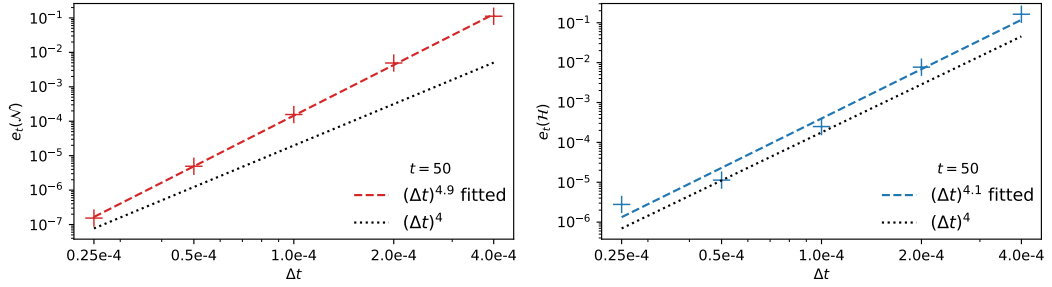


Figure 5.2: Dependence of the relative global waveaction (left) and energy (right) errors with timestep. The errors converge to zero as the timestep is reduced, at the empirical fitted rate stated, and indicated by the dashed line. For comparison, the expected convergence rate of $(\Delta t)^4$ is shown in by the black dotted line.

the timestep is reduced, with convergence rates $e_t(\mathcal{N}) \propto (\Delta t)^{4.9}$ and $e_t(\mathcal{H}) \propto (\Delta t)^{4.1}$ obtained by a least-squares fit. Thus both these errors are $\mathcal{O}((\Delta t)^4)$ as expected.

As the errors in \mathcal{N} and \mathcal{H} tend to zero in the expected way as Δt is reduced for the ETDRK4 method used, we conclude that the loss of invariants shown in figure 5.1 is entirely due to the numerical viscosity in the timestepping. In particular, on theoretical grounds we do not expect any effective damping from dealiasing. Recall from section 2.2.1 that the conservation of \mathcal{N} and \mathcal{H} was proved for the generalised NLS (and hence for the SHE) by differentiating the invariants with respect to time, and substituting the original equation of motion after an integration by parts. It is shown in [179] that quantities whose conservation relies on such an integration by parts are exactly conserved by Fourier-truncated pseudospectral schemes. Remarkably, this is the case with or without dealiasing.

5.3.2 Evolution of a freely-evolving simulation

We examine the simulation from section 5.3.1 with $\Delta t = 1.0 \times 10^{-4}$ that evolves freely from its initial condition 5.9. Figures 5.3(a) and (b) are snapshots of the physical-space field $|\psi(\mathbf{x})|$ at the initial and final time, respectively. In the second column of Figure 5.3 we show the state of the 1D-angle-integrated waveaction spectrum $n_k^{(1D)} = 2\pi k n_{\mathbf{k}}$ at several different times. The third column shows the spatio-temporal spectrum

$$|\hat{\psi}(k_x, \omega)|^2 = \left| \int \psi_{\mathbf{k}_0}(t) e^{-i\omega t} dt \right|^2, \quad (5.10)$$

calculated at the beginning (e) and end (f) of the simulation. In (5.10) we denote $\mathbf{k}_0 = (k_x, 0)$, i.e. $|\hat{\psi}(k_x, \omega)|^2$ is the spectrum of the space-and-time Fourier-transformed data, with the spatial transform along the $k_y = 0$ slice of \mathbf{k} -space.¹

¹Thus to construct the spatio-temporal spectrum (5.10), we take the $k_y = 0$ slices of the $\psi_{\mathbf{k}}$ field every few timesteps: at a high enough rate as to resolve periods of the shortest wave of interest

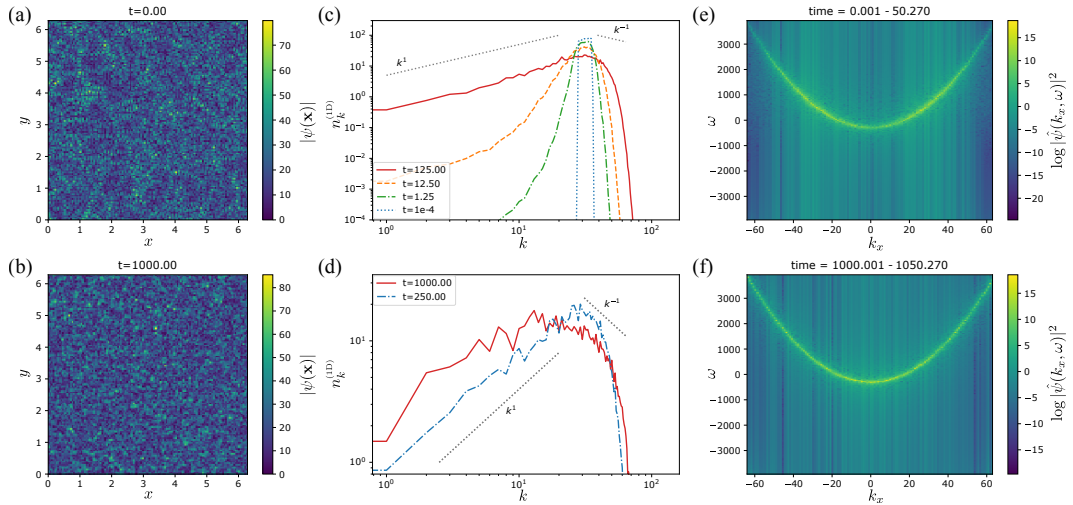


Figure 5.3: Freely-evolving run with the initial condition (5.9). First column: snapshots of $|\psi(\mathbf{x}, t)|$. Second column: 1D waveaction spectra. Third column: spatio-temporal spectra.

The spatio-temporal spectrum is a useful diagnostic in WT simulations and experiments as it indicates the kinds of dynamics and structures that are predominant in the system [181]. For example, a spatio-temporal spectrum that is concentrated around the linear dispersion relation reflects dynamics that are chiefly linear waves, with broadening around the dispersion relation indicating nonlinear wave interaction. This is the signature of the weak WT regime. Solitary compact structures in the spatial field also reveal themselves in the spatio-temporal spectrum as bands that are broad in the k dimension, with ballistic movement of these structures manifesting as tilted bands in the spatio-temporal spectrum due to Doppler shift.

Examining figures 5.3(a) and (b), we see that the $|\psi(\mathbf{x})|$ field fluctuates randomly throughout the simulation. Any structure from the initial condition, shown in (a) becomes quickly randomised after a short initial transient phase, with the field resembling (d) throughout most of the run. There is no evidence of a coherent structure developing during this run.

The transient is reflected in the evolution of the $n_k^{(1D)}$ spectrum shown in figure 5.3(c), where we see the spectrum quickly spreading across \mathbf{k} -space from its initial state (5.9). In the low- k range the spectral broadening slows down as it approaches the power law $n_k^{(1D)} \sim k$. The latter corresponds to the angle-integrated waveaction equipartition spectrum, which is the low- k limit of the RJ-like warm inverse cascade spectrum. Likewise in the high- k range we see the suggestion of

$k_x = N_x/2$, and for a long enough time as to capture a few (we choose eight) periods of the longest wave $k_x = 1$. This data is then Fourier transformed in time, and then squared.

the power law $n_k^{(1D)} \sim k^{-1}$, the angle-integrated energy equipartition spectrum, although we make this claim cautiously given the small inertial range that it would correspond to. As the simulation proceeds the spectrum evolves more slowly, aside from fluctuations. The shoulder between the $\sim k$ and $\sim k^{-1}$ ranges moves towards lower k with time, shrinking the waveaction equipartition range and growing the (presumptive) energy equipartition range, as shown in figure 5.3(d). This is qualitatively consistent a warm RJ-like spectrum whose chemical potential $\mu(t)$ decreases with time, as we will discuss in section 5.4.1.

Thus the freely-evolving simulation we present here develops a spectrum that, after the transient broadening phase, is consistent with the RJ-like warm cascade spectrum with time-dependent potentials $T(t)$ and $\mu(t)$. Of course we cannot draw the firm conclusion that this low-resolution simulation demonstrates the warm cascade predicted in chapter 4. Simulations at higher resolution must be done, together with fitting to the evolving RJ parameters $T(t)$ and $\mu(t)$, before we can claim that the warm cascade is demonstrated for the 2D SHE. However, the result we present here is a promising initial step in this direction.

Turning to figures 5.3(e) and (f), we see that the spatio-temporal spectrum is highly concentrated around a parabola throughout the run, consistent with the SHE dispersion $\omega_{\mathbf{k}} = k^2$. The lack of substantial broadening indicates that the simulation remains in the weak WT regime throughout its evolution, and as with the $|\psi(\mathbf{x})|$ field, there is no evidence of a coherent structure developing.

5.3.3 Forced-dissipated simulation: structure formation via the inverse cascade

Next we present a simulation with forcing and hyperviscous dissipation, to demonstrate the construction of a coherent condensate from turbulence. The forcing amplitude was $A_f = 0.1$ and the hyperviscosity coefficient was $\nu = 10^{-27}$. No hypoviscosity was used, in order to let the structure emerge out of the low- k end of the inverse cascade. To expedite the run, it was carried out with the larger timestep of $\Delta t = 2.5 \times 10^{-4}$, which, as we observed in section 5.3.1, has comparatively poor conservation of \mathcal{N} and \mathcal{H} in the corresponding freely-evolving run. Therefore conclusions drawn from these results must be treated very cautiously and considered provisional. However, note that when the system is forced, the $\sqrt{\Delta t}$ dependence in (5.6) turns the timestepping method into an order one-half scheme. Thus we do not expect the results of this section to differ qualitatively when a smaller timestep is used.

Figure 5.4 shows the results of this simulation, with the same diagnostics presented as in figure 5.3.

At the early time $t = 50$, figure 5.4(a) shows the low-level fluctuations in

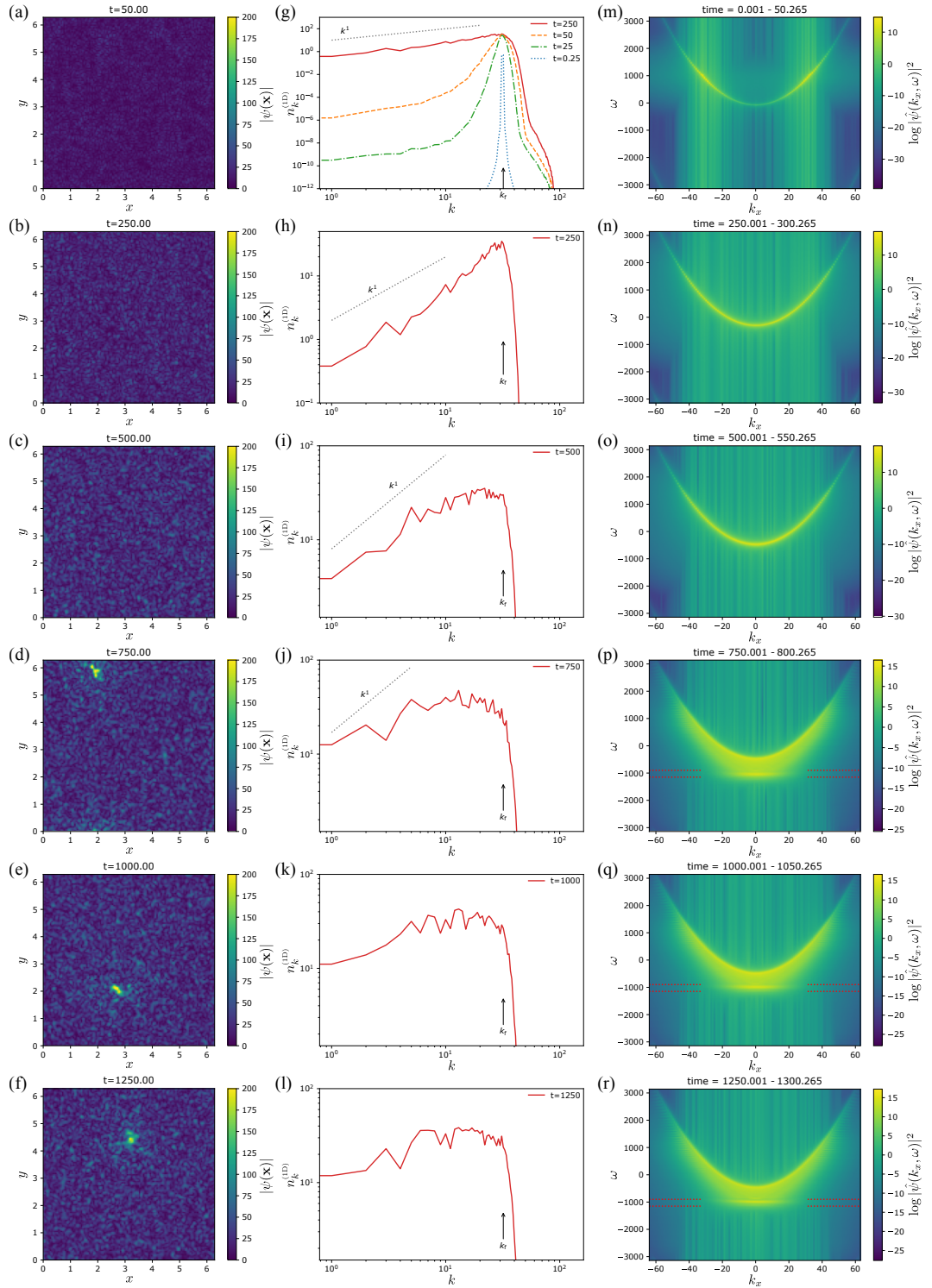


Figure 5.4: Forced-dissipated run with forcing around $k_f = 32$ and hyperviscosity. Columns are as in figure 5.3. Note the appearance of a coherent structure in the $|\psi(\mathbf{x})|$ field, and its signature in the spatio-temporal spectra, from $t = 750$ onwards.

the spatial field which strengthen with time as the turbulence develops due to the forcing. In (g) we see that the forcing around $k_f = 32$ quickly spreads out over k , as in the freely-evolving run. The spectrum in $k > k_f$ is damped by the hyperviscous dissipation so we see no evidence of the $\sim k^{-1}$ direct cascade warm spectrum. In the low- k range the spectral broadening again slows down as it approaches the $\sim k$ waveaction equipartition spectrum. The spatio-temporal spectrum for early times (m) is concentrated around k_f and follows a parabolic dispersion relation, exactly as expected for the SHE.

In the second and third row of figure 5.4 the fluctuations in the $|\psi(\mathbf{x})|$ field strengthen but remain incoherent. The spectrum $n_k^{(1D)}$ develops a flattened shoulder region at high k , and this shoulder progresses towards low k in time. As in section 5.3.2, this is qualitatively consistent with an RJ spectrum with $\mu(t)$ decreasing with time. The spatio-temporal spectrum remains parabolic, but broadens with time, indicating that the dynamics are in the weak WT regime but with an increasing degree of nonlinearity. The minimum of the dispersion relation dips progressively below $\omega = 0$, which is almost certainly due to a growing nonlinear frequency shift (4.33). It remains to measure this shift and compare it to its theoretical value.

At approximately $t = 710$ the $|\psi(\mathbf{x})|$ field rapidly coarsens and develops a strong, compact structure, which is shown in figures 5.4(d)-(f). This is the condensate discussed in chapter 4, which has developed from the inverse cascade. Once the condensate is present, the shoulder of the $n_k^{(1D)}$ spectrum has progressed to the lowest k and there is no longer any resemblance to the $\sim k$ waveaction equipartition spectrum. The spatio-temporal spectra in figures 5.4(p)-(r) show strong nonlinear broadening, strong nonlinear frequency shifts, and a component that is wide in k_x and distributed narrowly around $\omega = -1000$, marked out by the dashed red lines. This component is the signature of the condensate, and its flatness in the spatio-temporal spectrum reflects the fact that the movement of the condensate in \mathbf{x} -space resembles an unbiased random walk, rather than ballistic motion (to confirm this we would need to track and characterise the motion of the condensate quantitatively). The strength of the nonlinear effects visible in figures 5.4(p)-(r) indicate the breakdown of the weak WT regime.

Once the condensate forms the system appears to reach a nonequilibrium steady state: the condensate continues to wander through the simulation domain, the spectra fluctuate but do not appear to change in mean, and the spatiotemporal spectrum stabilises. This is also reflected in the histories of the waveaction and energy shown in figure 5.5. Around $t \approx 710$ when the condensate appears, the total waveaction and linear energy reach their maximum, and the total and nonlinear energies reach their minimum, after which these global quantities stabilise.

We also plot the value of the $N_x N_y |\psi_{\mathbf{k}=(0,0)}|^2$, i.e. the fundamental mode

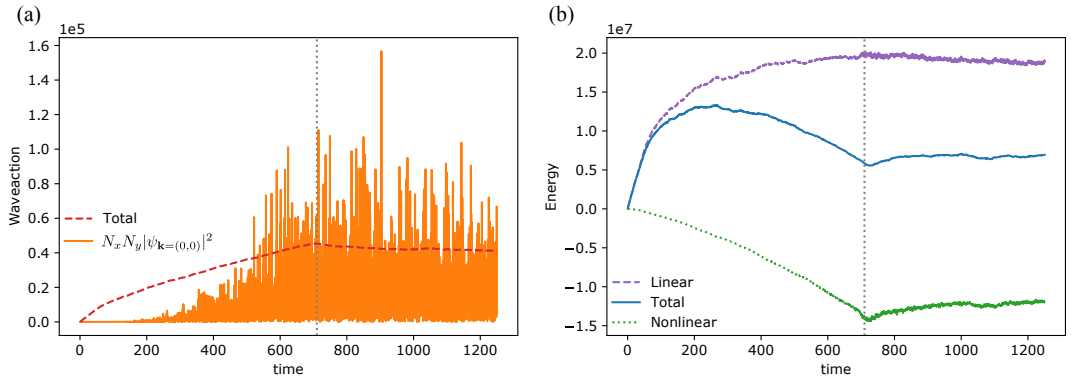


Figure 5.5: Time series of (a) the total waveaction, and scaled waveaction in the fundamental mode, and (b) the total, linear, and nonlinear energy for the forced-dissipated run. Vertical grey dots indicate $t = 710$, the approximate time of appearance of the condensate.

scaled by the system volume, with the scaling necessary in order to make its value visible compared to the total waveaction in figure 5.5(a). Note that even after the appearance of the compact condensate in physical space, the fundamental mode is *not* macroscopically occupied. This is in contrast to the condensate in the local NLS, for which the condensate is flat in physical space [10], and represented in Fourier space by the macroscopic occupation of the $\mathbf{k} = 0$ mode. In the present case, as the condensate in our simulation is reasonably compact, its spectrum will encompass many modes around the fundamental. Indeed, this is seen in the spatio-temporal spectra.

We have continued the simulation until $t = 2000$ and observe no further evolution of the system beyond fluctuations.

Animations of the $|\psi(\mathbf{x})|$ field and the $n_k^{(1D)}$ spectrum for both the freely-evolving and the forced-dissipated simulations can be found at link [182].

5.4 Discussion and future direction of research

5.4.1 Discussion of numerical results

To summarise, we have observed numerically, in both the freely-evolving and forced-dissipated 2D SHE, that after a transient stage the angle-integrated 1D spectra settle down in a state that resembles the warm RJ-like cascade spectrum, especially in its low- k range. This occurs while the system is in the weak WT regime, as evidenced by the spatio-temporal spectra. In the forced-dissipated case we observe a condensate emerging from a turbulent field via an inverse cascade, together with the breakdown of the weak WT regime. These results support the general picture outlined in chapter 4.

Furthermore, as the $n_k^{(1D)}$ spectra evolve, the shoulder between the $n_k^{(1D)} \sim k$ regime at the low- k end and the flat or descending spectrum at high k (which resembles $\sim k^{-1}$ in the freely-evolving case), moves toward low k as time goes on. If the spectrum is an RJ-like warm spectrum then this movement of the shoulder would indicate a chemical potential $\mu(t)$ that is shrinking in time. We recall the discussion of the NLS in section 3.A, where it was noted that condensation within the RJ spectrum is characterised by $\mu, T \rightarrow 0$ (although this statement is only strictly true in the weak WT limit, we expect the same phenomenology to carry over to the strongly nonlinear regime when the condensate is becoming significant). Thus the time evolution in a situation where a condensate grows via an inverse cascade will naturally include a situation where $\mu(t) \rightarrow 0$ in the advent of the condensate. Our results for the forced-dissipated case are a promising hint in this direction.

Of course, our study is not yet complete and there are many quantitative measurements that we have already mentioned that need to be made.

The major caveat that we must make about our results is the fact that our forced-dissipated run was made with a rather large timestep. The corresponding freely-evolving simulation with this timestep loses waveaction and energy rapidly. Despite this, our findings for this run are in qualitative agreement with those of section 5.3.2—the freely-evolving run with a smaller timestep—as far as the behaviour of the $n_k^{(1D)}$ spectrum in the weakly nonlinear regime is concerned. In the strongly nonlinear regime, the results are in agreement with the general scenario of a condensate appearing out of an inverse cascade. However the judgement must be reserved until the findings are replicated in a run with a smaller timestep, although we note once more that forcing via (5.6) constrains the time integration scheme to be of order one-half, so we are unlikely to see a dramatic change when a smaller timestep is used.

Aside from the timestep issue, the other major caveat of this study is that one cannot draw firm, quantitative conclusions from a study at such a low resolution. Moving to a higher resolution would make room for a larger inertial range for the cascades, which would be necessary for quantitative measurement of $T(t)$ and $\mu(t)$. These measurements at a higher resolution would provide much stronger evidence for the warm cascade in the SHE.

Aspects that merit further investigation include whether a condensate can occur in a freely-evolving system, either the existing one from section 5.3.2 but run for longer, or a system launched from an initial condition that contains more \mathcal{N} from which to construct the condensate. Such runs are currently ongoing. As to the forced-dissipated run, the saturation of the dynamics after $t \approx 750$, and the small size of the condensate as compared to the truly large-scale condensates in the NLS (see e.g. [10]), need further examination. It remains to be seen whether the time to

condensation, the condensate size, and the subsequent evolution of the system, are related to the leak of \mathcal{N} and \mathcal{H} due to the large timestep, whether they are effects that change with resolution, or whether they are intrinsic to the physics.

5.4.2 Future directions

Once the investigations outlined above have been completed, the scope for further research directions opens widely. The next stage would be to carry out simulations with forcing and dissipation at both high and low k , ideally to realise a stationary dual cascade with no condensate. This would allow the pure flux spectrum to be examined and compared to an RJ spectrum with stationary potentials. In practice a dual cascade with large inverse and direct inertial ranges might be difficult to realise simultaneously, even at high resolution. In this case one might have to realise each range separately by appropriate placement of the forcing scale and tuning of the dissipation parameters.

The results presented here are for the SHE with $\Lambda = 1$, i.e. its strongly nonlocal (Schrödinger-Newton) limit (note that this is the value of Λ set at the outset of our simulations as an adjustable parameter—as the system is forced and the average density $\langle |\psi(\mathbf{x})|^2 \rangle_{T_L^2}$ grows, the effective Λ will change, c.f. section 4.A). In chapter 4 we made predictions relating to the Schrödinger-Newton and the nonlinear Schrödinger limits of the SHE, but made no predictions about an intermediate regime (aside from the discussion in 4.4.5 of the crossover from the warm to the KZ spectrum in the 3D SHE). A numerical exploration could be carried out, in particular to investigate how the size of the condensates is affected by the nonlocality length $\Lambda^{-1/2}$.

Finally, as discussed in section 4.5, one might expect that the long-term dynamics of the SHE include growth and instability of the condensate, and its subsequent fragmentation. Such a scenario is observed in the 1D SHE [21, 22] and one would expect that a similar phenomenology would carry over to the 2D case presented here, and also to the 3D case. This direction of research invites further numerical investigations using this code, and indeed remains the main motivation for exploring the processes of inverse cascade and condensation in the SHE, within the framework of WT theory.

Bibliography

- [1] J. Skipp and S. Nazarenko. Equilibria and condensates in Rossby and drift wave turbulence. *arXiv preprint arXiv:2108.08349*, 2021.
- [2] J. Skipp, V. L’vov, and S. Nazarenko. Wave turbulence in self-gravitating bose gases and nonlocal nonlinear optics. *Physical Review A*, 102(4):043318, 2020.
- [3] S. Nazarenko. *Wave turbulence*, volume 825 of *Lecture Notes in Physics*. Springer, 2011.
- [4] V. E. Zakharov, V. S. L’vov, and G. Falkovich. *Kolmogorov spectra of turbulence I: Wave turbulence*. Springer Series in Nonlinear Dynamics. Springer, 1992.
- [5] A.N. Kolmogorov. The local structure of turbulence in incompressible viscous fluid for very large Reynolds numbers. *Doklady Akad. Nauk SSSR*, 30:9, 1941.
- [6] A.M. Obukhov. On the distribution of energy in the spectrum of turbulent flow. *Dokl. Akad. Nauk SSSR.*, 32:22, 1941.
- [7] Vladimir E Zakharov. Weak turbulence in media with a decay spectrum. *Journal of Applied Mechanics and Technical Physics*, 6(4):22–24, 1965.
- [8] Yuri Lvov, Sergey Nazarenko, and Robert West. Wave turbulence in Bose-Einstein condensates. *Phys. D*, 184(1-4):333–351, 2003.
- [9] V. E. Zakharov and S. V. Nazarenko. Dynamics of the Bose-Einstein condensation. *Physica D: Nonlinear Phenomena*, 201(3-4):203–211, 2005.
- [10] S. Nazarenko and M. Onorato. Wave turbulence and vortices in Bose–Einstein condensation. *Physica D: Nonlinear Phenomena*, 219(1):1–12, 2006.
- [11] S. Nazarenko and M. Onorato. Freely decaying turbulence and Bose–Einstein condensation in Gross–Pitaevski model. *Journal of Low Temperature Physics*, 146(1):31–46, 2007.

- [12] D. Proment, S. Nazarenko, and M. Onorato. Quantum turbulence cascades in the Gross-Pitaevskii model. *Phys. Rev. A*, 80(5):051603, 2009.
- [13] S. Nazarenko, M. Onorato, and D. Proment. Bose-Einstein condensation and Berezinskii-Kosterlitz-Thouless transition in the two-dimensional nonlinear Schrödinger model. *Physical Review A*, 90(1):013624, 2014.
- [14] N. Navon, A. L. Gaunt, R. P. Smith, and Z. Hadzibabic. Emergence of a turbulent cascade in a quantum gas. *Nature*, 539(7627):72–75, 2016.
- [15] E. Kozik and B. Svistunov. Kelvin-wave cascade and decay of superfluid turbulence. *Phys. Rev. Lett.*, 92(3):035301, 2004.
- [16] Sergey Nazarenko. Differential approximation for Kelvin wave turbulence. *JETP Lett.*, 83(5):198–200, 2006.
- [17] G. Boffetta, A. Celani, D. Dezzani, J. Laurie, and S. Nazarenko. Modeling Kelvin wave cascades in superfluid helium. *J. Low Temp. Phys.*, 156(3-6): 193–214, 2009.
- [18] Victor S. L’vov and Sergey Nazarenko. Weak turbulence of Kelvin waves in superfluid He. *Low Temp. Phys.*, 36(8-9):785–791, 2010.
- [19] S. Dyachenko, A. C. Newell, A. Pushkarev, and V. E. Zakharov. Optical turbulence: weak turbulence, condensates and collapsing filaments in the nonlinear Schrödinger equation. *Phys. D*, 57(1):96–160, 1992.
- [20] C. Connaughton, C. Josserand, A. Picozzi, Y. Pomeau, and S. Rica. Condensation of classical nonlinear waves. *Physical Review Letters*, 95(26):263901, 2005.
- [21] Umberto Bortolozzo, Jason Laurie, Sergey Nazarenko, and Stefania Residori. Optical wave turbulence and the condensation of light. *J. Opt. Soc. Am. B*, 26(12):2280–2284, 2009.
- [22] Jason Laurie, Umberto Bortolozzo, Sergey Nazarenko, and Stefania Residori. One-dimensional optical wave turbulence: Experiment and theory. *Phys. Rep.*, 514(4):121–175, 2012.
- [23] G. Düring, C. Josserand, and S. Rica. Weak turbulence for a vibrating plate: can one hear a Kolmogorov spectrum? *Phys. Rev. Lett.*, 97(2):025503, 2006.
- [24] N. Mordant. Are there waves in elastic wave turbulence? *Phys. Rev. Lett.*, 100(23):234505, 2008.

- [25] K. Hasselmann. On the non-linear energy transfer in a gravity-wave spectrum Part 1. General theory. *Journal of Fluid Mechanics*, 12(4):481–500, 1962.
- [26] K. Hasselmann. On the non-linear energy transfer in a gravity wave spectrum Part 2. Conservation theorems; wave-particle analogy; irreversibility. *Journal of Fluid Mechanics*, 15(2):273–281, 1963.
- [27] A. I. Dyachenko, Y. V. Lvov, and V. E. Zakharov. Five-wave interaction on the surface of deep fluid. *Physica D: Nonlinear Phenomena*, 87(1-4):233–261, 1995.
- [28] P. Denissenko, S. Lukaschuk, and S. Nazarenko. Gravity wave turbulence in a laboratory flume. *Phys. Rev. Lett.*, 99(1):014501, 2007.
- [29] C. Falcon, E. Falcon, U. Bortolozzo, and S. Fauve. Capillary wave turbulence on a spherical fluid surface in low gravity. *EPL (Europhysics Letters)*, 86(1):14002, 2009.
- [30] S. Nazarenko, S. Lukaschuk, Stuart M., and P. Denissenko. Statistics of surface gravity wave turbulence in the space and time domains. *Journal of Fluid Mechanics*, 642:395–420, 2010.
- [31] M. S. Longuet-Higgins, A. E. Gill, and K. Kenyon. Resonant interactions between planetary waves [and discussion]. *Proceedings of the Royal Society of London. Series A, Mathematical and Physical Sciences*, 299(1456):120–144, 1967.
- [32] A. M. Balk, S. V. Nazarenko, and V. E. Zakharov. On the structure of the Rossby/drift turbulence and zonal flows. In *Proceedings of the International Symposium “Generation of Large-Scale Structures in Continuous Media”, Perm-Moscow, USSR*, pages 34–35, 1990.
- [33] A. M. Balk, V. E. Zakharov, and S. V. Nazarenko. Nonlocal turbulence of drift waves. *Soviet Phys. JETP*, 71(2):249–260, 1990.
- [34] A. M. Balk. A new invariant for Rossby wave systems. *Physics Letters A*, 155(1):20–24, 1991.
- [35] A. M. Balk, S. V. Nazarenko, and V. E. Zakharov. New invariant for drift turbulence. *Physics Letters A*, 152(5-6):276–280, 1991.
- [36] S. Nazarenko and B. Quinn. Triple cascade behavior in quasigeostrophic and drift turbulence and generation of zonal jets. *Physical Review Letters*, 103(11):118501, 2009.

- [37] C. Connaughton, S. Nazarenko, and B. Quinn. Feedback of zonal flows on wave turbulence driven by small-scale instability in the Charney-Hasegawa-Mima model. *EPL (Europhysics Letters)*, 96(2):25001, 2011.
- [38] K. L. Harper, M. D. Bustamante, and S. V. Nazarenko. Quadratic invariants for discrete clusters of weakly interacting waves. *Journal of Physics A: Mathematical and Theoretical*, 46(24):245501, 2013.
- [39] C. Connaughton, S. Nazarenko, and B. Quinn. Rossby and drift wave turbulence and zonal flows: the Charney-Hasegawa-Mima model and its extensions. *Physics Reports*, 604:1–71, 2015.
- [40] K. L. Harper and S. V. Nazarenko. Large-scale drift and rossby wave turbulence. *New Journal of Physics*, 18(8):085008, 2016.
- [41] S. Galtier, S. V. Nazarenko, Alan C. Newell, and A. Pouquet. A weak turbulence theory for incompressible magnetohydrodynamics. *J. Plasma Phys.*, 63(5):447–488, 2000.
- [42] N. Tronko, S. V. Nazarenko, and S. Galtier. Weak turbulence in two-dimensional magnetohydrodynamics. *Physical Review E*, 87(3):033103, 2013.
- [43] N. K. Bell and S. V. Nazarenko. Reflected wave solution of Alfvén wave turbulence. *Journal of Physics A: Mathematical and Theoretical*, 51(40):405501, 2018.
- [44] N. K. Bell and S. V. Nazarenko. Rotating magnetohydrodynamic turbulence. *Journal of Physics A: Mathematical and Theoretical*, 52(44):445501, 2019.
- [45] S. Galtier and S. V. Nazarenko. Turbulence of weak gravitational waves in the early universe. *Physical review letters*, 119(22):221101, 2017.
- [46] S. Galtier, J. Laurie, and S. V. Nazarenko. A plausible model of inflation driven by strong gravitational wave turbulence. *Universe*, 6(7):98, 2020.
- [47] P. H. Diamond, S. I. Itoh, K. Itoh, and T. S. Hahm. Zonal flows in plasma – a review. *Plasma Physics and Controlled Fusion*, 47(5):R35, 2005.
- [48] B. Galperin and P. L. Read. *Zonal Jets: Phenomenology, Genesis, and Physics*. Cambridge University Press, 2019. ISBN 9781107619562.
- [49] I. N. James. Suppression of baroclinic instability in horizontally sheared flows. *Journal of the atmospheric sciences*, 44(24):3710–3720, 1987.

- [50] Yeontaek Choi, Yuri V. Lvov, and Sergey Nazarenko. Probability densities and preservation of randomness in wave turbulence. *Phys. Lett. A*, 332(3-4): 230–238, 2004.
- [51] Yeontaek Choi, Yuri V. Lvov, and Sergey Nazarenko. Joint statistics of amplitudes and phases in wave turbulence. *Phys. D*, 201(1-2):121–149, 2005.
- [52] Yeontaek Choi, Yuri V. Lvov, and Sergey Nazarenko. Wave turbulence. In *Recent developments in fluid dynamics*, page 225, Kepala, India, 2004. Transworld Research Network.
- [53] V. E. Zakharov and L. I. Piterbarg. Canonical variables for Rossby waves and plasma drift waves. *Physics Letters A*, 126(8-9):497–500, 1988.
- [54] A. C. Newell and Rumpf B. Wave Turbulence. *Annual Review of Fluid Mechanics*, 43:59–78, 2011.
- [55] S. Nazarenko. *Drift and Rossby Wave Turbulence*. PhD thesis, Landau Institute for Theoretical Physics, 1991.
- [56] V. E. Zakharov and N. N. Filonenko. Energy spectrum for stochastic oscillations of the surface of a liquid. In *Soviet Physics Doklady*, volume 11, page 881, 1967.
- [57] R. H. Kraichnan. Inertial ranges in two-dimensional turbulence. *The Physics of Fluids*, 10(7):1417–1423, 1967.
- [58] E. A. Kuznetsov. Turbulence of ion sound in a plasma located in a magnetic field. *Sov. Phys. JETP*, 35:310, 1972.
- [59] A. S. Monin and L. I. Piterbarg. A kinetic equation for Rossby waves. In *Soviet Physics Doklady*, volume 32, page 622, 1987.
- [60] A. B. Mikhailovskii, S. V. Novakovskii, V. P. Lakhin, S. V. Makurin, E.A. Novakovskaya, and O. G. Onishchenko. Kolmogorov weak turbulence spectra of an inhomogeneous magnetized plasma. *Sov. Phys. JETP*, 68:1386–1392, 1988.
- [61] S. V. Novakovskii, A. B. Mikhailovskii, and O. G. Onishchenko. On the theory of Kolmogorov spectra of drift wave turbulence. *Physics Letters A*, 132(1): 33–38, 1988.
- [62] A. M. Balk and S.V. Nazarenko. On the physical realizability of anisotropic Kolmogorov spectra of weak turbulence. *Sov. Phys. JETP*, 70(3), 1990.

- [63] R. Fjørtoft. On the changes in the spectral distribution of kinetic energy for twodimensional, nondivergent flow. *Tellus*, 5(3):225–230, 1953.
- [64] P. B. Rhines. Geostrophic turbulence. *Annual Review of Fluid Mechanics*, 11(1):401–441, 1979.
- [65] L. Onsager. Statistical hydrodynamics. *Nuovo Cimento*, 6(2):279–287, 1949.
- [66] R. H. Kraichnan. Statistical dynamics of two-dimensional flow. *Journal of Fluid Mechanics*, 67(1):155–175, 1975.
- [67] R. H. Kraichnan and D. Montgomery. Two-dimensional turbulence. *Reports on Progress in Physics*, 43(5):547, 1980.
- [68] P. B. Rhines. Waves and turbulence on a beta-plane. *Journal of Fluid Mechanics*, 69(3):417–443, 1975.
- [69] A. Hasegawa, C. G. MacLennan, and Y. Kodama. Nonlinear behavior and turbulence spectra of drift waves and Rossby waves. *The Physics of Fluids*, 22(11):2122–2129, 1979. doi: 10.1063/1.862504.
- [70] A. I. Dyachenko, S. V. Nazarenko, and V. E. Zakharov. Wave-vortex dynamics in drift and β -plane turbulence. *Phys. Lett. A*, 165(4):330–334, 1992.
- [71] H.-P. Huang, B. Galperin, and S. Sukoriansky. Anisotropic spectra in two-dimensional turbulence on the surface of a rotating sphere. *Physics of Fluids*, 13(1):225–240, 2001.
- [72] M. G. Shats, H. Xia, and H. Punzmann. Spectral condensation of turbulence in plasmas and fluids and its role in low-to-high phase transitions in toroidal plasma. *Physical Review E*, 71(4):046409, 2005.
- [73] NASA, ESA, and A. Simon (Goddard Space Flight Center). Jupiter and its shrunken great red spot, May 2014. URL <https://esahubble.org/images/heic1410a/>. [Online; accessed 16 March 2015].
- [74] A. Peeters. 3d-with zonal flow, October 2010. URL <http://www.gkw.org.uk/tikiwiki/browseimage2/>. [Online; accessed 16 March 2015].
- [75] J. G. Charney. On the scale of atmospheric motions. *Geophys. Publ. Kosjones Nors. Videnshap. Akad. Oslo*, 17(2):3–17, 1948.
- [76] A. Hasegawa and K. Mima. Stationary spectrum of strong turbulence in magnetized nonuniform plasma. *Physical Review Letters*, 39(4):205, 1977.

- [77] A. Einstein. Quantentheorie des einatomigen idealen Gases. Zweite Abhandlung. *Sitzungsberichte der Preußischen Akademie der Wissenschaften, Physikalisch-Mathematische Klasse, Berlin*, pages 3–14, 1925.
- [78] Lev Pitaevskii and Sandro Stringari. *Bose-Einstein Condensation and Superfluidity*, volume 164 of *International series of monographs on physics*. Oxford University Press, 2016.
- [79] N. D. Mermin and H. Wagner. Absence of ferromagnetism or antiferromagnetism in one or two-dimensional isotropic Heisenberg models. *Physical Review Letters*, 17(22):1133–1136, 1966.
- [80] P. C. Hohenberg. Existence of long-range order in one and two dimensions. *Phys. Rev.*, 158(2):383–386, 1967.
- [81] V. Bagnato and D. Kleppner. Bose-Einstein condensation in low-dimensional traps. *Physical Review A*, 44(11):7439, 1991.
- [82] A. I. Safonov, S. A. Vasilyev, I. S. Yasnikov, I. I. Lukashevich, and S. Jaakkola. Observation of quasicondensate in two-dimensional atomic hydrogen. *Physical Review Letters*, 81(21):4545, 1998.
- [83] G. Düring, A. Picozzi, and S. Rica. Breakdown of weak-turbulence and nonlinear wave condensation. *Physica D: Nonlinear Phenomena*, 238(16):1524–1549, 2009.
- [84] Z. Hadzibabic and J. Dalibard. Two-dimensional Bose fluids: An atomic physics perspective. *La Rivista del Nuovo Cimento*, 34(6):389–434, 2011.
- [85] K. Baudin, A. Fusaro, K. Krupa, J. Garnier, S. Rica, G. Millot, and A. Picozzi. Classical Rayleigh-Jeans condensation of light waves: Observation and thermodynamic characterization. *Physical Review Letters*, 125(24):244101, 2020.
- [86] R. Peierls. Zur kinetischen Theorie der Wärmeleitung in Kristallen. *Annalen der Physik*, 395(8):1055–1101, 1929.
- [87] D. G. Fox and S. A. Orszag. Inviscid dynamics of two-dimensional turbulence. *The Physics of Fluids*, 16(2):169–171, 1973.
- [88] E. M. Purcell and R. V. Pound. A nuclear spin system at negative temperature. *Physical Review*, 81(2):279, 1951.
- [89] M. Onorato, G. Dematteis, D. Proment, A. Pezzi, M. Ballarin, and L. Rondoni. Negative temperature states as exact equilibrium solutions of the wave kinetic equation for one dimensional lattices. *arXiv preprint arXiv:2012.10618*, 2020.

- [90] K. Baudin, A. Fusaro, J. Garnier, N. Berti, K. Krupa, I. Carusotto, S. Rica, G. Millot, and A. Picozzi. Energy and wave-action flows underlying Rayleigh-Jeans thermalization of optical waves propagating in a multimode fiber. *EPL (Europhysics Letters)*, 134(1):14001, 2021.
- [91] C. Connaughton, S. Nazarenko, and B. Quinn. Nonlocal wave turbulence in the Charney-Hasegawa-Mima equation: a short review. *arXiv preprint arXiv:1012.2714*, 2010.
- [92] I. Saito and K. Ishioka. Angular distribution of energy spectrum in two-dimensional β -plane turbulence in the long-wave limit. *Physics of Fluids*, 25(7):076602, 2013.
- [93] E. P. Gross. Structure of a quantized vortex in boson systems. *Il Nuovo Cimento*, 20(3):454–477, 1961.
- [94] L. P. Pitaevskii. Vortex lines in an imperfect Bose gas. *Sov. Phys. JETP*, 13(2):451–454, 1961.
- [95] B. Gallet, S. Nazarenko, and B. Dubrulle. Wave-turbulence description of interacting particles: Klein-Gordon model with a Mexican-hat potential. *Physical Review E*, 92(1):012909, 2015.
- [96] A. C. Newell and J. V. Moloney. *Nonlinear Optics*. ATIMS Series. Addison-Wesley, Redwood City, CA, 1992.
- [97] Robert W. Boyd. *Nonlinear optics*. Academic press, 3 edition, 2008.
- [98] G. B. Whitham. *Linear and Nonlinear Waves*, volume 42 of *Pure and Applied Mathematics: A Wiley-Interscience Series of Texts, Monographs and Tracts*. John Wiley & Sons, New York, 1999.
- [99] David J. E. Marsh. Axion cosmology. *Phys. Rep.*, 643:1–79, 2016.
- [100] Jens C. Niemeyer. Small-scale structure of fuzzy and axion-like dark matter. *Prog. Part. Nucl. Phys.*, 113:103787, 2020.
- [101] Wayne Hu, Rennan Barkana, and Andrei Gruzinov. Fuzzy cold dark matter: The wave properties of ultralight particles. *Phys. Rev. Lett.*, 85(6):1158–1161, 2000.
- [102] Abril Suárez, Victor H. Robles, and Tonatiuh Matos. A review on the scalar field/Bose-Einstein condensate dark matter model. In Claudia Moreno González, José Edgar Madriz Aguilar, and Luz Marina Reyes Barrera, editors, *Accelerated Cosmic Expansion*, pages 107–142, Cham, 2014. Springer International Publishing.

- [103] Pierre-Henri Chavanis. Self-gravitating Bose-Einstein Condensates. In Xavier Calmet, editor, *Quantum Aspects of Black Holes*, chapter 6, pages 151–194. Springer International Publishing, Cham, 2015.
- [104] Lam Hui, Jeremiah P. Ostriker, Scott Tremaine, and Edward Witten. Ultra-light scalars as cosmological dark matter. *Phys. Rev. D*, 95(4):043541, 2017.
- [105] Elisa G. M. Ferreira. Ultra-light dark matter. *arXiv preprint arXiv:2005.03254*, 2020.
- [106] M. R. Baldeschi, G. B. Gelmini, and R. Ruffini. On massive fermions and bosons in galactic halos. *Phys. Lett. B*, 122(3-4):221–224, 1983.
- [107] Jae-weon Lee and In-gyu Koh. Galactic halos as boson stars. *Phys. Rev. D*, 53(4):2236–2239, 1996.
- [108] Hsi-Yu Schive, Tzihong Chiueh, and Tom Broadhurst. Cosmic structure as the quantum interference of a coherent dark wave. *Nat. Phys.*, 10(7):496–499, 2014.
- [109] Akhilesh Kumar Verma, Rahul Pandit, and Marc E. Brachet. The formation of compact objects at finite temperatures in a dark-matter-candidate self-gravitating bosonic system. *arXiv preprint arXiv:1912.10172*, 2019.
- [110] L. Jaramillo and O. Macias. An artist’s impression of Milky Way, with the Galactic bulge at the centre. Virginia Tech. URL <https://anu.prezly.com/mysterious-signal-comes-from-very-old-stars-at-centre-of-our-galaxy>. [Online; accessed June 2020].
- [111] J. M. Overduin and P. S. Wesson. Dark matter and background light. *Phys. Rep.*, 402:267–406, 2004.
- [112] P. J. E. Peebles and Bharat Ratra. The cosmological constant and dark energy. *Rev. Mod. Phys.*, 75(2):559–606, 2003.
- [113] Volker Springel, Simon D. M. White, Adrian Jenkins, Carlos S. Frenk, Naoki Yoshida, Liang Gao, Julio Navarro, Robert Thacker, Darren Croton, John Helly, et al. Simulations of the formation, evolution and clustering of galaxies and quasars. *Nature*, 435(7042):629–636, 2005.
- [114] D. H. Weinberg, J. S. Bullock, F. Governato, R. Kuzio de Naray, and Peter A. H. G. Cold dark matter: Controversies on small scales. *Proc. Natl. Acad. Sci. U. S. A.*, 112(40):12249–12255, 2015.
- [115] James S. Bullock and Michael Boylan-Kolchin. Small-scale challenges to the Λ CDM paradigm. *Annu. Rev. Astron. Astrophys.*, 55:343–387, 2017.

- [116] T. Harko. Bose-Einstein condensation of dark matter solves the core/cusp problem. *J. Cosmol. Astropart. Phys.*, 2011(05):022, 2011.
- [117] David J. E. Marsh and Ana-Roxana Pop. Axion dark matter, solitons and the cusp-core problem. *Mon. Not. R. Astron. Soc.*, 451(3):2479–2492, 2015.
- [118] Monica Colpi, Stuart L. Shapiro, and Ira Wasserman. Boson stars: Gravitational equilibria of self-interacting scalar fields. *Phys. Rev. Lett.*, 57(20):2485–2488, 1986.
- [119] Philip Mocz, Mark Vogelsberger, Victor H. Robles, Jesús Zavala, Michael Boylan-Kolchin, Anastasia Fialkov, and Lars Hernquist. Galaxy formation with BECDM—I. Turbulence and relaxation of idealized haloes. *Mon. Not. R. Astron. Soc.*, 471(4):4559–4570, 2017.
- [120] Philip Mocz, Anastasia Fialkov, Mark Vogelsberger, Fernando Becerra, Mustafa A. Amin, Sownak Bose, Michael Boylan-Kolchin, Pierre-Henri Chavanis, Lars Hernquist, Lachlan Lancaster, et al. First star-forming structures in fuzzy cosmic filaments. *Phys. Rev. Lett.*, 123(14):141301, 2019.
- [121] Philip Mocz, Anastasia Fialkov, Mark Vogelsberger, Fernando Becerra, Xuejian Shen, Victor H. Robles, Mustafa A. Amin, Jesús Zavala, Michael Boylan-Kolchin, Sownak Bose, Federico Marinacci, Pierre-Henri Chavanis, Lachlan Lancaster, and Lars Hernquist. Galaxy formation with BECDM—II. Cosmic filaments and first galaxies. *Mon. Not. R. Astron. Soc.*, 494(2):2027–2044, 04 2020.
- [122] M. D. Iturbe Castillo, J. J. Sánchez-Mondragón, and S. Stepanov. Formation of steady-state cylindrical thermal lenses in dark stripes. *Opt. Lett.*, 21(20):1622–1624, 1996.
- [123] Iam-Choon Khoo. *Liquid Crystals*. John Wiley & Sons, 2 edition, 2007.
- [124] Allan W. Snyder and D. John Mitchell. Accessible solitons. *Science*, 276 (5318):1538–1541, 1997.
- [125] Claudio Conti, Marco Peccianti, and Gaetano Assanto. Route to nonlocality and observation of accessible solitons. *Phys. Rev. Lett.*, 91(7):073901, 2003.
- [126] Carmel Rotschild, Oren Cohen, Ofer Manela, Mordechai Segev, and Tal Carmon. Solitons in nonlinear media with an infinite range of nonlocality: first observation of coherent elliptic solitons and of vortex-ring solitons. *Phys. Rev. Lett.*, 95(21):213904, 2005.

- [127] Carmel Rotschild, Barak Alfassi, Oren Cohen, and Mordechai Segev. Long-range interactions between optical solitons. *Nat. Phys.*, 2(11):769–774, 2006.
- [128] Víctor M. Pérez-García, Vladimir V. Konotop, and Juan J. García-Ripoll. Dynamics of quasicollapse in nonlinear schrödinger systems with nonlocal interactions. *Phys. Rev. E*, 62(3):4300, 2000.
- [129] Ole Bang, Wieslaw Krolikowski, John Wyller, and Jens Juul Rasmussen. Collapse arrest and soliton stabilization in nonlocal nonlinear media. *Phys. Rev. E*, 66(4):046619, 2002.
- [130] Marco Peccianti, Claudio Conti, and Gaetano Assanto. Optical modulational instability in a nonlocal medium. *Phys. Rev. E*, 68(2):025602, 2003.
- [131] Neda Ghofraniha, Claudio Conti, Giancarlo Ruocco, and Stefano Trillo. Shocks in nonlocal media. *Phys. Rev. Lett.*, 99(4):043903, 2007.
- [132] G. Xu, D. Vocke, D. Faccio, J. Garnier, Thomas Roger, Stefano Trillo, and A. Picozzi. From coherent shocklets to giant collective incoherent shock waves in nonlocal turbulent flows. *Nat. Commun.*, 6(1):8131, 2015.
- [133] Thomas Roger, Calum Maitland, Kali Wilson, Niclas Westerberg, David Vocke, Ewan M. Wright, and Daniele Faccio. Optical analogues of the Newton-Schrödinger equation and boson star evolution. *Nat. Commun.*, 7:13492, 2016.
- [134] Rivka Bekenstein, Ran Schley, Maor Mutzafi, Carmel Rotschild, and Mordechai Segev. Optical simulations of gravitational effects in the Newton-Schrödinger system. *Nat. Phys.*, 11:872–878, 2015.
- [135] Alvaro Navarrete, Angel Paredes, José R Salgueiro, and Humberto Michinel. Spatial solitons in thermo-optical media from the nonlinear Schrödinger-Poisson equation and dark-matter analogs. *Phys. Rev. A*, 95(1):013844, 2017.
- [136] Angel Paredes, David N Olivieri, and Humberto Michinel. From optics to dark matter: A review on nonlinear Schrödinger–Poisson systems. *Phys. D*, 403:132301, 2020.
- [137] Michael K.-H. Kiessling. The “Jeans swindle”: a true story — mathematically speaking. *Adv. Appl. Math.*, 31(1):132–149, 2003.
- [138] James Binney and Scott Tremaine. *Galactic Dynamics*. Princeton Series in Astrophysics. Princeton University Press, 2 edition, 2008.
- [139] W. F. Vinen and J. J. Niemela. Quantum turbulence. *J. Low Temp. Phys.*, 128(5):167–231, 2002.

- [140] Carlo F. Barenghi, Russell J. Donnelly, and W. F. Vinen. *Quantized Vortex Dynamics and Superfluid Turbulence*, volume 571 of *Lecture Notes in Physics*. Springer-Verlag, 2001.
- [141] Michikazu Kobayashi and Makoto Tsubota. Quantum turbulence in a trapped Bose-Einstein condensate. *Physical Review A*, 76(4):045603, 2007.
- [142] Giorgio Krstulovic and Marc Brachet. Dispersive bottleneck delaying thermalization of turbulent bose-einstein condensates. *Phys. Rev. Lett.*, 106(11):115303, 2011.
- [143] Marios C. Tsatsos, Pedro E. S. Tavares, André Cidrim, Amilson R. Fritsch, Mônica A. Caracanhas, F. Ednilson A. dos Santos, Carlo F. Barenghi, and Vanderlei S. Bagnato. Quantum turbulence in trapped atomic Bose-Einstein condensates. *Phys. Rep.*, 622:1–52, 2016.
- [144] Makoto Tsubota, Kazuya Fujimoto, and Satoshi Yui. Numerical Studies of Quantum Turbulence. *J. Low Temp. Phys.*, 188(5-6):119–189, 2017.
- [145] Nicolás P. Müller, Marc-Etienne Brachet, Alexandros Alexakis, and Pablo D. Mininni. Abrupt transition between three-dimensional and two-dimensional quantum turbulence. *Phys. Rev. Lett.*, 124(13):134501, 2020.
- [146] A. Picozzi, J. Garnier, T. Hansson, P. Suret, S. Randoux, G. Millot, and D. N. Christodoulides. Optical wave turbulence: Towards a unified nonequilibrium thermodynamic formulation of statistical nonlinear optics. *Phys. Rep.*, 542(1):1–132, 2014.
- [147] Catherine Sulem and Pierre-Louis Sulem. *The Nonlinear Schrödinger Equation: Self-Focusing and Wave Collapse*, volume 139 of *Applied Mathematical Sciences*. Springer-Verlag, New York, 1999.
- [148] D. G. Levkov, A. G. Panin, and I. I. Tkachev. Gravitational Bose-Einstein condensation in the kinetic regime. *Phys. Rev. Lett.*, 121(15):151301, 2018.
- [149] Colm Connaughton, Sergey Nazarenko, and Alan C. Newell. Dimensional analysis and weak turbulence. *Phys. D*, 184(1-4):86–97, 2003.
- [150] Davide Proment, Miguel Onorato, Pietro Asinari, and Sergey Nazarenko. Warm cascade states in a forced-dissipated Boltzmann gas of hard spheres. *Phys. D*, 241(5):600–615, 2012.
- [151] Colm Connaughton and Rachel McAdams. Mixed flux-equipartition solutions of a diffusion model of nonlinear cascades. *Europhys. Lett. EPL*, 95(2):24005, 2011.

- [152] Colm Connaughton and Sergey Nazarenko. Warm cascades and anomalous scaling in a diffusion model of turbulence. *Phys. Rev. Lett.*, 92(4):044501, 2004.
- [153] V. S. L’vov and S. Nazarenko. Differential model for 2D turbulence. *JETP Lett.*, 83(12):541–545, 2006.
- [154] V. N. Grebenev, S. B. Medvedev, S. V. Nazarenko, and B. V. Semisalov. Steady states in dual-cascade wave turbulence. *J. Phys. A*, 53(36):365701, 2020.
- [155] Uriel Frisch, Susan Kurien, Rahul Pandit, Walter Pauls, Samriddhi Sankar Ray, Achim Wirth, and Jian-Zhou Zhu. Hyperviscosity, Galerkin truncation, and bottlenecks in turbulence. *Phys. Rev. Lett.*, 101(14):144501, 2008.
- [156] Victor S. L’vov, Sergei V. Nazarenko, and Oleksii Rudenko. Bottleneck crossover between classical and quantum superfluid turbulence. *Phys. Rev. B*, 76(2):024520, 2007.
- [157] D. V. Semikoz and I. I. Tkachev. Kinetics of Bose condensation. *Phys. Rev. Lett.*, 74(16):3093–3097, 1995.
- [158] D. V. Semikoz and I. I. Tkachev. Condensation of bosons in the kinetic regime. *Phys. Rev. D*, 55(2):489–502, 1997.
- [159] Sergei V. Nazarenko and Alexander A. Schekochihin. Critical balance in magnetohydrodynamic, rotating and stratified turbulence: towards a universal scaling conjecture. *J. of Fluid Mech.*, 677:134–153, 2011.
- [160] Argelia Bernal and F Siddhartha Guzmán. Scalar field dark matter: Head-on interaction between two structures. *Phys. Rev. D*, 74(10):103002, 2006.
- [161] Bodo Schwabe, Jens C. Niemeyer, and Jan F. Engels. Simulations of solitonic core mergers in ultralight axion dark matter cosmologies. *Phys. Rev. D*, 94(4):043513, 2016.
- [162] Mustafa A. Amin and Philip Mocz. Formation, gravitational clustering, and interactions of nonrelativistic solitons in an expanding universe. *Phys. Rev. D*, 100(6):063507, 2019.
- [163] F. Siddhartha Guzmán and L. Arturo Ureña-López. Evolution of the Schrödinger-Newton system for a self-gravitating scalar field. *Phys. Rev. D*, 69(12):124033, 2004.
- [164] F. Siddhartha Guzmán and L. Arturo Ureña-López. Gravitational cooling of self-gravitating Bose condensates. *Astrophys. J.*, 645(2):814–819, 2006.

- [165] Tiago D. Ferreira, Nuno A. Silva, and A. Guerreiro. Superfluidity of light in nematic liquid crystals. *Phys. Rev. A*, 98(2):023825, 2018.
- [166] I. E. Alber. The effects of randomness on the stability of two-dimensional surface wavetrains. *Proc. R. Soc. London, Ser. A*, 363(1715):525–546, 1978.
- [167] V. E. Zakharov, S. L. Musher, and A. M. Rubenchik. Hamiltonian approach to the description of non-linear plasma phenomena. *Phys. Rep.*, 129(5):285–366, 1985.
- [168] V. S. Lvov and A. M. Rubenchik. Spatially non-uniform singular weak turbulence spectra. *Soviet Physics-JETP*, 45(1):67–74, 1977.
- [169] B. Hall, M. Lisak, D. Anderson, R. Fedele, and V. E. Semenov. Statistical theory for incoherent light propagation in nonlinear media. *Phys. Rev. E*, 65(3):035602, 2002.
- [170] Miguel Onorato, Alfred Osborne, Renato Fedele, and Marina Serio. Landau damping and coherent structures in narrow-banded 1 + 1 deep water gravity waves. *Phys. Rev. E*, 67(4):046305, 2003.
- [171] Antonio Picozzi. Towards a nonequilibrium thermodynamic description of incoherent nonlinear optics. *Opt. Express*, 15(14):9063–9083, 2007.
- [172] A. Picozzi and J. Garnier. Incoherent soliton turbulence in nonlocal nonlinear media. *Phys. Rev. Lett.*, 107(23):233901, 2011.
- [173] M. Onorato, S. Residori, U. Bortolozzo, A. Montina, and F. T. Arecchi. Rogue waves and their generating mechanisms in different physical contexts. *Phys. Rep.*, 528(2):47–89, 2013.
- [174] P. A. E. M. Janssen. Nonlinear four-wave interactions and freak waves. *J. Phys. Oceanogr.*, 33(4):863–884, 2003.
- [175] Steven A Orszag. Numerical methods for the simulation of turbulence. *The Physics of Fluids*, 12(12):II–250, 1969.
- [176] D. Gottlieb and S. A. Orszag. *Numerical analysis of spectral methods: theory and applications*. SIAM, 1977.
- [177] Matteo Frigo and Steven G Johnson. The design and implementation of FFTW3. *Proceedings of the IEEE*, 93(2):216–231, 2005.
- [178] J. W. Cooley and J. W. Tukey. An algorithm for the machine calculation of complex Fourier series. *Mathematics of computation*, 19(90):297–301, 1965.

- [179] G. Krstulovic and M. Brachet. Energy cascade with small-scale thermalization, counterflow metastability, and anomalous velocity of vortex rings in Fourier-truncated Gross-Pitaevskii equation. *Physical Review E*, 83(6):066311, 2011.
- [180] Steven M Cox and Paul C Matthews. Exponential time differencing for stiff systems. *Journal of Computational Physics*, 176(2):430–455, 2002.
- [181] P. C. di Leoni, P. J. Cobelli, and P. D. Mininni. The spatio-temporal spectrum of turbulent flows. *The European Physical Journal E*, 38(12):1–10, 2015.
- [182] J. M. Skipp. Simulations of the 2D Schrödinger-Helmholtz equation, 2021. URL https://warwick.ac.uk/fac/cross_fac/complexity/people/students/dtc/students2012/skipp/she_simulations/.